CONTROL SYSTEM DESIGN FOR HIGH PERFORMANCE SCANNING TUNNELING MICROSCOPY

by

Farid Tajaddodianfar

APPROVED BY SUPERVISORY COMMITTEE:

S.O. Reza Moheimani, Chair

John N. Randall

Robert D. Gregg IV

Tyler Summers

This dissertation

is dedicated to my wife, Mahsa, for all her support

CONTROL SYSTEM DESIGN FOR HIGH PERFORMANCE SCANNING TUNNELING MICROSCOPY

by

FARID TAJADDODIANFAR, BS, MS, PhD

DISSERTATION

Presented to the Faculty of

The University of Texas at Dallas

in Partial Fulfillment

of the Requirements

for the Degree of

DOCTOR OF PHILOSOPHY IN

MECHANICAL ENGINEERING

THE UNIVERSITY OF TEXAS AT DALLAS

May 2018

ACKNOWLEDGMENTS

I would like to gratefully thank Dr. Reza Moheimani for all his advice and support. Completion of this work couldn't be possible without the help of our Zyvex Labs fellows. I appreciate John N. Randall, James Owen, Ehud Fuchs and Joshua Ballard of Zyvex Labs for all of their fruitful discussions and for their scientific comments. I gratefully thank Dr. Tyler Summers and Dr. Robert Gregg for reviewing this dissertation and providing valuable comments. Also, I thank Zyvex Labs technicians, Robin Santini and Cyndi Delgado, for their help to keep the STM operational.

March 2018

CONTROL SYSTEM DESIGN FOR HIGH PERFORMANCE

SCANNING TUNNELING MICROSCOPY

Farid Tajaddodianfar, PhD
The University of Texas at Dallas, 2018

Supervising Professor: S.O. Reza Moheimani, Chair

Scanning Tunneling Microscope (STM) is scientific instrument that is used to generate atomic-resolution images from material surface. Since its invention in early 1980s, STM has played a crucial role in advancements and many breakthroughs in nanotechnology. The early works on STM concentrated on imaging. However, soon it was realized that the STM tip could be used as an effective tool for patterning the surface with a resolution down to a single atom through lithography. This capability of STM has turned it to an important instrument in atomically-precise manufacturing. Tip-sample crash is a prevalent failure in STM which severely limits its performance. Adverse effects of such failure are even worse in lithography applications which need preserved non-changing tip shape.

In this research, we focus on the STM control system to address the tip-sample crash problem. Based on frequency-domain closed-loop system identification tests, we show that the DC gain of the open-loop plant depends on the Local Barrier Height (LBH) which is a quantum mechanical property of the tip and sample. Since LBH is highly variable due to local changes in surface and tip properties, the control loop gain is subject to large changes. Such variations adversely affect the closed-loop stability and increase the chance of tip-sample crash if the controller gains are kept fixed.

We propose a method for estimating LBH on-the-fly and use that estimation to adaptively tune the gains of a proportional-integral (PI) controller. Results of the proposed LBH measurement method are not dependent on the feedback parameters, despite a method prevalently used in STM research. We report experimental results confirming variability of LBH, enhanced closed-loop stability in the presence of the tuning method, and extended tip life-cycle. Furthermore, we study the effect of proposed control method on the STM performance in Hydrogen Depassivation Lithography (HDL), and show that it results in more stable current and improves the STM performance. Moreover, we investigate the HDL procedure and suggest effective ways for conducting the HDL from a control system perspective to minimize damages to the tip during lithography.

TABLE OF CONTENTS

LIST OF FIGURES

LIST OF TABLES

CHAPTER 1

INTRODUCTION

1.1 Overview

Invention of Scanning Tunneling Microscope (STM) in the early 1980s put the idea of Scanning Probe Microscopy (SPM) into the practice and brought the Nobel prize in physics to its inventors (Binnig and Rohrer, 2000). Over the past three decades, the STM has found a myriad of applications in numerous fields leading to ground-breaking observations, e.g. see (Wolkow, 1992; Zhang et al., 2009; Hansma V.B. Elings, O. Marti, C.E. Bracker, 1988; Loth et al., 2010). The early work on STM concentrated on imaging. However, soon it was realized that the STM tip could be used as an effective tool for patterning the surface with a resolution down to a single atom (Lyding et al., 1994). In the nano-lithography applications, the tunneling current triggers a chemical reaction at a specific location on the sample surface to selectively deposit a single atom. This underlying concept behind atomically-precise manufacturing, is an active research topic in nanotechnology (Ballard et al., 2013; Fuechsle et al., 2012; Weber et al., 2012; Lee et al., 2014).

Performance of the STM control system has a major effect on the quality of acquired images. Few attempts have been made to improve the STM control system. In Chapter 2 we review the research background focusing on the STM control system and discuss the state of the art in this field. In practice, poor control performance causes unsafe decrease in the tip-sample separation and consequently increases the risk of tip-sample crash. Such a crash is a failure that results in irreversible damage to both tip and sample and adds to the operation costs. Tip-sample crash problem can be more challenging in the nano-lithography applications where STM operates at higher current, higher bias voltage and potentially smaller tip-sample separation. Additionally, in the nano-lithography applications it is crucially important that the STM tip preserves its geometry during the process, otherwise the idea of atomically-precise manufacturing will be challenged due to the tip shape changes (Ballard et al., 2013). Unsafe tip-sample proximity due to the poor performance of the STM control system can be a reason for the tip changes. Our research is directed toward the design and implementation of an ultra-high-precision control system which avoids tip-sample crash and enables the STM to be effectively used for imaging and atomically-precise manufacturing.

In this chapter, we review the principals of STM operation and briefly discuss the theory of the tunneling current. We also discuss a number of various STM scanners. Since this research is performed on the Zyvex labs' STMs, we mainly focus on their STM scanners. Also we briefly review the current control system of the existing STMs. Later in this chapter, we briefly review the applications of STM.

1.2 Working Principle

Basic concept of the SPM is to move an extremely sharp probing tip at a nano-meter distance over a sample to collect surface topography information via a physical phenomenon that takes place between the tip and sample. In STM, this phenomenon is a quantum mechanical effect known as the tunneling current which refers to an electrical current established due to the tunneling of electrons through the space between a conducting tip and sample while their relative distance is below one nanometer and a bias DC voltage is applied to them. This current is modeled as an exponential function of the tip-sample separation. Obtaining an atomic-resolution surface image requires rastering of the STM tip over the sample. While scanning, atomic-scale surface features cause a change in the tip-sample separation and consequently in the tunneling current. A control system measures this current and adjusts the vertical tip position to compensate for the current variations and keep the current constant. Thus, the tip vertical motion relative to the sample is proportional to the height of the atomic-scale surface features, and the controller command maps a topography of the surface. Figure 1.1 displays a schematic of the STM operation in the constant current mode.

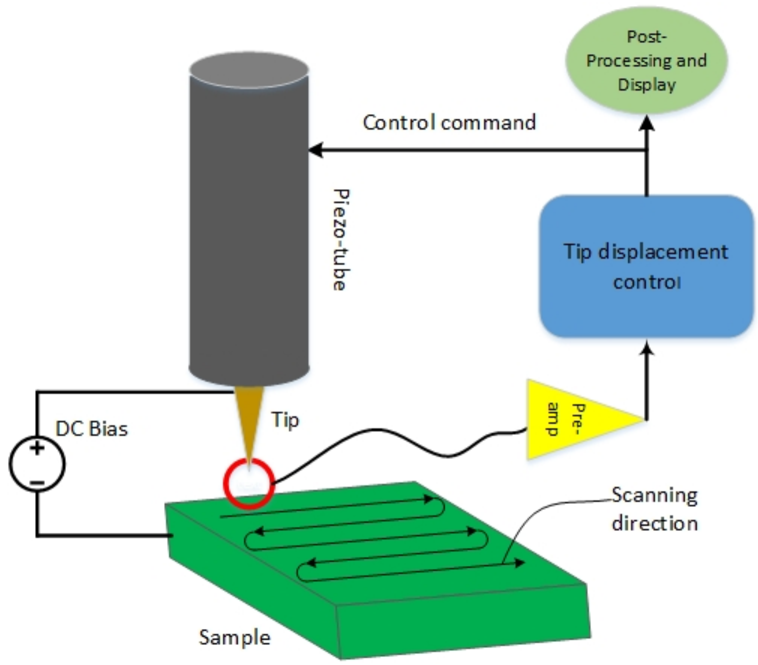

Figure 1.1. Schematic of STM operating in constant current mode

1.3 Tunneling current

Quantum mechanical calculations suggest that the electrical current which tunnels through the vacuum between tip and sample is proportional to the applied bias voltage and is an exponential function of the tip-sample separation (Binnig and Rohrer, 2000; Garcia et al., 1983). A simplified tunneling current model is then obtained as (Lang, 1988):

$$i = \sigma V_b e^{-1.025\sqrt{\varphi}\delta} \tag{1.1}$$

where V_b is the bias voltage between tip and sample, σ is a parameter depending on the material and geometry of the tip and sample, and δ (in $\mathring{A}$) is the energy barrier thickness which is approximately the geometrical tip-sample separation (Lang, 1988). φ (in eV) is called "Work function" or "Barrier Height" which by definition is the minimum energy required to remove an electron from a solid. In quantum physics, the energy of electron in vacuum is higher than its energy in solid and this difference, i.e. the Work Function, acts as a barrier preventing electrons from leaving the solid. So the terms Work Function and Barrier Height are close in meaning (Voigtlander, 2015; Binnig and Rohrer, 2000). A pre-amplifier of gain R is used to convert sub-nano-ampere range tunneling current i given by (1.1) to a measurable voltage, the natural logarithm of which is then taken with the aim of linearizing the model. This gives:

$$\ln(Ri) = \ln(R\sigma V_b) - 1.025\sqrt{\varphi}\delta \tag{1.2}$$

which indicates that for constant σ and V_b the logarithm of tunneling current is proportional to the tip-sample separation. This linear relationship between $\ln i$ and δ is crucial to the operation of STM which ultimately maps a surface topography correlated to δ by keeping the current constant using a linear feedback. Additionally, equation (1.2) suggests that, for constant σ and V_b, the logarithmic derivative of current with respect to the tip-sample separation provides a measure of the barrier height (Binnig et al., 1984; Lang, 1988; Kuk, 1990):

$$\varphi = 0.952\left(\frac{d}{d\delta}\ln Ri\right)^2 \tag{1.3}$$

In the early STM works, in order to measure φ using equation (1.3), the tip-sample separation δ is modulated by a known frequency Ω. Then, the derivative required in equation (1.3) is obtained by tracking the Ω component of the logarithm of tunneling current using a Lock-in Amplifier (LIA) (Binnig et al., 1984; Wiesendanger et al., 1987). Later in section 4.2 we will propose another method for measuring φ. It has been understood in the STM community that the barrier height depends on the physical properties of the tip apex as well as those of the sample surface atoms into which the current tunnels (Lang, 1988). This means that barrier height is a local effect and is subject to change based on variations in the instantaneous and spatial physical properties of the tip and sample. Based on this understanding, parameter φ obtained by the described method can be used to produce another image while scanning a surface. This is referred to as the Local Barrier Height (LBH) image, and is the basis for Scanning Tunneling Spectroscopy (STS) which provides additional information about the physical and chemical surface characteristics (Wiesendanger et al., 1987; Maeda et al., 2004; Binnig and Rohrer, 2000; Jia et al., 1998).

Experimental investigations have also shown that, for the range of tip-sample separation δ at which the STM usually operates, φ representing the LBH is nearly independent of δ (Binnig et al., 1984; Lang, 1988; Maeda et al., 2004). This experimental observation assures that the linearization provided by equation (1.2) remains effective for normal operating ranges of STM. Thus, it is possible to utilize a linear feedback control system to keep the current constant by changing tip-sample distance. In section 3.4 we discuss the operation of this closed-loop control system and investigate the effect of LBH on the stability and performance of the STM control system.

The rule of thumb calculation of current shows that a variation of 0.1nm in tip-sample separation results in a difference in the tunneling current by nearly an order of magnitude(Voigtlander, 2015). This means that if the tip approaches the sample only by $1\mathring{A}$ then the current would change near 10 times. This sensitivity in the tip-sample distance is the reason for the extremely high vertical resolution of the STM which can reach the picometer regime. Atoms on the tip which protrude only 2.5 (∼one atomic distance) less toward the sample carry only a factor of 150 less current. This means that the majority of the tunneling current is carried by the "last atom", which also explains the very high (ultimately atomic) lateral resolution of the STM(Voigtlander, 2015).

1.4 STM Scanners

1.4.1 Tube Scanners

Tube Piezo elements are prevalently being used in scanning probe microscopy applications, due to their compact design and high resonance frequencies as well as capability of providing motion in three orthogonal directions. Tube scanners are made of a radially poled piezoceramic tube covered by metallic electrodes both inside and outside. The outer electrode is divided into four quadrants. If a voltage is applied to the all outer electrodes and the inner electrode, an axial motion will be observed due to the transverse piezo effect. If two opposite outer electrodes are actuated with opposite voltages, a bending motion will result.

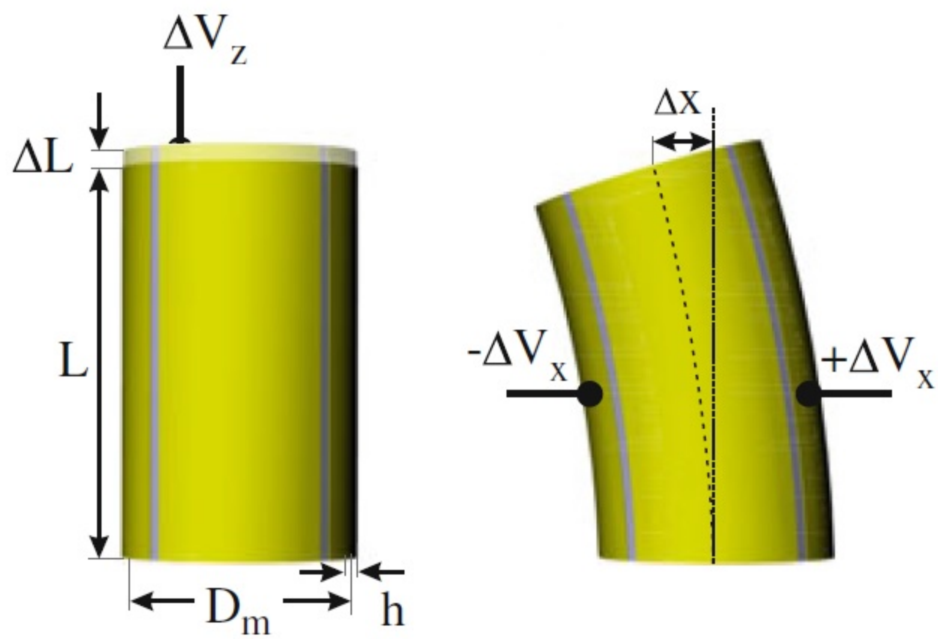

Figure 1.2. Tube Piezo actuator; left) axial motion, right) bending motion (Voigtlander, 2015)

As shown in Figure 1.2, bending of the tube in any direction produces a slight motion in axial direction, as well. In most works, this cross-coupling is negligible in most cases. However, for compensation of such undesired motion and increasing the accuracy, the outer

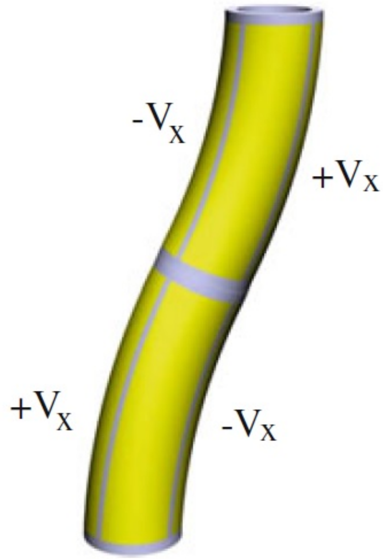

Figure 1.3. Tube piezo actuator with eight outer sections to avoid coupling between in-plane and axial motions (Voigtlander, 2015)

electrode is divided into eight sections instead of four; then, for providing an in-plane motion the upper and lower sections of the tube are bent in opposite directions (Figure 1.3).

Despite their effectiveness in providing high-resolution motion, piezo-electric actuators suffer from various nonlinear phenomena, including hysteresis and creep, which makes their modeling and control issues challenging. Thus, a large body of work has been devoted in the past years to cope with their problems. Also, the tube scanners are mainly used for fine positioning and rastering in STM. They need to be accompanied by another actuator which supports the coarse positioning purposes. In STM, the coarse positioning is required to bring the tip from far away from the sample to a distance as close as 1nm to the sample, to get the tunneling current established (or equivalently to engage the tip and sample). Then, fine positioning with a piezo-tube is required for scanning and current control.

1.4.2 Lyding Scanner

In the earliest STM designs, Binnig and Rohrer placed their STM tip on the edge of a piezo-tube to be fine positioned (Binnig and Rohrer, 2000). In another design which appeared a few years later, (Lyding et al., 1988) proposed their STM scanner. The Lyding scanner is made of two concentric piezo-tube actuators. The STM tip is mounted in the center of the inner tube, and the STM sample is mounted on the outer tube. The outer tube produces coarse positioning of the tip relative to the sample by moving the sample toward tip by stick-slip mechanism. The inner tube, then, is used for fine positioning of the tip and rastering. One of the Zyvex Labs STMs benefits from the Lyding scanner which is shown in Figure 1.4. Later in this report we will present our experimental results obtained using the Lyding scanner.

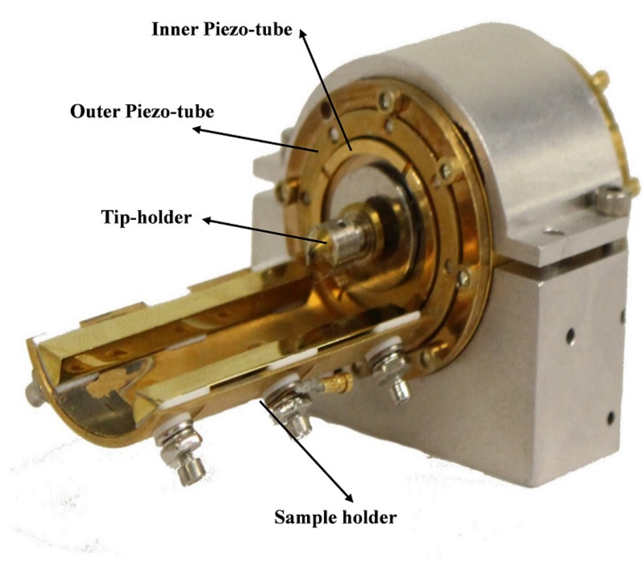

Figure 1.4. The Lyding scanner used in Zyvex Labs' STM

1.4.3 Zyvex Pyadkin Scanner

Zyvex lab's benefits from an innovative scanner in one of their STMs. The scanner is a patented innovation of the Zyvex Labs, shown in Figure 1.5. This serial-kinematic scanner has three linear shear-stack piezoelectric actuators, one each for the X, Y, and Z axes where the X and Y axes are the scan axes. The Z axis actuator sits on the X axis actuator and both Z and X axes actuators sit on the Y actuator. All three actuators combine fine motion (deflection of piezo stacks) and coarse motion via slip-stick with ruby spheres in etched silicon groves providing a linear motion. The scanner is set up with the Z Axis in the horizontal plane. It is very compact, stiff, and the lowest resonant frequency is impressively high near 8 kHz. Further discussion about the dynamics of the scanner is given in section 3.2.1.

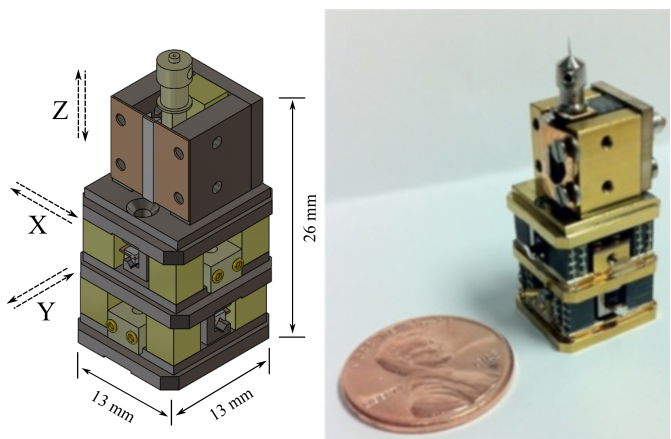

Figure 1.5. The Pyadkin piezo-stack scanner

1.4.4 Omicron Scanner

Scienta-Omicron produces a commercial SPM platform (Figure 1.6) which can be used for STM and AFM applications. This scanner is used in Zyvex Labs' ultra-high-vacuum (UHV) chambers and is equipped with pA resolution current amplifier for STM imaging and lithography. Coarse positioning in Z,Y and Z directions are provided by a stick-slip mechanism and covers a range of 10mm at each direction with steps as small as 40 nm. Fine positioning is provided by piezo-tube scanner and covers a $12\mu m \times 12\mu m \times 1.5\mu m$ range with a resolution in Z direction better than 0.01 nm. The current pre-amplifier covers a range of 1 pA-330 nA with different bandwidth at various ranges. A built-in eddy current vibration isolation system provide the required isolation from the ambient vibrations and this design does not need an additional stage for vibration isolation. In the next chapters, we present our test results on this scanner.

Figure 1.6. Scienta Omicron's variable temperature SPM setup for UHV STM applications (ScientaOmicron, ScientaOmicron)

1.5 Experimental STM setup

Zyvex lab's STM operates in Ultra-High Vacuum (UHV) with a pressure as low as $10^{-11} Torr$. Typical samples are made of Hydrogen passivated silicon. The STM is customized for Hydrogen Depassivation Lithography (HDL), a promising method for atomically precise manufacturing. For details about Zyvex lab's approach to STM-HDL see (Ballard et al., 2013). In this approach, the STM tip is used both for generating atomic-resolution images and for creating lithography patterns on the surface. Throughout this paper we focus on the STM operation in imaging mode.

Zyvex labs' STM benefits from a 20-bit Digital Signal Processor (DSP) running at 50 kHz sampling frequency which is used for all data acquisition and control purposes, and commercially is known as Zyvector^{TM}. A customized software named ScanZ provides the user with an interface for operating the STM both in imaging and in lithography modes. ScanZ is also equipped with image post-processing tools as well as functions for driving the scanner in coarse motion and getting the STM tip and sample engaged. A Femto DLPCA-200 current-to-voltage pre-amplifier is used to detect the tunneling current in Pyadkin and Lyding scanners, and is a main element of the control system discussed next. For frequency-domain measurements reported in this dissertation, we use an ONOSOKKI CF-9400 FFT Analyzer. Also for online time-domain measurements and analysis we use a dSpace Microlab Box.

1.6 Z-axis control system architecture

The effective instantaneous tip-sample gap, δ, can be calculated as:

$$\delta = d_{hm} - d_0 - h - d_{tp} \tag{1.4}$$

where d_{hm} represents the tip-sample separation when the tip is at its home position after the tip-sample engagement, d_0 stands for changes in the tip-sample gap while scanning due to sample distortion or drift, h is the surface features' height and represents the actual surface topography, and d_{tp} is the tip displacement due to the control command. Figure 1.7a displays a block diagram of the closed-loop current control system of the STM.

The effective tip-sample gap δ is converted to a current i through the tunneling current physics. The pre-amplifier, represented by a gain R, detects this sub-nano-ampere range current and converts it to a measurable voltage V_i which is then sampled by an A/D converter. Natural logarithm of the measured signal is first taken, then it is compared to the logarithm of the amplified setpoint current $\ln(Ri_d)$ to determine the error signal based on which a controller $K(s)$ calculates the appropriate command to set the error signal back to zero. The control command passes through the D/A converter and the High-Voltage-Amplifier $G_h(s)$, moves the piezo-actuator $G_p(s)$ and modifies δ to keep the current constant. While scanning, the surface topography appears as an unknown disturbance h in the tip-sample gap and results ina change in the tunneling current. The current control system adjusts the vertical position of the tip to keep the current constant during scanning. Thus, the control command maps the surface topography. Misalignment of the sample or drift generates another disturbance d_0 while noise n is mainly generated with the current measurement. The STM open-loop model in z-direction is shown by $G(s)$ in Figure 1.7a which represents all the dynamics from control command to $logi$ signal. The model $G(s)$ is required for model-based analysis and control design. In the next section we present our approach for identification of $G(s)$.

Assuming a model given by equation (1.1) for the tunneling current and taking its logarithm stated in equation (1.2), the closed-loop control block diagram is simplified as shown in Figure 1.7b. Thus, the local barrier height φ appears as a loop gain in the control system, while the bias voltage V_b and the pre-amplifier gain R appear as a static input to the system given the fact that V_b and R are kept constant during STM imaging. In the rest of this report we use the simplified block diagram shown in Figure 1.7b for our discussions.

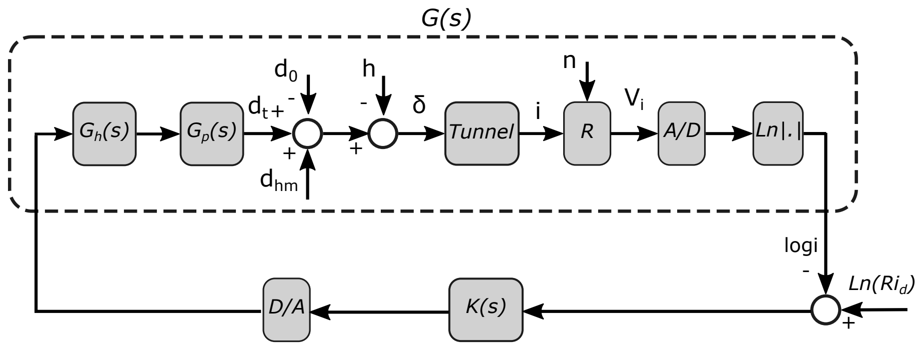

(a)

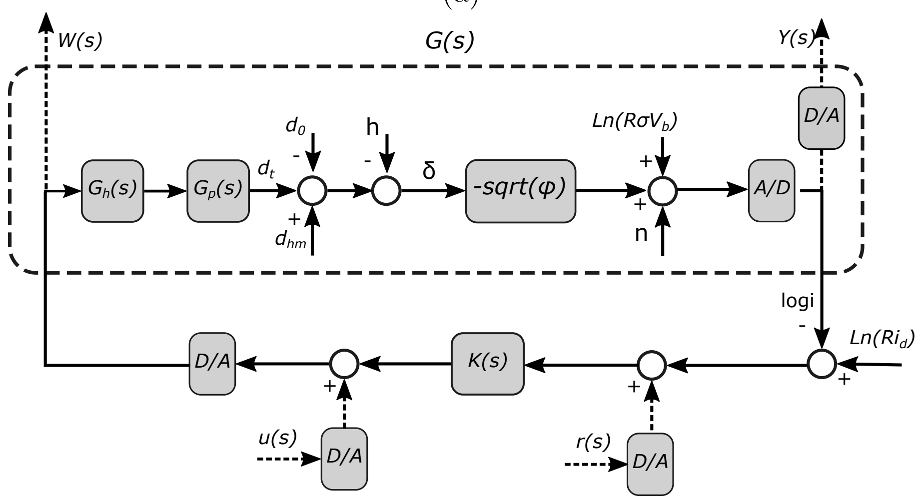

(b)

Figure 1.7. a) Block diagram of the STM Z-axis control system, b) control block diagram with simplified tunneling current model. Exogenous inputs and outputs for identification purposes are shown in dashed arrows.

1.7 STM applications

Over the past three decades, the STM has found a myriad of applications in numerous fields leading to ground-breaking observations, e.g. see (Wolkow, 1992; Zhang et al., 2009; Hansma

V.B. Elings, O. Marti, C.E. Bracker, 1988; Loth et al., 2010). In this section we briefly review the possible applications of STM.

1.7.1 Imaging

The STM was first invented with the aim of acquiring atomic-resolution images from the surface of conductive material. Early developments of STM showed that three different types of STM images are available, as discussed below.

Topography images

The main idea of STM operation described in section 1.2 results in an image which shows the physical Z-axis displacement of the tip while it moves over the sample and this is mainly due to the roughness of the surface. This image is called topography image and presents the height of atomic features. Furthermore, a change in current during a scan can occur not only due to the height of the atomic surface features, but also due to a possible change in the electronic properties of the surface atoms. Since such a change in the electronic properties results in a change in current, the controller moves the tip to compensate for current changes. This means that any variation in the electronic properties appear as an artifact in the topography image.

Figure 1.8 displays an STM topography images of a hydrogen passivated silicon surface. The surface of this sample is covered with hydrogen atoms. Bright spots are missing hydrogen atoms which appear to be higher than others atoms despite the fact that they are actually lower than the surrounding because of a missing hydrogen. This is because the current can easily tunnel to silicon rather than hydrogen. At an spot with missing hydrogen, the tunneling current increases due to a change in the electronic properties of atoms and the controller moves the tip away to keep the current constant. Thus the missing hydrogen area appear to be higher than the surrounding.

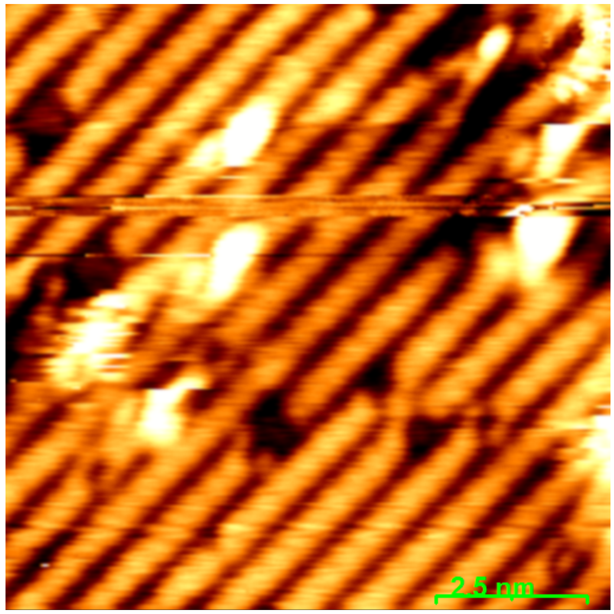

Figure 1.8. STM topography image of a hydrogen passivated silicon sample. Image obtained by Zyvex Labs STM.

Local Barrier Height images

As described in section 1.3, a modulation method can be used to determine the Local Barrier Height (LBH) while scanning the sample. The LBH image provides additional information about the electronic and quantum mechanical properties of the sample. Our research has revealed that the LBH is of great importance from a feedback control point of view, and this will be discussed in detail in Chapter 4. Figure 1.9 displays an LBH image of hydrogen passivated silicon sample obtained by our method described in Chapter 4.

Scanning Tunneling Spectroscopy

A third possible way to obtain an STM image is called scanning tunneling spectroscopy (STS) (Binnig and Rohrer, 2000). In this method the bias voltage applied to the tip and sample is modulated by known frequency and the corresponding frequency component in the tunneling current is being tracked by a lock-in amplifier. Referring to simplified current model given by equation 1.1, this modulation method effectively gives the differential

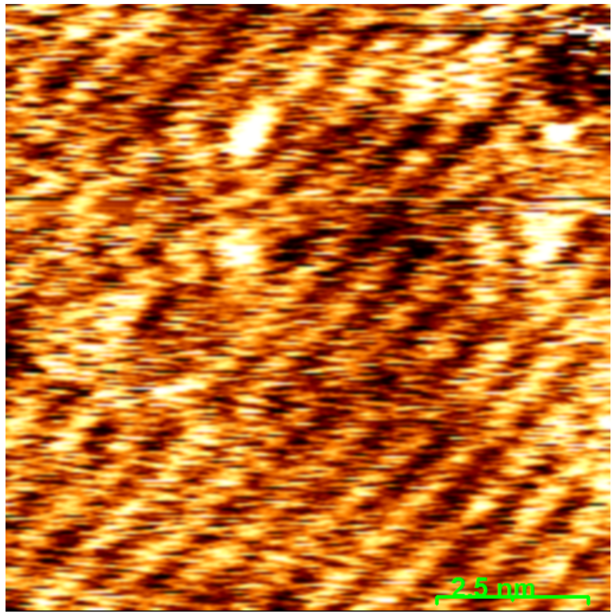

Figure 1.9. LBH image of a hydrogen passivated silicon sample, obtained simultaneously by the topography image of Figure 1.8 using a modulation method described in section 4.2

resistance di/dV (Voigtlander, 2015). However, since the work function φ is also a function of the bias voltage, di/dV is also dependent on V and tip-sample separation. It has been shown that the normalized differential resistance provides a better measurement and is less dependent on the tip-sample separation:

$$\frac{\frac{di}{dV}}{\frac{i}{V}} = \frac{d \ln i}{d \ln V} \tag{1.5}$$

The STS image provides additional useful information about the electronic and quantum mechanical properties of the sample surface.

1.7.2 Nano-lithography

The early work on STM concentrated on imaging. However, soon it was realized that the STM tip could be used as an effective tool for patterning the surface with a resolution down to a single atom (Lyding et al., 1994; Hla and Rieder, 2002). In the nano-lithography applications, the tunneling current triggers a chemical reaction at a specific location on the sample surface to selectively deposit a single atom.

STM-based nano-lithography is mainly accomplished through a process called Hydrogen Depassivation Lithography (HDL). In this method, a silicon sample with surface passivated by hydrogen is patterned by STM tip. To do this, the STM tip is used to tunnel a large current to hydrogen atoms and this provides enough energy to break the bond between hydrogen and silicon and depassivate the hydrogen atom. Depassivated region present higher reactivity than the background and these regions are used to selectively deposit silicon or other atoms. This underlying concept behind atomically-precise manufacturing, is an active research topic in nanotechnology (Ballard et al., 2013; Fuechsle et al., 2012; Weber et al., 2012; Lee et al., 2014; Loth et al., 2010; Zhang et al., 2009)

1.8 Tip change challenge in STM

Successful operation of STM depends on many factors. Among these factors, the STM tip plays a crucial role. The resolution of the STM image depends on the sharpness of the tip. The more atomically-sharp the tip, the better image resolution. However, it is usually observed that the STM tip is subject to change. The tip change can originate from a range of reasons: from adsorption of contaminating atoms on the tip apex to temperature change or even tip-sample contact. Among these reasons, the tip-sample contact can be originated from poor control system performance. In practice, tip-sample mechanical contact can easily happen due to instabilities or resonances of the actuator, noting that the tip-sample separation in imaging mode is near a few angstroms. A contact between tip and sample may result in lose of imaging capability and irreversible damage to the tip and sample.

In nano-lithography mode the tip-change problem is even more sever. In litho mode, the tip-sample separation can potentially be smaller compared to that in imaging mode, and this magnifies the importance of high-precision and high-performance control of the tip. Furthermore, if tip changes while patterning the sample in the lithography mode, the obtained pattern might be different from the desired pattern, and this severely undermines the atomically-precise manufacturing goal.

Our research is directed toward design and implementation of a high-performance control system which can avoid possible tip-sample contact that results from poor performance of the control system. Our ultimate goal is to design a control system that protects the STM tip and facilitates the atomically-precise manufacturing process. Toward this goal, we start our research by reviewing the state of the art in STM control, identification of the STM control system and designing appropriate control methods, accordingly. We report our progress in the next chapters.

CHAPTER 2

RESEARCH BACKGROUND

2.1 Overview

In this chapter, we review the background of research conducted on the STM instrumentation and control. By reviewing the previous works in this field, we draw the state of the art and define our research objective in this field.

2.2 STM Control Research

2.2.1 Current control

The early STMs used proportional-integral (PI) control for tip-sample distance control with the aim of maintaining the tunneling current in a desired fixed level. In the early works, stability of the tunneling loop was the main interest. (Oliva et al., 1995) approximated the components of tunneling feedback loop by simple transfer functions based on specific parameters, and proposed analytical solutions for working regimes with guaranteed stability. They showed that resonance-induced instability in the feedback loop can cause severe misinterpretations of the obtained image. For example, they showed that an unstable STM can produce images which are far away from the real surface topography. They suggested STM users to calculate stable working regimes prior to imaging (Oliva et al., 1995). Later, (Oliva et al., 1997) presented an experimental approach for identification of the parameters they have already used for determination of stability regions. Their theory suggests that these parameters are given in the following form:

$$G_0 \left[\frac{k_i \tau + (k_i/\omega_c)\xi^2}{k_i + (1+\xi^2)\omega_0^2 \tau^2} \right] < 1 \qquad (2.1)$$

where G_0 is the overall closed-loop gain, k_i is the integral controller gain and ω_c is the PI controller corner frequency. Unknown parameters which should be determined by experiment are ξ, ω_0 and τ as the damping factor, resonance frequency and time constant related to damping, respectively (Oliva et al., 1997). They proposed a two-step procedure for their experiment using a tripod Piezo-electric actuator (PEA). In the first step, as shown in Figure 2.1a, the tip is far from the sample and the tunneling current is zero. A harmonic excitation is applied to one piezo and the response induced in the other is recorded. Using a lock-in amplifier, the frequency response of coupling between X,Y,Z axes are obtained. In the second step, as shown in Figure 2.1b, the tip is engaged and the feedback loop is closed with the established tunneling current. Here, a harmonic voltage is injected in the input of one piezo and the voltages induced in the others are recorded and analyzed by a lock-in amplifier. Comparing the obtained natural frequencies in open- and closed-loop revealed that the natural frequencies shift in closed-loop. This is attributed to the effect of tunneling current and system identification in closed-loop is encouraged (Oliva et al., 1997).

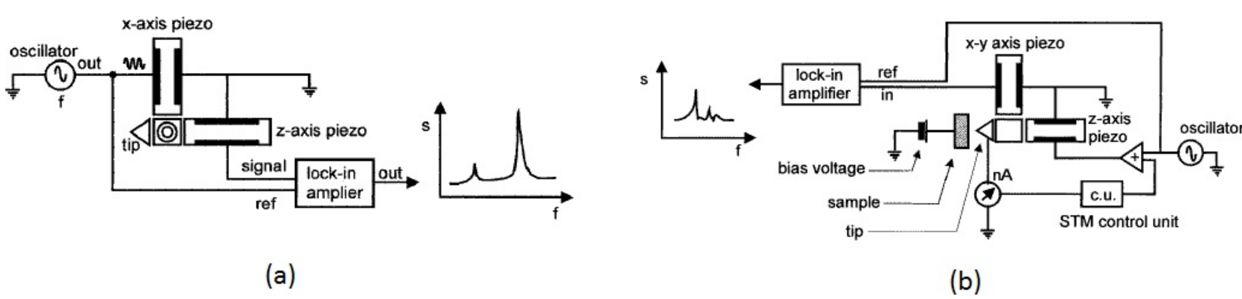

Figure 2.1. The experimental setup implemented by (Oliva et al., 1997) for determination of open-loop (a), and closed-loop (b) frequency responses. Schematics are from (Oliva et al., 1997).

In another work, (Anguiano et al., 1998) extended their analytical study of simplified STM feedback loop to the case of optimal imaging. They argued that for having high quality and reliable images, not only the feedback loop should be stable, but also certain amplitude and phase shift requirements should be satisfied. Figure 2.2 depicts a summary of their stability, amplitude and phase criteria for reliable STM imaging.

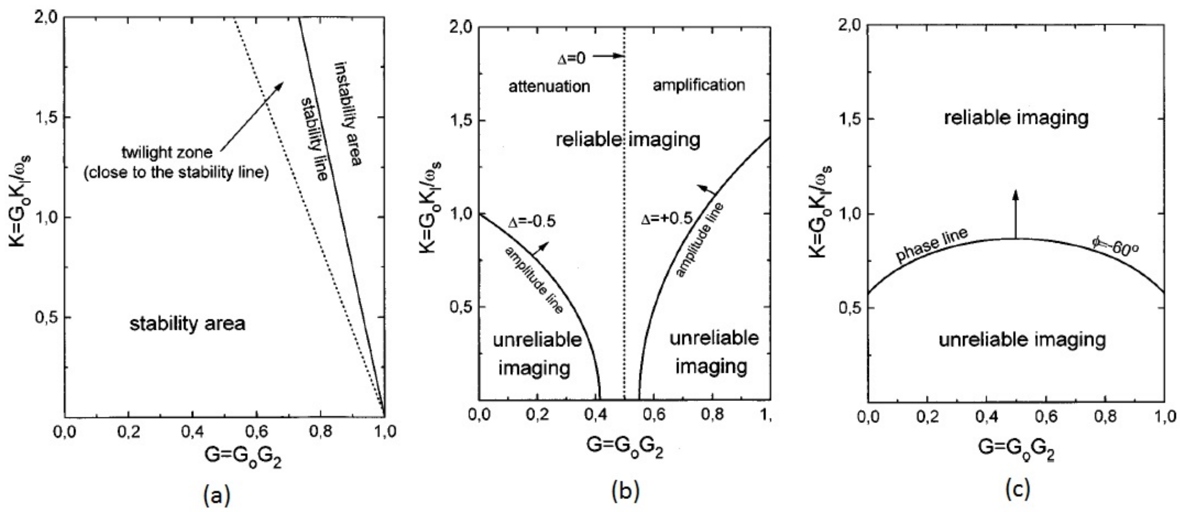

Figure 2.2. a) stability, b) amplitude and c) phase criteria for reliable imaging shown in the parameter space of the STM proposed by (Anguiano et al., 1998). Intersection of the three areas give the reliable imaging regime. Figures are from (Anguiano et al., 1998).

(Boudreau et al., 2002) proposed their work with the intention of building low-price high-precision digital control system for STM using fixed-point Digital Signal Processing (DSP). They described their procedure for designing the appropriate software and cited several important points in their design process. In their attempt for controller design, they first run a closed-loop identification of STM's dynamic behavior. To this aim, they added a step signal to move the tip away from the sample, while it was engaged, and watched for the variation in tunneling current. They identified the closed-loop dynamics by that measurement and obtained the corresponding open-loop dynamics by subtracting the controller which was already known. Based on the obtained open-loop model, appropriate controller was designed via simulations. They also argued that the capacitive coupling between current detector and X-, Y- and Z-axes electrodes is responsible for large noise component in the tunneling current. To cope with this measurement noise, they identified the transfer function between scan-tube signals and the parasite current; then, they subtracted the output components of this transfer function from the real-time measurements (Boudreau et al., 2002).

A sliding mode approach for control of STM was proposed by (Bonnail et al., 2004). They modeled the STM scanner as a linear state-space system using a 3rd order Mason electromechanical representation. They also modeled the tunneling current by a 2nd order Mason model assuming its nonlinear nature to be added as perturbations. They also argued that measuring tunneling current as the only output is not sufficient for preserving observability of the system; thus they measured the current passed through the PEA as the second output. Their control strategy consists of two levels. The first level is a regulatory problem which is solved by a PI controller. At the second level, based on their tunneling current and PEA currents measurement, they evaluated a control law based on the sign of which the control command of first-level PI control was switched. This is mostly similar to the sliding mode control, and is referred to as Variable Structure Control (VSC) approach (Bonnail et al., 2004)(Figure 2.3).

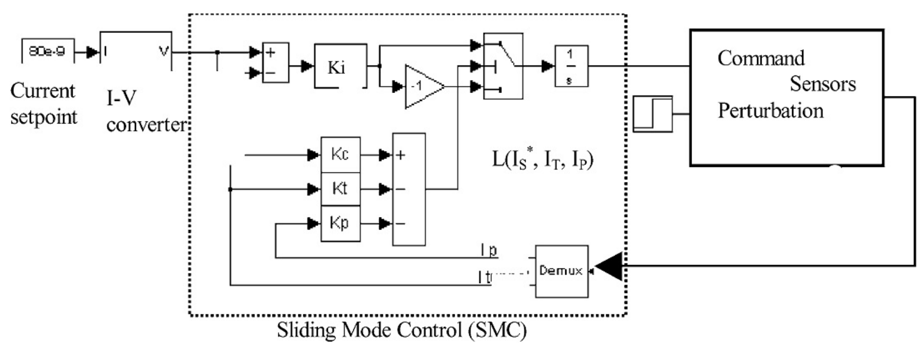

Figure 2.3. Variable Structure Control (VSC) implemented in (Bonnail et al., 2004) for STM control.

In an attempt to improve performance of the STM, (Ahmad et al., 2008) proposed their design procedure for a more advanced controller instead of conventional PI controller. Their method was a loop-shaping technique which aimed to shape the sensitivity function of the

STM control system using a second order notch filter; this was mixed by a pole placement method to ensure both stability and satisfying performance of the system. They took into account the dynamics of the main elements in the STM feedback loop including pre-amplifier, logarithmic amplifier and lowpass filters. They used a linear second-order transfer function for piezo-tube and neglected nonlinear effects of hysteresis and creep. For controller synthesis they also linearized the nonlinear tunneling current model as well as the logarithmic amplifier (Ahmad et al., 2008). For experimental verification of their proposed method, they later reported an experimental setup for measuring and control the tunneling current (Ahmad et al., 2012). Their setup was working in ambient air pressure and was not necessarily useful for surface topography imaging as in STM. This team, in a more recent report (Ryba et al., 2014), proposed their approach for 3D control of their piezo-driven experimental setup. They also reported their attempts to observer-based compensation of hysteresis and creep nonlinearities as well as pole placement tunneling current control in the ambient conditions (Ryba et al., 2014).

In another work, (Ahmad et al., 2009) proposed an H_∞ controller design procedure to enhance the STM performance. In this work they followed a multivariable control approach to the STM control problem, and described their expectations of system performance in the form of previously user-defined weight functions. Then they constructed a generalized control plant containing the actual system and the weight function. The control problem was then converted to synthesis of a controller which minimizes the infinity-norm of the generalized control plant using the small-gain theorem (Skogestad and Postlethwaite, 2005).

2.2.2 STM tip in-plane positioning

Rather than the tip-sample distance (z-axis) which is feedback-controlled, precise positioning of the tip over sample plane (x-y plane) is also required in order to obtain topographic images. This is more critical in lithography mode where unreliable positioning may result in modification of surface in an undesired location. During the scan process, a rastering tip motion in x-axis as well as a ramp motion in y-axis can generate a scan pattern in x-y plane. While the tip follows this pattern, the Z-axis is feedback controlled, and thus the height of each point on the pattern is obtained which reflects the surface topography. Unfortunately, feedback control of tip position in x-y plane is not possible due to unavailability of sensors with atomic resolutions needed for such process. Thus x-y positioning needs to be conducted in open-loop. In order to insure that the tip follows the given command in x-y plane, the command frequency must be much smaller than the first resonance frequency of scanner (e.g. below 1%)(Clayton and Devasia, 2005). Otherwise, positioning errors are induced in the x-y motion of the tip; a consequence of which is appearance of artifacts in the obtained image. To prevent these artifacts, very slow scanning speed is necessary which limits the STM scanning speed. Clayton and Devasia (Clayton et al., 2009) proposed an image processing technique to compensate for the dynamic effects of the lateral scanner motion. They increased the scanning speed and adjusted the obtained image by further processing.

2.2.3 Noise reduction

Tunneling current is severely prone to noise. Two major sources of such noise is the ambient mechanical noise as well as the measurement noise. Various design and measurement considerations are necessary to limit the induced noise and to increase the signal-to-noise ratio. Most of the techniques implemented so far for noise reduction are passive. Mechanical and acoustic vibration isolation is a prevalent method which is mainly implemented by passive mechanisms such as spring suspension or magnetic damping (Voigtlander, 2015). Designing a compact and stiff mechanical scanner is necessary for noise reduction. Active noise cancellation is an alternative to the passive methods which can significantly reduce the noise level and thus increase the quality of imaging and control of STM. (Liu et al., 2007) proposed an idea for active cancellation of mechanically induced noise in STM. The main concept of their idea is to use the tunneling current as noise sensor due its extreme sensitivity to tip-sample distance. To this aim, they have introduced a double-tip scanner with two tips such close to each other that both of them observe the same mechanical noise. Then, they use the noise measured by one tip to actively cancel the same noise induced in the main tip. See Figure 2.4 for a schematic of this idea.

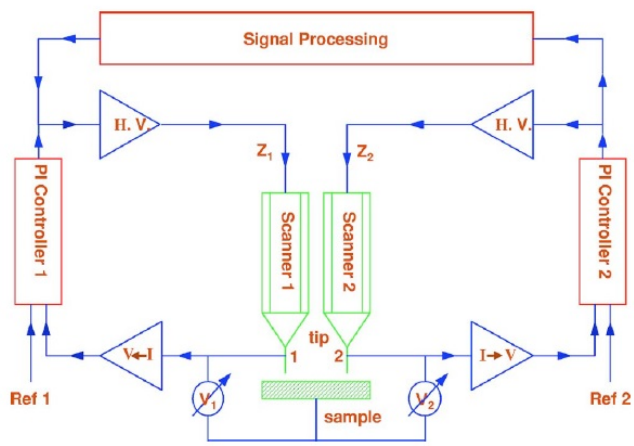

Figure 2.4. Active noise cancellation using double-tip scanner (Liu et al., 2007)

2.2.4 Tunneling current control in other applications

(Blanvillain et al., 2014) described a position sensor based on the tunneling current effect. Figure 2.5 shows the main idea which includes an electrostatically-controlled gold-coated cantilever having the tunneling junction with a sharp piezo-controlled metal tip. The tunneling current control system is similar to that of STM. The gold coating prevents tunneling current fluctuations due to chemical reactions, e.g. oxidation, and facilitates sustaining the tunneling junction in the air. Their strategy for controller design is based on modeling the system in state-space realization, designing a Kalman filter for state estimation from incomplete noisy measurements, and finally synthesis of a robust controller. They validated performance of the designed controller through simulations.

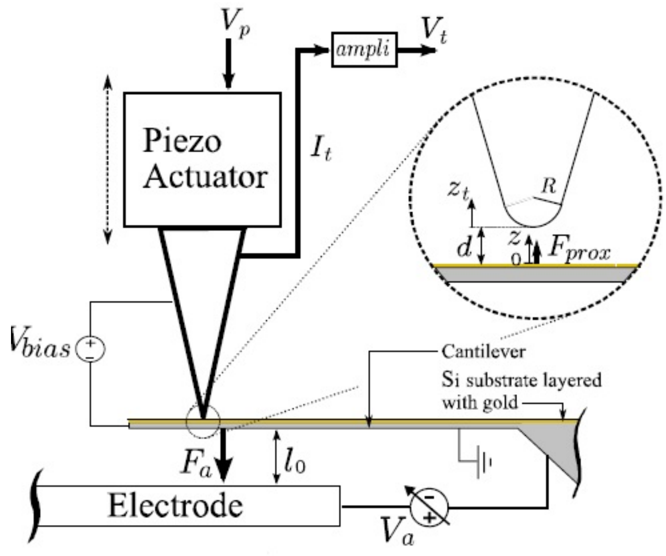

Figure 2.5. Tunneling current based position sensor (Blanvillain et al., 2014)

2.3 Various STM designs

A part from the conventional STMs, some specific applications or performance requirements have imposed specific design of STMs. For instance, demand for probing the quantum characteristics of material (e.g. transport process) motivated the design of multiple tip STMs. (Cai et al., 2007) proposed a dual-tip STM (DSTM) capable of operation between 2 K and room temperature, in a high magnetic field up to 12 T as well as in ultra-high vacuum. They used piezo-driven stick-slip mechanism for coarse positioning and a piezo tube for scanning in the DSTM design which can be used in the transport measurement.

Conducting SPM tests in various environments motivated (Stieg et al., 2008) to design and fabricate a specific SPM device which is capable of operating in electrolyte, air and vacuum. They used piezo tubes for fine positioning the SPM tip, and designed the SPM unit in modular form that can be used for various purposes: AFM or Electrochemical-STM (ECSTM). The STM closed-loop showed first resonance at 2.6 kHz and 1.7 kHz in air and electrolyte, respectively. They attributed this change to the STM tip length which is relatively larger (more than 5 mm) for operation in electrochemical environment and the additional mass of insulating layer (Stieg et al., 2008). A passive damping design provides vibration isolation for their SPM unit. They provided acoustic shielding for their system by lining it with a sandwich-type reflection/absorption barrier composed of vinyl rubber and melamine foam. Thin shields of aluminum provide a Faraday barrier to reduce electromagnetic disturbances (Stieg et al., 2008).

Enabling STM imaging in ultra-low temperatures motivated some specific STM designs. (Troyanovskiy and Roditchev, 2012) proposed an STM which was capable of operating at temperatures down to 4.2 K and in vacuum. Their coarse positioning mechanism was based on a sliding concept which provided positioning accuracy of 10 nm in 4.2 K. A piezo-tube was used for fine positioning.

2.4 Nanopositioning with piezoelectric actuators

Thank to their capability to produce sub-nanometer resolution motion, the piezo-electric actuators are a crucial element of scanning probe microscopy (STM and AFM). Beside their advantages including high resolution and sensitivity, the piezo-electric actuators suffer from a number of drawbacks which makes their implementation a challenging control problem. Nonlinear nature of the actuator due to hysteresis and creep effects is the main challenge. Sharp resonance frequencies and limited range of motion are the other difficulties that arise when using piezo-electric material in SPM. A great body of work has been devoted to address theses challenges and facilitate their application in scanning probe microscopy. For only a few review papers in this field see (Devasia et al., 2007; Cao and Chen, 2014; Clayton et al., 2009; Minase et al., 2010; Fleming, 2013; Yong et al., 2012; Moheimani and Fleming, 2006).

2.5 System identification

In part of our research on the STM control, we will need to perform system identification in order to obtain appropriate models for the system. In general system identification refers to a procedure during which Input/Output data to a system are collected and a mathematical model is fitted to the collected data. In dynamical systems the identification can be performed both in open loop and closed loop. Most of the identification techniques are developed to address the open-loop identification, both in time-domain and frequency domain. A vast body of research are available in this area dating back to early 1990s. In this section we briefly review the literature focusing on the system identification.

2.5.1 Time-domain System identification

(Ljung, 1999) categorized various system identification methods. These methods are applicable to linear and nonlinear, time-variant and time-invariant, static and dynamic systems. A great body of research has been published that benefit from the time-domain methods described there.

2.5.2 Frequency-domain method

The identification process is possible to be conducted in frequency-domain rather than time-domain. To this aim, the collected input /output data are effectively the Frequency Response Data (FRD), and during an identification procedure a dynamic system model is sought to fit the obtained data. (Pintelon and Schoukens, 2012) summarized the latest methods in frequency-domain system identification. Subspace frequency-domain methods have found a lot of applications, and over the past two decades lots of theoretical and applied papers have been published focusing on this topic. For a few samples see (Pintelon, 2002; Noël and Kerschen, 2013; Smith, 2014; Akçay, 2010; Cauberghe et al., 2006; Claes et al., 2007; Döhler and Mevel, 2012).

2.5.3 Closed-loop System Identification

Closed-loop identification has been the subject of extensive research in the past two decades (Forssell and Ljung, 1999; Yan et al., 2015; Pouliquen et al., 2014). The fundamental challenge associated with the closed-loop identification is that the output noise is correlated with the input to the plant due to the feedback (Forssell and Ljung, 1999). Thus, direct identification of the open-loop plant from the closed-loop data is challenging. A large number of research have addressed the challenges of closed-loop system identification (Patwardhan and Goapluni, 2014; Jin et al., 2014; Jammoussi et al., 2013; Rahim et al., 2014; Yan et al., 2015; Pouliquen et al., 2014)

One approach to address this issue is to inject a known signal into the feedback loop and record the output of the plant (which is also the output of the closed-loop system) as well as the input to the plant (which is another output of the closed-loop). The underlying dynamics between the deterministic injected signal and the two measured noisy outputs are the closed-loop systems which are identified without noise-input correlation problem. The open-loop models are later extracted from the identified closed-loop data. This method is known as “the joint input-output approach” (Forssell and Ljung, 1999).

2.6 Conclusion and Research Objective

Our literature review shows that the problem of STM control in general and the tip-sample contact, in particular, have not been well-addressed in the previous research. As mentioned earlier, commonly a PI controller with fixed user-tuned gains is used in commercial STMs. The research background in addressing the STM control challenges is weak.

On the other hand, there is a good body of work devoted to the control of piezo-electric actuators. Since STMs benefit from piezo-electric actuators, most of the findings reported in the literature to deal with the piezo-actuators are applicable to the STM case where needed.

The complicated and nonlinear nature of tunneling current makes the STM problem intrinsically nonlinear and this can negatively affect the performance of any controller. Nevertheless, the tunneling current has not been investigated in detail from a system dynamics point of view.

Our research goal is to address part of the tip-sample contact problem that is associated with the control system performance. To this aim, we need to understand the dynamics of STM and design an appropriate control scheme based on its dynamics. Noting that the tunneling current exists under the feedback control, we must conduct the identification tests in the closed-loop. This can be the first step toward understanding the STM from a system point of view.

In this dissertation, we address the STM control problem by taking a system dynamics approach. By performing closed-loop system identification tests, we find that parameters describing physics of the tunneling current are affecting the closed-loop gain. Therefore, the physics of tunneling current affects the closed-loop stability. To the author's best knowledge, this is the first time that the tunneling current parameters (i.e. the Local Barrier Height) is related to the closed-loop stability of STM. This provides a new insight into the STM control challenges. In the next chapters, we describe the details of our work.

CHAPTER 3

CLOSED-LOOP SYSTEM IDENTIFICATION

3.1 Overview

In this chapter we present our efforts for understanding the STM dynamics and reasons of tip-sample crash. We start with presenting our approach for closed-loop system identification which leads to a new understanding that the a tunneling current parameter known as the local barrier height (LBH) appears to be proportional to the closed-loop gain. Since the LBH is highly variable in STM, we conclude that it can severely affect the stability of the closed loop. We later propose an online method for estimating the LBH on-the-fly and tuning the controller gains for preserving system stability despite LBH variations. We conclude this chapter by presenting experimental results supporting this claim.

3.1.1 Tunneling current and the LBH

Quantum mechanical calculations suggest that the electrical current that is established through the vacuum between the tip and sample is proportional to the applied bias voltage and is an exponential function of the tip-sample separation (Binnig and Rohrer, 2000; Garcia et al., 1983). A simplified tunneling current model is then obtained as (Lang, 1988):

$$i = \sigma V_b e^{-1.025\sqrt{\varphi}\delta} \tag{3.1}$$

where V_b is the bias voltage between the tip and sample, σ is a parameter depending on the material and geometry of the tip and sample, and δ (in $\mathring{A}$) is the energy barrier thickness which is approximately equal to the geometrical tip-sample separation (Lang, 1988). φ (in eV) is called "Work function" or "Barrier Height" which by definition is the minimum energy required to remove an electron from a solid. In quantum physics, energy of electron in vacuum is higher than its energy in solid and this difference, i.e. the Work Function, acts as a barrier preventing electrons from leaving the solid. So the terms Work Function and Barrier Height are close in meaning (Voigtlander, 2015; Binnig and Rohrer, 2000). A pre-amplifier of gain R is used to convert sub-nano-ampere range tunneling current i given by (3.1) to a measurable voltage, the natural logarithm of which is then taken with the aim of linearizing the model. This gives:

$$\ln(Ri) = \ln(R\sigma V_b) - 1.025\sqrt{\varphi}\delta \tag{3.2}$$

which indicates that for constant σ and V_b the logarithm of tunneling current is proportional to the tip-sample separation. This linear relationship between $\ln i$ and δ is crucial to the operation of STM which ultimately maps a surface topography correlated to δ by keeping the current constant using a linear feedback.

Additionally, equation (3.2) suggests that, for constant σ and V_b, the logarithmic derivative of current with respect to the tip-sample separation provides a measure of the barrier height (Binnig et al., 1984; Lang, 1988; Kuk, 1990):

$$\varphi = 0.952 \left(\frac{d}{d\delta} \ln Ri \right)^2 \tag{3.3}$$

In the early STM works, in order to measure φ using equation (3.3), the tip-sample separation δ is modulated by a known frequency $\mathit{\Omega}$. Then, the derivative required in equation (3.3) is obtained by tracking the $\mathit{\Omega}$ component of the logarithm of tunneling current using a Lock-in Amplifier (LIA) (Binnig et al., 1984; Wiesendanger et al., 1987). In the next chapter we will describe an alternative method for measuring φ. It has been understood in the STM community that the barrier height depends on the physical properties of the tip apex as well as those of the sample surface atoms into which the current tunnels (Lang, 1988).

This means that barrier height is a local effect and is subject to change based on variations in the instantaneous and spatial physical properties of the tip and sample. Based on this understanding, parameter φ obtained by the described method can be used to produce another image while scanning a surface. This is referred to as the LBH image, and provides additional information about the physical and chemical surface characteristics (Wiesendanger et al., 1987; Maeda et al., 2004; Binnig and Rohrer, 2000; Jia et al., 1998).

Experimental investigations have also shown that, for the range of tip-sample separation δ at which the STM usually operates, φ is nearly independent of δ (Binnig et al., 1984; Lang, 1988; Maeda et al., 2004). This experimental observation assures that the linearization provided by equation (3.2) remains effective for normal operating ranges of STM. Thus, it is possible to utilize a linear feedback control system to keep the current constant by changing tip-sample distance. In the next sections we discuss the operation of this closed-loop control system and investigate the effect of LBH on the stability and performance of the STM control system.

3.1.2 Closed-loop structure

The effective instantaneous tip-sample gap, δ, can be represented by:

$$\delta = d_{hm} - d_0 - h - d_{tp} \tag{3.4}$$

where d_{hm} represents the tip-sample separation when the tip is at its home position, d_0 stands for changes in the tip-sample gap while scanning due to sample distortion or drift, h is the surface features' height and represents the actual surface topography, and d_{tp} is the tip displacement due to the control command.

Figure 3.1a displays a block diagram of the closed-loop current control system of the STM. δ is converted to a current i through the tunneling current physics. The pre-amplifier

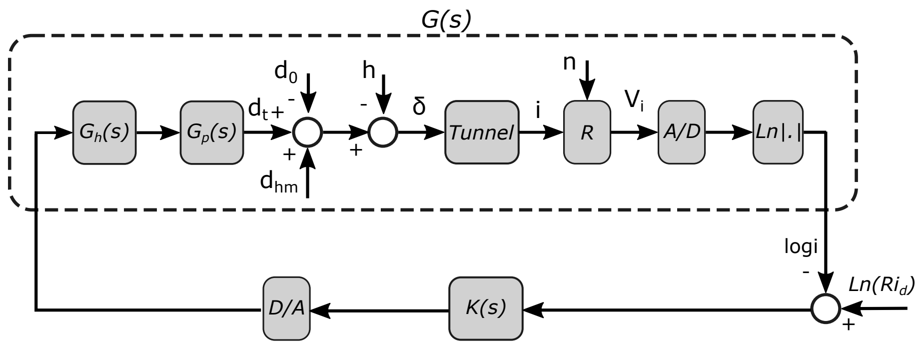

Figure 3.1. Block diagram of the STM Z-axis control system

converts this sub-nano-ampere range current into a measurable voltage V_i which is then sampled by an A/D converter. Natural logarithm of the measured signal is first taken, then it is compared to the logarithm of the setpoint current $\ln(Ri_d)$ to determine the error signal based on which a controller $K(s)$ operates. The control command passes through the D/A converter and the High-Voltage-Amplifier $G_h(s)$, moves the piezo-actuator $G_p(s)$ and modifies δ. While scanning, the surface topography appears as an unknown disturbance h and results in a change in the tunneling current. The controller adjusts the vertical position of the tip to keep the current constant. Thus, the control command maps the surface topography. Misalignment of the sample or drift generates another disturbance d_0 while noise n is mainly generated with current measurement. The STM open-loop model in z-direction is shown by $G(s)$ in Figure 3.1a which represents all the dynamics from control command to *logi* signal.

Assuming a model given by equation (3.1) for the tunneling current and using equation (3.2), the closed-loop control block diagram is simplified as shown in Figure 3.1b. Thus, the square root of φ appears proportional to the feedback loop gain. In the rest of this report we use the simplified block diagram shown in Figure 3.1b for our discussions.

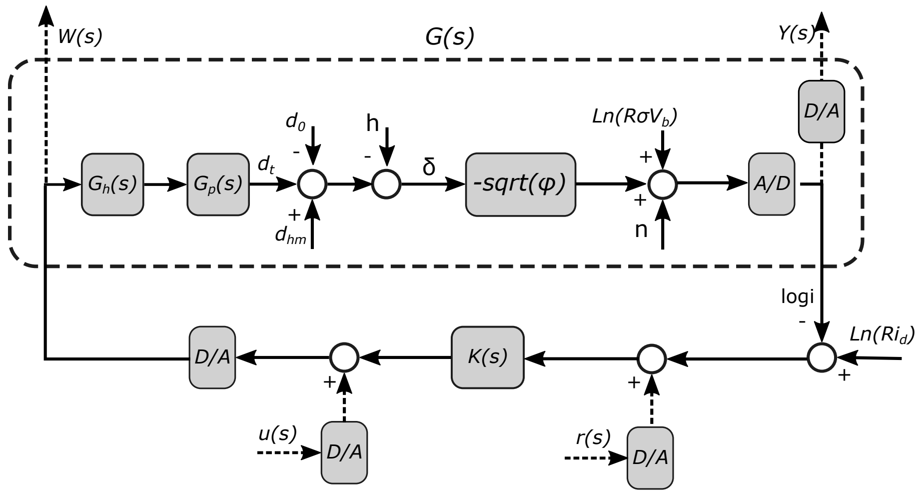

Figure 3.2. Control block diagram with simplified tunneling current model. Exogenous inputs and outputs for identification purposes are shown in dashed arrows.

3.2 Closed-loop System Identification

We conduct identification tests in frequency domain. We inject a sinusoidal identification signal $r(s)$ to the closed-loop setpoint and record the resulting gain and phase at the outputs $Y(s)$ and $W(s)$ (Figure 3.2). Sweeping the frequency of the injected signal, we obtain the Frequency Response Function (FRF) between each I/O pair. Furthermore, we average the measured values at each single frequency point to reduce the measurement noise. We repeat the same procedure by injecting a frequency-sweeping signal $u(s)$ into the controller command and recording the system outputs $Y(s)$ and $W(s)$. Knowing the structure of the feedback loop, the four underlying systems are:

$$G^c_{r2w}(s) = \frac{W(s)}{r(s)} = \frac{z(s)K(s)z(s)}{1 + K(s)z(s)G(s)} \tag{3.5}$$

$$G^c_{r2y}(s) = \frac{Y(s)}{r(s)} = \frac{z(s)K(s)z(s)G(s)z(s)}{1 + K(s)z(s)G(s)} \tag{3.6}$$

$$G^c_{u2w}(s) = \frac{W(s)}{u(s)} = \frac{z(s)z(s)}{1 + K(s)z(s)G(s)} \tag{3.7}$$

$$G^c_{u2y}(s) = \frac{Y(s)}{r(s)} = \frac{z(s)z(s)G(s)z(s)}{1 + K(s)z(s)G(s)} \tag{3.8}$$

where $z(s)$ describes the zero-order-hold model of the A/D and D/A blocks. Closed-loop FRFs (3.5)-(3.8) immediately result from the I/O measurements. In order to obtain the open-loop model $G(s)$, required for control design purposes, we can divide the obtained closed-loop FRFs at each frequency point to obtain:

$$G_1(s) = \frac{G^c_{u2y}(s)}{G^c_{u2w}(s)} = z(s)G(s) \tag{3.9}$$

$$G_2(s) = \frac{G^c_{r2y}(s)}{G^c_{r2w}(s)} = z(s)G(s) \tag{3.10}$$

Having a fixed sampling frequency, $z(s)$ is known and thus both $G_1(s)$ and $G_2(s)$ represent the same open-loop dynamics $G(s)$ after a further division by $z(s)$, and thus (3.9) and (3.10) are expected to match over a wide frequency range. We can also obtain the controller dynamics $K(s)$ by dividing (3.5) by (3.7) and (3.6) by (3.8):

$$K_1(s) = \frac{G^c_{r2w}(s)}{G^c_{u2w}(s)} \tag{3.11}$$

$$K_2(s) = \frac{G^c_{r2y}(s)}{G^c_{u2y}(s)} \tag{3.12}$$

This can be used for validation purposes since the dynamics of the controller are already known. It is worth noting that: i) to avoid the appearance of nonlinearities in *logi*, and ii) to prevent tip-sample crash due to large oscillations near resonance frequencies, and also iii) to maintain good signal-to-noise ratio during the tests, the frequency range of interest is divided into several intervals over which the amplitude of the input signal is adjusted properly. For more discussion on the procedure and typical results see (Tajaddodianfar et al., 2016).

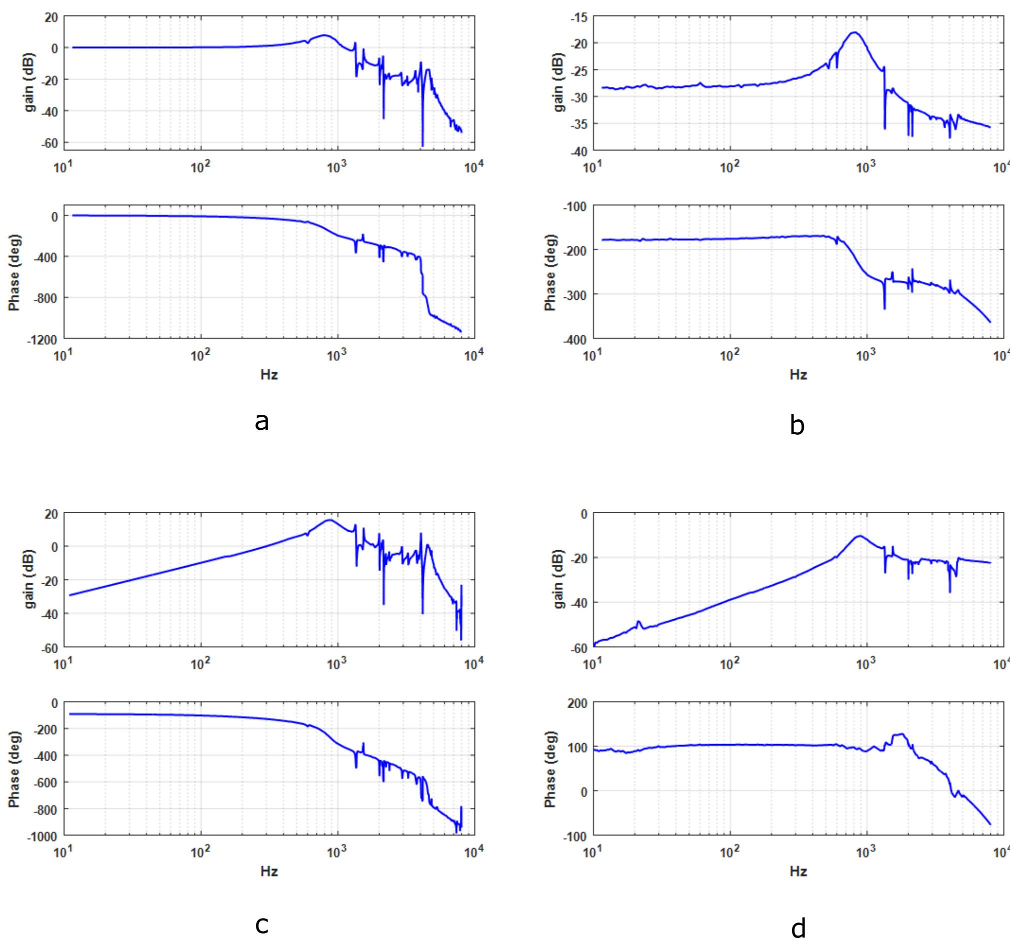

Figure 3.3. Experimental frequency response functions (FRFs) of closed-loop systems, a) G_{r2y}, b) G_{r2w} , c) G_{u2y}, d) G_{u2w}

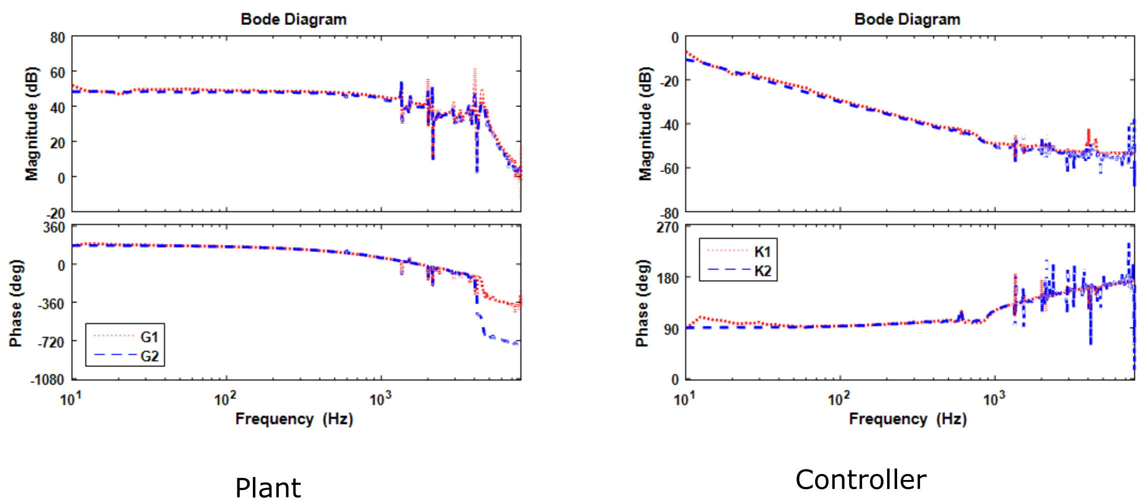

Figure 3.4. Obtained open-loop FRFs for the plant (equations 3.9 and 3.10) and the controller (equations 3.11 and 3.12).

3.2.1 Various identified systems

Once the open-loop FRF is obtained, a transfer function (TF) model is fitted to the measured data to derive a mathematical model of the system dynamics. Depending on the type of the scanner used in the STM, the obtained results are different, as presented next.

Lyding Scanner

Figure 3.5 shows a typical experimental FRF of the STM with Lyding scanner and the model fitted to it. Only dominant resonances are considered while fitting the model which is obtained as:

$$G(s) = \frac{Ce^{-Ts}}{\left(1 + \frac{s}{2\pi\omega_0}\right)} \prod_{i=1}^{N} \frac{1 + 2\zeta_i \left(\frac{s}{2\pi f_i}\right) + \left(\frac{s}{2\pi f_i}\right)^2}{1 + 2\eta_i \left(\frac{s}{2\pi\omega_i}\right) + \left(\frac{s}{2\pi\omega i}\right)^2} \tag{3.13}$$

with $C = 213$, $T = 80\mu s$, $\omega_0 = 1000Hz$ and other parameters are given in Table 3.1:

Table 3.1. Identified parameters for the Lyding Scanner

i	1	2	3	4	5
ω_i(Hz)	468	1520	1880	2780	4010
η_i	0.004	0.011	0.001	0.002	0.002
f_i(Hz)	456	1490	1890	3810	4100
ζ_i	0.003	0.010	0.002	0.001	0.001

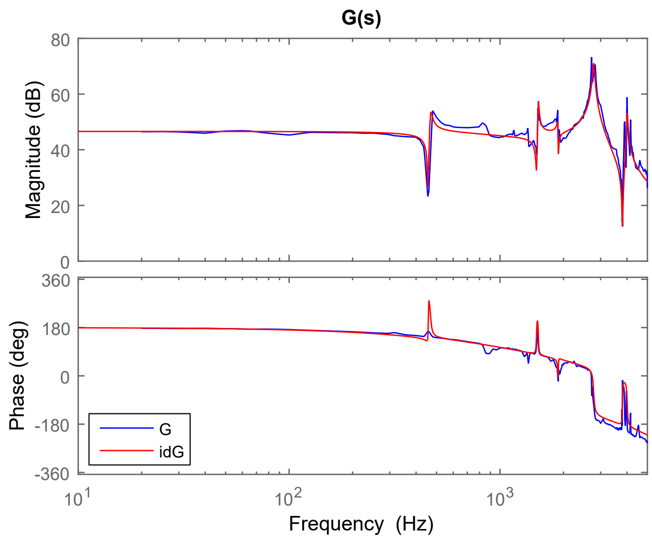

Figure 3.5. FRF of the open-loop model G(s) and the identified TF model for the Lyding scanner

Pyadkin Scanner

Figure 3.6 shows a typical experimental FRF of the STM with Pyadkin scanner and the model fitted to it. Only dominant resonances are considered while fitting the model which is obtained as:

$$G(s) = CG_0(s) = \frac{Ce^{-Ts}\left(\frac{1}{2\pi f_0}s+1\right)}{\frac{1}{2\pi p_0}s+1} \times \prod_{m=1}^{N} \frac{\left(\frac{s}{2\pi f_m}\right)^2 + 2\zeta_m\left(\frac{s}{2\pi f_m}\right)+1}{\left(\frac{s}{2\pi p_m}\right)^2 + 2\eta_m\left(\frac{s}{2\pi p_m}\right)+1} \tag{3.14}$$

with $C = 56.9dB$, $T = 70\mu s$, $p_0 = 1.1kHz$, $f_0 = 11kHz$, and other parameters given as Table 3.2.

Table 3.2. Identified model parameters

m	1	2	3
$p_m(kHz)$	8.25	9.11	12.2
$\eta_m \times 1000$	5.0	3.5	25
$f_m(kHz)$	8.65	9.69	–
$\zeta_m \times 1000$	8.5	15	–

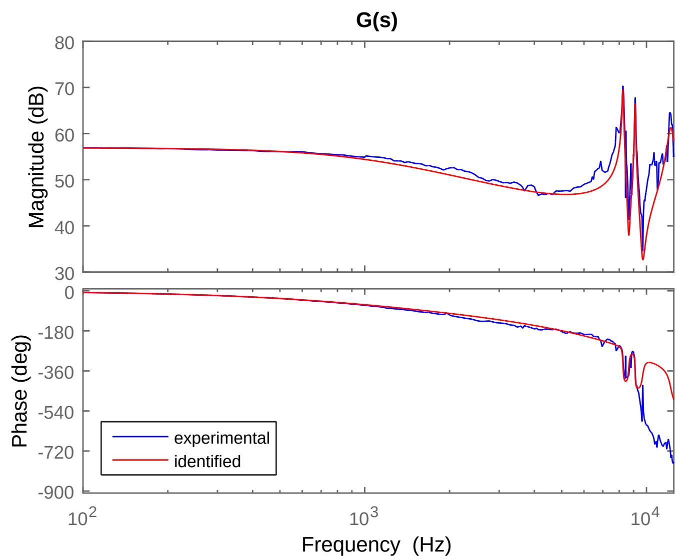

Figure 3.6. FRF of the open-loop model G(s) and the identified TF model for the Pyadkin scanner

Omicron Scanner

Figure 3.7 displays a typical FRD obtained using the Omicron scanner and a transfer function fitted to it. The TF model is obtained as:

$$G(s) = \frac{-7.57 \times 10^8(s^2 - 64550s + 1.35 \times 10^9)}{(s + 13270)(s + 3135)(s^2 + 2853s + 2.418 \times 10^7)} \tag{3.15}$$

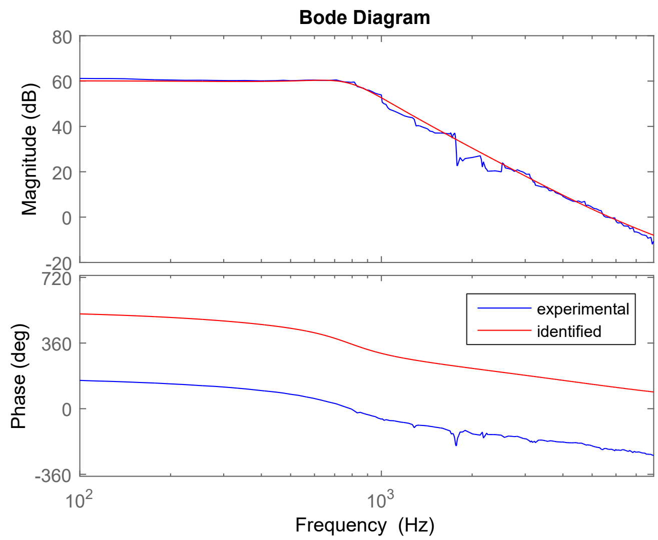

Figure 3.7. FRF of the open-loop model G(s) and the identified TF model for the Omicron scanner

3.3 Model Uncertainties

One point to be considered about the model (3.14) or similar open-loop STM transfer functions is that some of the model parameters are subject to variation every time the STM is operated. For instance, after each tip-replacement and due to the mechanical displacement of the tip holder in the scanner, the resonance frequencies are expected to change. In order to obtain an estimate of the range of variation of resonance frequencies, we performed the identification tests over several different days. Results have shown that uncertainty in resonance frequencies are not more than 10% of their nominal value. Nevertheless, after the current is established the resonance frequencies are kept fixed since there is no significant mechanical motion in the tip holder once the tip and sample are engaged.

Comparing FRF models of $G(s)$, obtained from different tests, we observed that the DC gain of the open-loop model $G(s)$ represented by parameter C in (3.14) is also subject to change. The observed range is 48-60 dB for the existing STM. Referring to the simplified block diagram shown in Figure 3.1b we note that the DC gain of $G(s)$ is given by:

$$C = -1.025\sqrt{\varphi}A_H\gamma \tag{3.16}$$

where A_H is the DC gain of $G_h(s)$ and represents the constant high-voltage amplifier gain ($A_H = 13.5$ in our setup). Also, γ is the DC gain of the piezo-actuator model $G_p(s)$ and describes the piezo-actuator displacement in reaction to a DC voltage applied to it. γ depends on the piezo-actuator material and configuration. In STM it is usually estimated by a calibration procedure through which the height of atomic steps on a sample obtained from STM images are compared to their already-known values. γ is also a constant parameter, and therefore, we may attribute observed variations in parameter C to the changes in parameter φ which represents the local barrier height (LBH) as discussed in section 3.1.1.

Based on our observations, we can distinguish two types of STM tips based on DC gain variations. The first type, called stable tip, generates small variations in the system DC gain, while the second one, called unstable tip, generates significantly higher variation in the open-loop DC gain. Having a stable tip, the STM can generate high-resolution images while after a possible tip-sample crash the tip becomes unstable and the quality of image is reduced. By looking at the DC gain of the open-loop function we can distinguish between stable and unstable tips. Figure 3.8 displays the measured open-loop FRD $G(s)$ for the two cases of stable tip (before crash) and unstable tip (after crash). Ideally, the system FRF must show a constant magnitude up to the bandwidth frequency where it drops by 3 dB. However, mainly due to the tip-change issue, the low frequency portion of the FRF is not constant. Indicating that for measurements of Figure 3.8 we have used 50 times of averaging, we expect lower effect of noise in this range. Early theoretical investigations in STM have shown that the LBH is dependent on tip characteristics (Lang, 1988). In section 4.6.1 we will show our time-domain measurements which confirm that the LBH is affected by tip change.

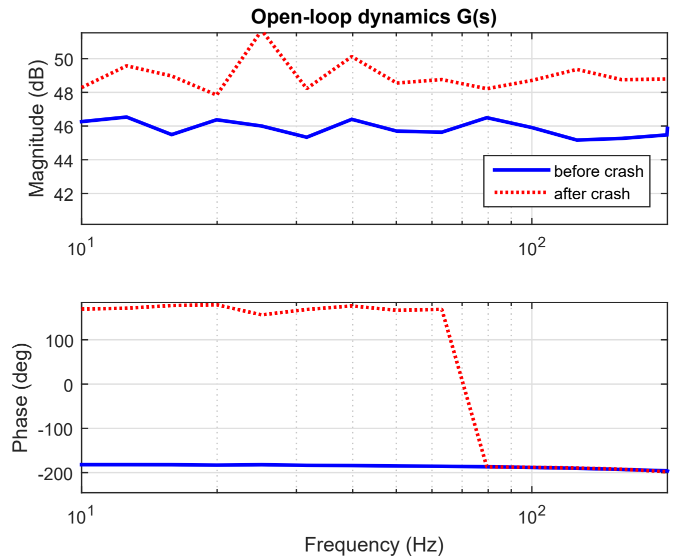

Figure 3.8. Low frequency part of the open-loop function $G(s)$ before and after tip crash. The tip is stable before crash with a magnitude variance of 0.02 dB, while after crash the tip becomes unstable characterized by a 1.8 dB variance in magnitude at frequencies lower than 40 Hz.

LBH depends on many local properties of both the tip and the sample. Thus, during STM scanning when the tip rasters over the sample and meets different local atomic configurations and features with various electronic properties, the parameter φ is subject to change. Moreover, LBH is dependent on the tip conditions (Binnig and Rohrer, 2000); therefore, tip-change which is a very common effect in STM may cause variations in φ. Regardless of the origin of LBH variations, one can find out from (3.16) that φ directly affects the closed-loop gain. Thus, LBH variations influence the closed-loop bandwidth and the overall robustness of the closed-loop system. The proportional and integral gains of a PI controller affect the closed-loop performance and stability, in the same way. This is discussed next.

3.4 Stability and Performance Analysis

We use the open-loop transfer function model given by (3.14) along with a Proportional-Integral (PI) controller to analyze the closed-loop stability and performance of the existing

STM. A digital PI controller is implemented in the STM with the sampling frequency of 50 kHz. The corresponding continuous-time controller transfer function is:

$$K(s) = k_i \left(\frac{1}{s} + \frac{1}{\omega_c} \right) \tag{3.17}$$

where k_i and ω_c represent the integrator gain (in sec^{-1}) and the corner frequency of the controller (in rad/s), respectively. In order to evaluate the effects of the two controller parameters, we first define the closed-loop stability and performance criteria, as follows.

3.4.1 Stability

A loop transfer function of the system assuming a unit integrator gain is given by:

$$G_{lp}(s) = \left(\frac{1}{s} + \frac{1}{\omega_c} \right) G(s) \tag{3.18}$$

For a bounded topography disturbance at the sample surface, the tip displacement must stay bounded. This requires the loop transfer function of the system, $K(s)G(s)$, to maintain a positive Gain Margin (GM) and Phase Margin (PM). For a given ω_c, an integrator gain equal to the GM of the transfer function (3.18) puts the closed-loop system in the marginal stability. Thus, for stability it is required to have $k_i < GM\left\{G_{lp}(s)\right\}$:

3.4.2 Bandwidth

The closed-loop system must be fast enough to track the surface topography while scanning. The required bandwidth depends on the scanning speed as well as the surface topography of the sample. Faster scanning requires higher bandwidth to track the same features. A bandwidth of around 100 times the rastering frequency is normally required. A closed-loop transfer function representing imaging functionality of the STM can be defined as:

$$G_{img}(s) = \frac{CK(s)}{1 + K(s)G(s)} \tag{3.19}$$

Bandwidth of the system given by equation (3.19) determines the closed-loop bandwidth.

3.4.3 Suppressed ringing

While the closed-loop system response must be stable and fast to track the surface features, it should not result in undesired overshoot and fluctuations. Considering the highly resonant nature of piezo-scanner, the control system should not excite the resonances; otherwise, the risk of tip-sample crash will significantly increase and the STM image quality will be negatively affected. To ensure these requirements, the infinity norm of the imaging transfer function (3.19) must stay below a pre-defined threshold. By definition, the infinity norm is the maximum of the magnitude of a transfer function over all frequencies:

$$\|G_{img}(s)\|_{\infty} = \max_{\omega \in \mathbb{R}} \{|G_{img}(j\omega)|\} \tag{3.20}$$

3.4.4 Appropriate PI gains

The proposed stability and performance criteria define three curves in the PI controller parameter space. Selecting a value for ω_c, the gain margin of system (3.18) determines the critical integrator gain which puts the system in marginal stability. Repeating the procedure for various values of ω_c a curve shown with solid line in Figure 3.9a is obtained, to the left of which the stability criterion is satisfied. Also, selecting a desired closed-loop bandwidth ω_{BW} as well as a corner frequency ω_c, an integrator gain k_i is found such that the system (3.19) will have a bandwidth of ω_{BW}. Repeating the procedure for various ω_c values, a curve in the controller parameter space is obtained, to the right of which the bandwidth criterion is satisfied, as shown in dotted curve in Figure 3.9a. Selecting a desired maximum infinity norm, which puts the closed-loop system in the ringing edge, and solving the nonlinear closed-loop equation for k_i, one ends up with the dashed curve in Figure 3.9a, to the left of which criterion 3.4.3 is satisfied. As ω_c gets larger, the proportional gain of the controller becomes smaller and the controller approaches a pure integrator. So, for large ω_c values the critical integrator gain is independent of ω_c. Considering all three criteria, Figure 3.9a suggests that the PI gains must be selected in the colored area to ensure stability, fast and safe performance of the closed-loop system. Manual tuning of STM PI gains involves selecting an appropriate value for ω_c ,increasing k_i gain so that ringing is observed in the current signal. Then, half of the corresponding k_i gain is selected as the operational value. In Figure 3.9a it is assumed that undesired oscillations appear when the closed-loop gain at resonance frequency is 5 dB larger than its DC value, and the black dashed-dotted curve corresponds to the conventional PI tuning method.

We have observed that parameter C in (3.14) takes different values spanning approximately 10 dB in range. This large amount of variation in C can easily affect the stability and performance of the STM for which PI gains are already tuned. For instance, Figure 3.9b shows stability and performance curves for the same system as shown in Figure 3.9a but with parameter C being 6 dB higher. It is clear in Figure 3.9b that the appropriate PI gain area significantly shrinks for higher DC gains, and it is quite possible for a set of appropriate PI gains for the system with $C = 53.1dB$ to result in ringing or instability when the the DC gain soars to $C = 59.1dB$ due to some physical reason. This observation suggests that once the PI gains are tuned and fixed, model variations rooting in physics of the tunneling current, i.e. the LBH variations, may deteriorate system performance or stability. We believe this to be a key cause of the tip-sample crash and tip-change in STM which critically limits the performance of the instrument both in imaging and nano-lithography applications. This provides enough motivation for us to propose an algorithm for online estimation of the LBH and accordingly tuning of the PI gains for enhanced system stability. This is discussed in the next chapter.

3.4.5 Experimental validation

In order to validate the stated criteria, we performed further experimental tests. After conducting system identification tests which resulted in a plant transfer function model similar to 3.14, we changed the controller corner frequency ω_c and starting from a small value we kept increasing the k_i gain. While doing so, we kept track of the highest resonance peak appearing in the FFT of the tunneling current, which grows with k_i gain. We recorded the value of k_i which puts the highest FFT peak at a 10 dB equivalent level. Repeating the procedure for various ω_c values, we obtained results shown in Figure 3.10. Parameter C prior to these tests was measured as $C = 45.5dB$. Observations showed that for $\omega_c < 5krad/s$ harmonics of resonance frequencies appear in the system output suggesting that the nonlinear effects are dominant. This is consistent with the fact that small gain of PI controller at higher frequencies is responsible for minimizing the effect of nonlinearities in the system response. With a small corner frequency, the high frequency gain of the PI controller will be too large to sufficiently reduce the nonlinear effects.

Furthermore, we fixed PI corner frequency at $\omega_c = 10krad/s$ and measured the integrator gain putting the system at 10 dB threshold while the parameter C was measured at different conditions. Results are depicted in Figure 3.11 showing a good agreement between theoretical and experimental results.

3.5 Concluding Remarks

In this chapter we used closed-loop system identification to study the STM dynamics, and showed that the DC gain of open-loop model is affected by the LBH. Given that LBH is a variable depending on the electronic properties of the tip and sample, the overall feedback loop gain is subject to change when scanning. Observations show that due to possible large variations in LBH, the closed-loop system may experience ringing or instability if the PI gains are kept fixed.

This gives us a motivation to estimate the plant DC gain (i.e. the LBH) on-the-fly and compensate for its adverse effects by adjusting the PI gains. This is discussed in the next chapter.

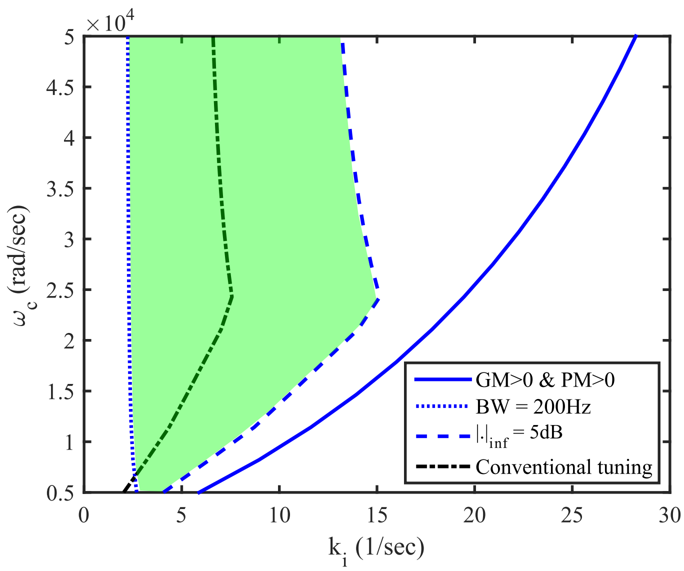

(a)

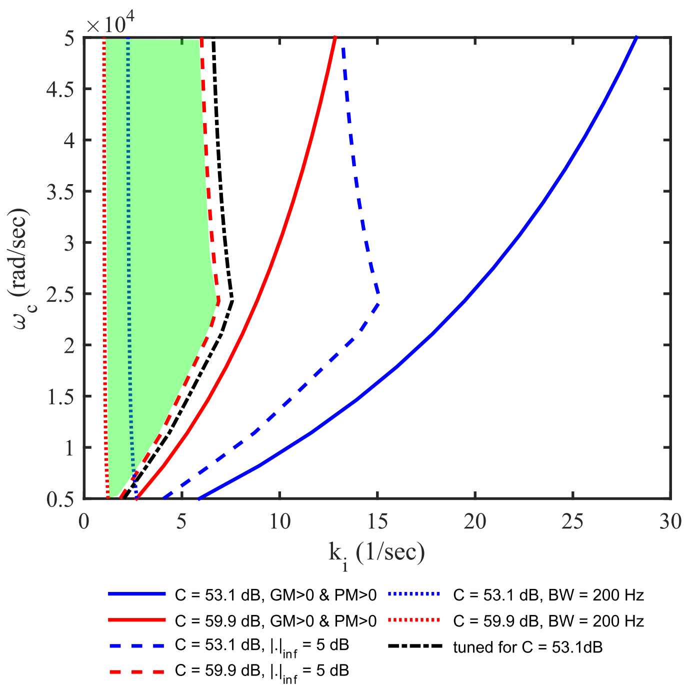

(b)

Figure 3.9. a) Critical Stability and performance curves in the PI controller parameter space for a plant with $C = 53.1dB$. Conventional tuning curve is shown as the black dashed-dotted curve, and shaded area displays appropriate PI gains. b) Shrinkage of the appropriate PI gains area for higher plant DC gain values.The tuned PI gains curve in (a) is outside of the shaded appropriate area for the higher DC gain value in (b).

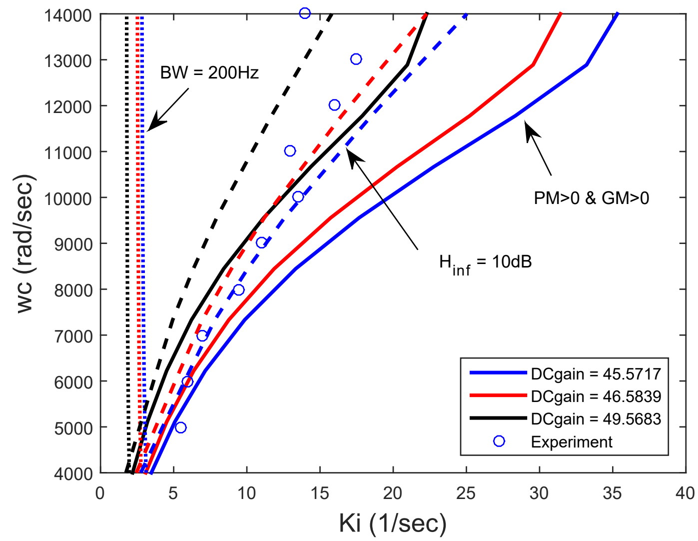

Figure 3.10. Stability and performance curves in the parameter space of the PI controller for three different model DC gain values. Circles denote experimental results. Theoretical and experimental results obtained using identified STM model with Lyding scanner.

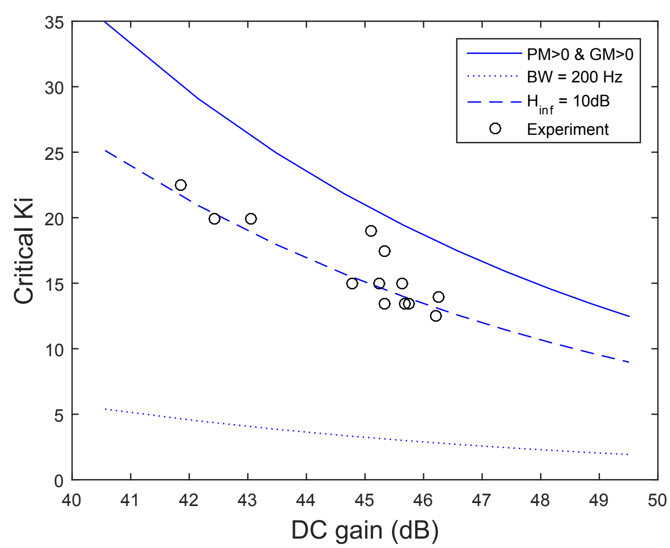

Figure 3.11. Critical values of integrator gain k_i versus model DC gain given by the stability and performance criteria with fixed $\omega_c = 10krad/s$. Circles denote experimental results. Theoretical and experimental results obtained using identified STM model with Lyding scanner.

CHAPTER 4
PI-TUNING BASED ON LBH ESTIMATION WITH APPLICATIONS IN IMAGING

4.1 Overview

In Chapter 3 we showed that due to large variations of LBH the closed-loop system may experience stability issues. In this chapter we present a method for estimating the LBH on-the-fly and use the obtained estimation to continuously adjust the gains of PI controller.

We present experimental results showing that the LBH is a variable parameter and that adjusting PI gains improves the closed-loop stability. Furthermore we compare our method for LBH estimation with the method that is conventionally used in STM literature and show that our method gives more accurate and reliable results. In this chapter we focus on the imaging mode, and leave the lithography mode for Chapter 5.

4.2 Local Barrier Height Estimation

In this section we propose an algorithm for online estimation of the open-loop DC gain parameter given by C in equation (3.14). Referring to Figure 3.1b we need to inject a harmonic identification signal with fixed known frequency represented by $r(s)$ or $u(s)$ into the closed-loop system and track the amplitude of the corresponding component in the system outputs $Y(s)$ and $W(s)$. The main part of the algorithm is an amplitude estimator which is capable of estimating and tracking the amplitude of a known carrier frequency in a noisy background. The Lock-in Amplifier (LIA) is the most common method being used for this purpose. In LIA the signal to be tracked which contains an Ω component is multiplied by $\sin(\Omega t)$ and $\cos(\Omega t)$ shifting the carrier frequency to DC and leaving a 2Ω component along with a large Ω component for signals with DC bias. Signals fed to LIA are AC coupled first to remove the DC bias and are passed through a Low-pass Filter (LPF) after multiplication by $\sin(\Omega t)$ and $\cos(\Omega t)$. However, due to the large 2Ω component, bandwidth of the LPF is limited and this also limits tracking capability of the filter. The problem can be alleviated by using an LPF with sharper roll-off which needs higher filter orders. Here, we use another method which is found to perform as efficiently as the LIA but has a smaller order and is easier to implement.

4.3 Mathematical Tools

4.3.1 Lock-in Amplifier

A Lock-in Amplifier (LIA) is also possible to be used for tracking the amplitude of the $\varOmega$-component in the response signals. Assume that the measured signal is a composition of a range of different frequency components:

$$x(t) = a_0 + \sum_{i=1}^{\infty} \left(a_i \cos\left(\omega_i t + \psi_i\right)\right) + n \tag{4.1}$$

with n representing wide-band measurement noise. Assuming the frequency of interest to be $\omega_1 = \varOmega$, we are interested in determining a_1. The LIA algorithm starts with modulating the measured signal using $sin(\omega_1 t)$ as below:

$$\begin{aligned} x_s(t) &= a_0 \sin\left(\omega_1 t\right) + \sum_{i=1}^{\infty} \left(a_i \cos\left(\omega_i t + \psi_i\right) \sin\left(\omega_1 t\right)\right) + n \sin\left(\omega_1 t\right) \\ &= -\frac{1}{2} a_1 \sin\left(\psi\right) + a_0 \sin\left(\omega_1 t\right) + \frac{1}{2} a_1 \sin\left(2\omega_1 t + \psi\right) + n \sin\left(\omega_1 t\right) \\ &+ \sum_{i=2}^{\infty} \frac{1}{2} a_i \left(\sin\left(\left(\omega_i + \omega_1\right) t + \psi_i\right) - \sin\left(\left(\omega_i + \omega_1\right) t + \psi_i\right)\right) \end{aligned} \tag{4.2}$$

after passing $x_s(s)$ through a low-bandwidth sharp low-pass filter, all dynamic terms in (4.2) are suppressed and we are left with a static component as:

$$x_{ss}(t) = -\frac{1}{2}a_1 \sin(\psi) \tag{4.3}$$

At the same time, LIA modulates (4.1) by $\cos(\omega_1 t)$ and low-pass filter it. The following static term is then obtained:

$$x_{cs}(t) = \frac{1}{2}a_1 \cos(\psi) \tag{4.4}$$

Using (4.3) and (4.4) LIA gives a_1 as:

$$a_1 = 2\sqrt{x_{ss}^2 + x_{cs}^2} \tag{4.5}$$

To track variations of a_1 we are interested in higher bandwidth of low-pass filters; however, the higher the bandwidth of low-pass filters the more noisy estimation. So, we have to compromise between accuracy and bandwidth of estimation. Also, for lowering a_0 in (4.1) which appears as the coefficient of ω_1 component in (4.2), we should AC couple the measured signal by passing it through a high-pass filter to suppress its DC and very low-frequency components.

4.3.2 Lyapunov Filter

Assume that the carrier signal has a known frequency $\varOmega$ and unknown amplitude and phase as below:

$$x(t) = X \sin(\varOmega t + \psi) \tag{4.6}$$

We can re-write (4.6) as the product of a parameter vector $\boldsymbol{\theta}$ and a known regressor vector $\boldsymbol{\varPhi}$:

$$x(t) = \boldsymbol{\theta\varPhi(t)} \tag{4.7}$$

where $\boldsymbol{\theta} = [X_1, X_2] = [X\cos(\psi), X\sin(\psi)]$ and $\boldsymbol{\Phi(t)} = [\sin(\Omega t), \cos(\Omega t)]^T$. Considering $\bar{\boldsymbol{\theta}} = [\hat{X}_1, \hat{X}_2]$as an estimate of the parameter vector $\boldsymbol{\theta}$, the corresponding estimate of $x(t)$ is given by $\hat{x}(t) = \bar{\boldsymbol{\theta}}\boldsymbol{\Phi}$. The estimation error is then defined by $\epsilon(t) = x(t) - \hat{x}(t)$, based on which the following estimator dynamics is constituted:

$$\frac{d}{dt}\bar{\boldsymbol{\theta}} = \epsilon\boldsymbol{\Gamma}\boldsymbol{\Phi} \tag{4.8}$$

where $\Gamma = diag(\gamma)$ for some $\gamma > 0$ known as the adaptive gain. The adaptive law (4.8) guarantees that $\hat{X}_1, \hat{X}_2, \epsilon \in L_\infty$ and that $\frac{d}{dt}\hat{X}_1, \frac{d}{dt}\hat{X}_2 \in L_2$. Given that $\boldsymbol{\Phi}$ is Persistently Exciting (PE), we can show that $\frac{d}{dt}\hat{X}_1, \frac{d}{dt}\hat{X}_2 \in L_\infty$ as well, and this immediately implies that the estimated parameter vector $\bar{\boldsymbol{\theta}}$ converges to $\boldsymbol{\theta}$ exponentially fast (Ioannou and Sun, 1996). Thus, at each time t, an estimate of the amplitude and phase of the Ω-component of the measured signal is given by:

$$\hat{X} = \sqrt{\hat{X}_1^2 + \hat{X}_2^2}, \quad \psi = \arccos\left(\tfrac{\hat{X}_1}{\hat{X}}\right) \tag{4.9}$$

The parameter γ determines the convergence speed of the estimator. For large γ, the filter has a high-bandwidth and fast tracking which also lets more noise into the estimation, while smaller γ gives smoother but slower estimation. Thus, γ remains as a tunable parameter of the filter which enables the user to strike a trade-off between filter bandwidth and estimation accuracy.

The frequency Ω of the identification signal $r(j\Omega)$ should be greater than the required closed-loop bandwidth so that it would not adversely affect the useful topography information which exist at low frequencies. In addition, Ω should be small enough to avoid exciting resonance frequencies of the scanner. For the existing STM which requires a closed-loop bandwidth of a few hundred hertz and has its smallest resonance frequency near 8 kHz, we select $\Omega = 1kHz$ as the frequency of the identification signal. The closed-loop outputs are measured as $Y(s)$ and $W(s)$, as shown in Figure 3.1b, and contain DC and low-frequency components as well as wide-band noise and high-frequency components. However, for LBH estimation we are interested only in their Ω-component. Thus, we pass the measured signals through a band-pass filter (BPF) centered at Ω before sending them to the Lyapunov filter. The pass band of this filter relates to the noise-bandwidth trade-off of the LBH estimator, as well. However, since the maximum bandwidth of LBH estimation cannot be greater than the close-loop bandwidth, we assign a fixed 3 dB pass band of 300 Hz around the center frequency of 1 kHz to the BPF, and keep parameter γ as the only tunable parameter. Figure 4.1 displays the magnitude response of the implemented digital Butterworth BPF.

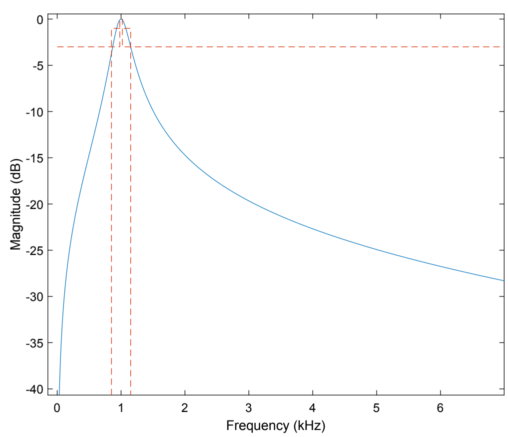

Figure 4.1. Magnitude response of the implemented Butterworth IIR band-pass filter BPF.

4.4 LBH estimation

4.4.1 Conventional LBH Measurement Method

It is well-known that assuming a constant small bias voltage V with a one dimensional square barrier of height φ above the Fermi level results in a simplified tunneling current model (Lang, 1988):

$$i \propto V \exp\left(-1.025\delta\sqrt{\varphi}\right) \tag{4.10}$$

where δ in $\mathring{A}$ is the barrier thickness and is approximately equal to the tip-sample separation. The barrier height φ is also a function of δ and $\varphi(\delta) \to \Phi$ as $\delta \to \infty$, i.e. the barrier height approaches the sample surface work function Φ as the tip-sample separation increases. Theoretical and experimental investigations have shown that in the typical working ranges of STM, $\varphi(\delta)$ is almost independent of δ (Binnig et al., 1984). Therefore, in such ranges a linear relationship holds between the logarithm of tunneling current ($\ln i$) and the tip-sample separation δ. This allows for the implementation of a linear feedback control system to keep the current i at a constant setpoint i_d by adjusting the relative distance between the tip and the sample. The assumption that φ is independent of δ in the working range immediately converts equation (4.10) to the following relation that makes it possible to measure the barrier height:

$$\varphi \propto \left(\frac{d \ln i}{d\delta}\right)^2 \tag{4.11}$$

Equation (4.11) indicates that rate of change of $\ln i$ with respect to the separation δ is proportional to the square root of the barrier height.

The gap modulation method was introduced in the early STM works to measure φ based on equation (4.11). In this method, a modulating signal at frequency Ω is added to the piezo-tube drive and forces the tip to oscillate in the direction normal to the sample. It is assumed that the oscillation amplitude of δ at that frequency is fixed because Ω is beyond the bandwidth of the controller. Then only tracking the amplitude of $\ln i$ at Ω using a lock-in amplifier will suffice to calculate φ.

The barrier height obtained by equation (4.11) is a quantity that depends on the surface local electronic properties as well as those of the tip. Hence, the terminology Local Barrier Height (LBH) or the Apparent Barrier Height is used. This measurement is a basis to generate another STM image called the LBH image which is found to be capable of presenting additional details regarding the surface physics. However, the basic assumption which validates the gap-modulation method is not always correct. In fact, even if Ω is beyond the bandwidth of $K(s)$ there is always a portion of $\ln i$ at Ω which passes through the controller $K(s)$ and adds up to δ that is modulated at Ω. This means that $\ln i$ influences δ at frequency Ω and this effect becomes more profound when i) larger modulation amplitudes are employed to gain a better signal-to-noise ratio, ii) larger controller bandwidth is required for fast imaging, and iii) large variations in $\ln i$ at Ω occur. Under these circumstance, the denominator of equation (4.11) can no longer be assumed to be a constant and this may affect the measured LBH values.

In the next section, we first discuss the effect of LBH on the controller stability and performance, and then we propose an alternative approach to LBH measurement to circumvent the above issues.

4.4.2 LBH Effects On Control System Performance

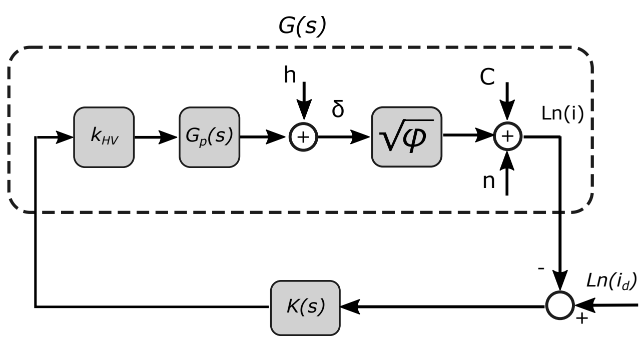

Figure 4.2. Simplified Z-axis control block diagram showing the LBH as a parameter that affects DC gain of open-loop plant $G(s)$.

Equation (4.11) shows that the LBH can be considered, mathematically, as a gain which maps the tip-sample gap (δ) into the logarithm of current ($\ln i$). Knowing that the current control system uses $\ln i$ as the feedback signal and adjusts δ by a control signal, it can be shown that the LBH is directly affecting the DC gain of the open-loop STM dynamics that is being controlled. There are other parameters that contribute to the plant DC gain, e.g. the high-voltage amplifier gain and piezo-material sensitivity. However, all of these parameters are fixed. In addition, it can be assumed that any dynamic drop due to the scanner and filter dynamics at the frequency of modulation is fixed. These assumptions are based on the closed-loop system identification tests performed on the STM which has been discussed in the authors previous reports including (Tajaddodianfar et al., 2016, 2017) and (Tajaddodianfar et al., 2017).

Figure 4.2 displays a simplified block diagram of the STM Z-axis control. Here, $G(s)$ and $K(s)$ are the open-loop plant and controller dynamics, respectively. k_{HV} is the high-voltage amplifier gain and $G_p(s)$ is the piezo-scanner dynamics in Z-direction. Surface topography, constant logarithm terms and measurement noise are represented by h, C and n, respectively, and i_d is the current setpoint.

It is well-known in that the DC gain of the open-loop plant is a critical factor in the closed-loop stability and performance of the system. Since the DC gain is a function of the LBH value, the STM stability can be violated if the LBH experiences substantial variations. In (Tajaddodianfar et al., 2017) and Chapter 3, we presented experimental results which suggested that the DC gain may vary by a factor of two due to the LBH variations on a H-passivated silicon sample and a tungsten tip. Therefore, LBH variations can destabilize the STM feedback loop that operates based on a conventional fixed-gain PI controller.

4.4.3 Proposed LBH Measurement Method

Our approach for measuring the LBH is similar to the conventional method in the sense that it is based on modulating the tip-sample distance at a high frequency and tracking the corresponding amplitude at output by a lock-in amplifier. However, unlike the conventional approach, we assume that the modulated amplitude of δ may change due to the controller response. This is a sensible assumption because, even if the modulating frequency is out of the bandwidth of the closed-loop system, the controller will always pass a portion of $\ln i$ at the frequency $\mathit{\Omega}$, and as a result, the modulation amplitude of δ will be affected by LBH.

The control block diagram shown in Figure 4.2 motivates us to measure the DC gain of the plant $G(s)$ and relate it to the LBH variations. To do this, we inject a single-tone dither signal with frequency $\mathit{\Omega}$ at an arbitrary point in the feedback loop, e.g. current setpoint, and track the amplitude of Ω-components at the input and output of $G(s)$. If the amplitude of setpoint dither is r_0, the corresponding amplitudes at the input and output of $G(s)$ will be given by:

$$Y(j\mathit{\Omega}) = K(j\mathit{\Omega})G(j\mathit{\Omega})\left(1 + K(j\mathit{\Omega})G(j\mathit{\Omega})\right)^{-1} r_0 \tag{4.12}$$

$$W(j\mathit{\Omega}) = K(j\mathit{\Omega})\left(1 + K(j\mathit{\Omega})G(j\mathit{\Omega})\right)^{-1} r_0 \tag{4.13}$$

where $W(s)$ and $Y(s)$ are input and output signals for $G(s)$ in Laplace space, respectively, as shown in Figure 4.3, and $j = \sqrt{-1}$. Calculating the magnitude of complex variables and dividing (4.12) by (4.13) gives:

$$\frac{\| Y(j\mathit{\Omega}) \|}{\| W(j\mathit{\Omega}) \|} = \| G(j\mathit{\Omega}) \| = \widetilde{C} \tag{4.14}$$

which means that the fraction in the left of (4.14) is independent of the controller dynamics and feedback effects and solely dependent on the plant dynamics at the frequency of $\mathit{\Omega}$. On the other hand, we can separate the effect of the plant DC gain and the rest of its dynamics by re-writing the right hand as:

$$\widetilde{C} = \sqrt{\varphi} k_{HV} \gamma \, \| G_0(j\mathit{\Omega}) \| \tag{4.15}$$

where γ is the constant piezo-material sensitivity and $G_0(s)$ is a dynamic system with unit DC gain representing the remaining dynamic components of $G(s)$. As discussed before (Tajaddodianfar et al., 2017),$\| G_0(j\Omega) \|$ is reasonably assumed to be constant during the STM operation. Thus, any variation in $\widetilde{C}$ is due to the changes in the square root of LBH. We calculate $RY = \| Y(j\Omega) \|$ and $RW = \| W(j\Omega) \|$ using any type of lock-in amplifier and divide them to obtain $\widetilde{C}$ according to (4.14) at each time t. The estimated parameter $\widetilde{C}$ reflects the variations of the LBH and is proportional to the feedback loop gain. Therefore, $\widetilde{C}$ can also be used to continuously update the gains of a PI controller in reaction to variations in plant DC gain in order to maintain the LBH at a pre-determined level. Here, we use a Lyapunov filter to track the amplitude of dither signal. This is an alternative implementation of lock-in amplifier that was described in detail in (Ioannou and Sun, 1996; Tajaddodianfar et al., 2017). In this scheme, the signal is first passed through a second order IIR band-path filter with a passband centered at Ω and then a first order Lyapunov filter tracks the amplitude of the resulting signal. It can be shown that the port at which the exogenous signal is added does not affect the equation (4.14). This means that there is no difference if we use either of the identification signals $r(j\Omega)$ or $u(j\Omega)$ shown in Figure 3.1b. However, since W is a small signal, we found it more effective to add the identification signal to setpoint in order to obtain a better signal at W. The only thing that should be considered is to maintain a good signal-to-noise ratio (SNR) at frequency Ω in both outputs of the closed loop. To achieve this, we leave the amplitude of the injected signal as a tunable parameter which can be adjusted by the user to keep a good SNR. However, amplitude of $r(s)$ should not be so large to trigger nonlinear oscillations or lead to tip-sample crash.

Based on the structure shown in Figure 4.3, the signal W is used to generate a topography image of the surface, while $\widetilde{C}$ can be used to produce an LBH image which shows local barrier height variations over the sample. Considering the fact that the LBH is affected both by the tip and surface properties, we expect to observe certain features in the LBH image which reflect local changes in electronic properties of the sample. This will be discussed in further detail in the section 4.6.

4.5 Self-tuning PI controller

Variation of the open-loop DC gain or LBH affects the closed-loop stability and performance in the same way that the integrator parameter k_i given by (3.17) does. Since we have an estimation $\widetilde{C}$ proportional to the instantaneous open-loop DC gain, it is possible to adjust the controller gains at each time t such that the overall loop gain remains constant despite variations stemming from the LBH. To do this, we first define a constant desired value $\widetilde{C}_d$ at which we aim to keep $\widetilde{C}$. Then, we multiply the controller command by $\widetilde{C}_d/\widetilde{C}$ which is equivalent to updating the controller gains at each time step as:

$$(k_i)_{new} = k_i \frac{\widetilde{C}_d}{\widetilde{C}} \tag{4.16}$$

Considering the controller structure given by (3.17), equation (4.16) implies that both integral and proportional gains are multiplied by the factor $\widetilde{C}_d/\widetilde{C}$. The desired parameter $\widetilde{C}_d$ is also left as a user-defined parameter and it is recommended to be selected in the mid-range of observed $\widetilde{C}$ variations. Also, we pass $\widetilde{C}$ through a saturation block to ensure that possible undesired sparks in $\widetilde{C}$ do not result in inappropriately large or small controller gains. Figure 4.3 displays the overall Z-axis control system structure with the self-tuning PI control.

4.6 Experimental Observations and Results

In this section, first we present the experimental results confirming the fact that the LBH is a varying parameter that depends on local effects. Operation of STM highly depends on the

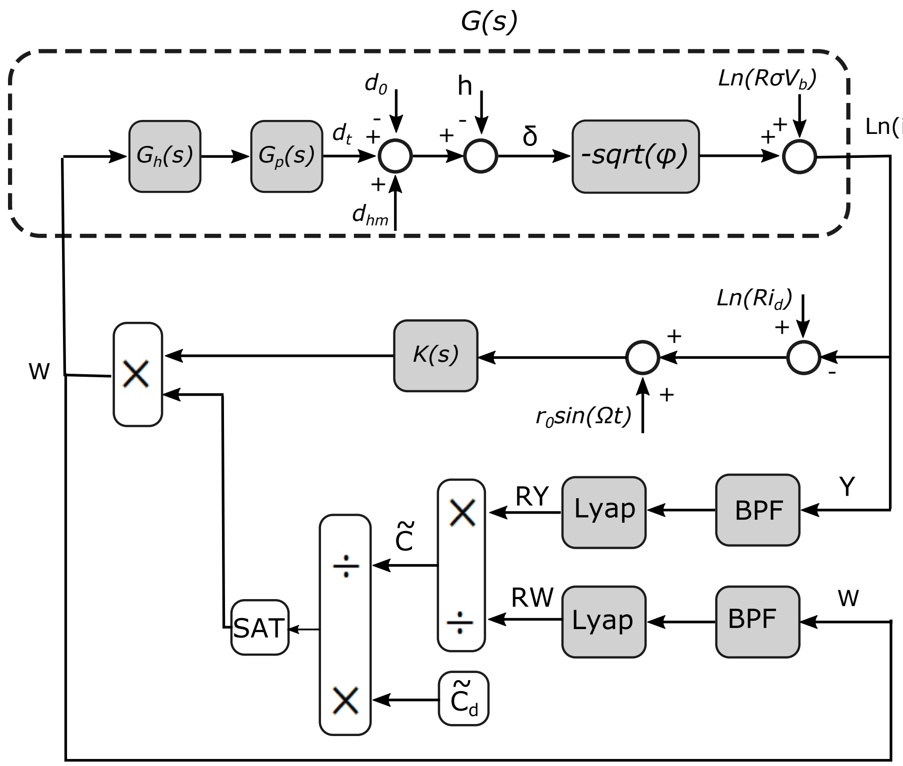

Figure 4.3. Z-axis control system block diagram with self-tuning PI controller. The blocks shown by BPF are band-pass filters through which the measured signals are passed prior to being fed into the Lyapunov Filters. RY and RW are the amplitude of the Ω-component in logarithm of tunneling current (Y) and the controller command (W), respectively. $\widetilde{C}$ is given by (4.14) and is proportional to the LBH. The block SAT is a saturation block which limits the modifying factor for safety reasons. A lock-in amplifier block LIA can replace the blocks BPF and Lyap.

functionality of tip and sample. At least two major tip conditions are distinguishable in STM: i) Unstable tip which presents frequent tip changes and cannot sustain its configuration for a satisfactory image quality, and ii) Stable tip which does not change frequently and provides sustained image quality. Having an unstable tip, the measured LBH is highly affected by tip changes, while with a stable tip the measured LBH is mainly influenced by the surface electronic properties of the sample. In the following, we first present our observations of the LBH variations in the presence of an unstable tip, and then we present the results of self-tuning PI control while having a good stable tip.

4.6.1 LBH Measurements

We used the architecture shown in Figure 4.3 for estimating the LBH. Figures 4.4 to 4.6 display our experimental observations confirming the fact that $\widetilde{C}$ is a varying parameter depending on local effects. Figure 4.4 displays parameter $\widetilde{C}$ along with parameters RY and RW described in Figure 4.3 measured by filter gain of $\gamma = 100$ while the STM was idle with all the user defined parameters fixed. At time $t \simeq 3s$, the controller gain k_i was increased and then it was decreased back to the previous value at $t \simeq 22s$. Figure 4.4 suggests that despite RY and RW, the parameter $\widetilde{C}$ is not mainly affected by the controller gains and this agrees with equation (4.14).

Figure 4.5 presents parameter $\widetilde{C}$ measured using $\gamma = 30$ for the filter gain, while the STM tip was unstable and changing frequently. All other control system parameters were fixed while collecting data shown in Figure 4.5 and the STM was not scanning. Although tiny relative tip-sample motion is always expected due to drift and piezo creep, but tip change is considered to be the major cause of the precipitate changes in $\widetilde{C}$ which can be attributed to the LBH changes as discussed in previous sections. Figure 4.6 provides yet another clue that $\widetilde{C}$ is highly local. In this experiment the STM was idle while $\widetilde{C}$ was being measured by $\gamma = 30$. At time $t \simeq 5s$, the STM tip was moved on the XY plane from its original location A to a new point B located several nano-meters away. The measured parameter $\widetilde{C}$ was nearly doubled by moving from point A to point B. We continued measuring $\widetilde{C}$ in the new location and moved it back to the previous point A at time $t \simeq 26s$. As shown in Figure 4.6, $\widetilde{C}$ drops back to the values it had at point A. The substantial change in $\widetilde{C}$ triggered by moving from one location on the sample to another suggests that the electronic/chemical properties of the atoms tunneled through on the sample at point A are different from those of atoms at point B, resulting in different LBH values at the two points. This observation confirms that while scanning and sweeping over the sample, the LBH can experience substantially different values depending on the chemical composition and structure of the sample surface, and this is equivalent to the variation of control loop gain while scanning.

Moreover, the given results present slower variation of $\widetilde{C}$ at some time intervals e.g. at $15s < t < 20s$ in Figure 4.6 or at $22s < t$ in Figure 4.5. These observations suggest that not all the variations in $\widetilde{C}$ are precipitate. In fact, $\widetilde{C}$ may experience fast or slow changes in its value depending on the complicated physics governing it. The presented observations confirm that the plant DC gain which is proportional to $\widetilde{C}$ can take significantly different values while STM is operating. These variations originate from tip-changes, atomic structure of the sample, or any other possible physical source, and can be slow or fast. However, these observations suggest the need for continuous tuning of controller gains to prevent instabilities stemming from such DC gain variations.

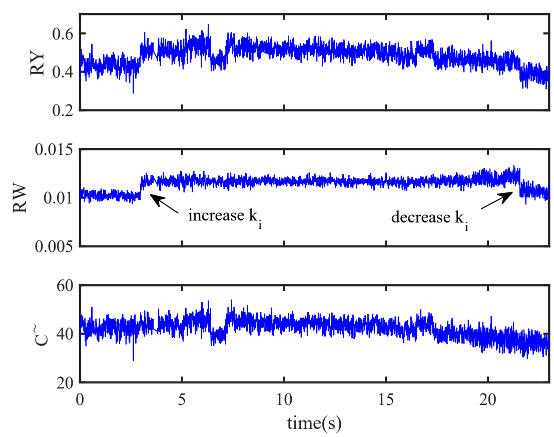

Figure 4.4. RY, RW and $\widetilde{C}$ as described in Figure 4.3 measured using $\gamma = 100$ as the filter gain. Controller gain k_i is increased at time $t \simeq 3s$ and is turned back to its previous value at time $t \simeq 22s$. Controller gain change does not affect $\widetilde{C}$ as expected by equation (4.14).

The LBH is also expected to be dependent on the bias voltage applied to the tip and sample. Figure 4.7 displays the measured variable RY, RW and $\widetilde{C}$ while the STM is idle and the bias voltage is changed from -2.5 V to +8 V and reverse. A significant variation in the LBH is clear as shown in this figure.

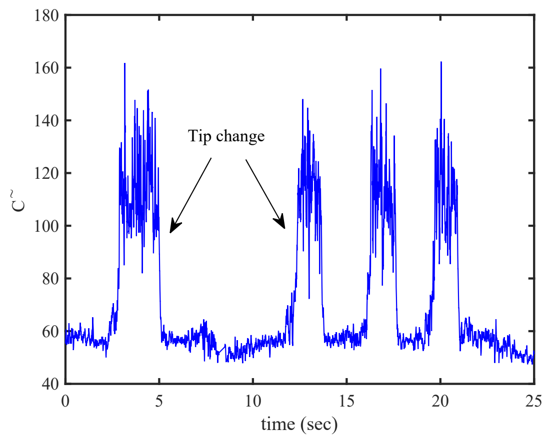

Figure 4.5. $\widetilde{C}$ measured using $\gamma = 30$ as the filter gain while the STM is idle. STM tip is unstable and precipitate variations occur due to tip changes.

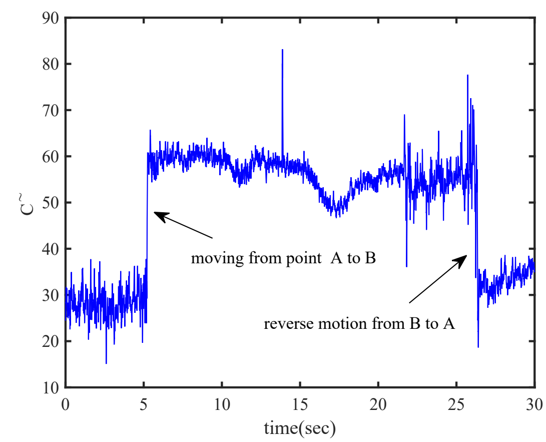

Figure 4.6. $\widetilde{C}$ measured using $\gamma = 30$ as the filter gain. The tip is moved from some point A to another point B in the XY plane at time $t \simeq 5s$, and is moved back to point A again at time $t \simeq 26s$. All other parameters are fixed.

4.6.2 Comparison with the Gap Modulation Method

Both the conventional LBH measurement method and the alternative method proposed here are used to generate LBH images. These images are obtained with and without the PI controller tuning scheme described in section 4.5. In the present section we compare the obtained results to appreciate the difference between the two methods.

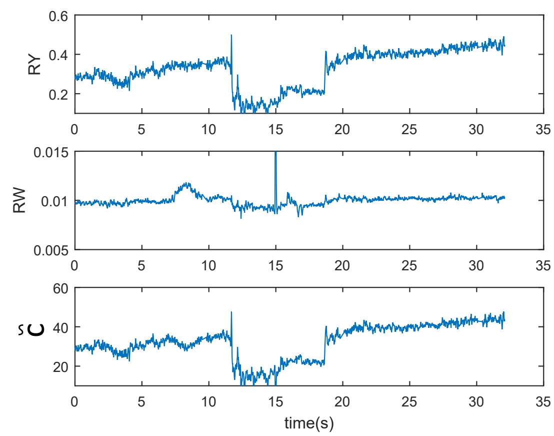

Figure 4.7. RY, RW and $\widetilde{C}$ as described in Figure 4.3 measured using $\gamma = 100$ as the filter gain. The STM is idle and the bias voltage is changed from -2.5 V at time $t \simeq 12s$ to +8 V and it is changed back to -2.5 V at $t \simeq 18s$.

Figure 4.8 displays an STM topography image as well as LBH images obtained using the proposed and conventional methods simultaneously. Experiments were conducted with fixed PI gains. The topography image shows the relative height of features with respect to the mean value. In order to depict the LBH image, we estimated parameter $\widetilde{C}$ based on equation (4.15) and divided it further by the system constants k_{HV} and γ to set the units to $1/nm$, as shown in Figure 4.8 (middle). In the conventional method, only $\ln i$ is used to produce the image. The image displayed in the bottom of Figure 4.8 was plotted using the signal RY shown in Figure 4.3.

A number of surface features including dimer rows, step-edge, missing Si dimers and dangling bonds are visible in the topography image (Figure 4.8 top). For some features the contrast is purely physical. The top of the step edge appears brighter than the base, while the missing dimer defects appear dark. Dangling bonds (DB) result from missing hydrogen atoms (Ballard et al., 2013; Randall et al., 2009), and appear as bright features. In this case, the contrast is electronic. The dangling bond states are much closer to the Fermi level than the H-terminated dimers, and as a result, tunneling is easier on the dangling bonds; hence, the tunneling current tends to increase over them. However, since the controller keeps the current constant, it moves the tip away from the surface over a dangling bond and as a result dangling bonds appear as bright spots in the topography image. Equivalently, LBH is lower on a dangling bond since states are closer to the Fermi level. This results in a higher DC gain of $G(s)$ in Figure 4.2 given the negative sign in the exponential component in equation (4.10).

It is well known that the LBH image is always correlated to the topography. One reason is that the control system moves the tip perpendicular to the average surface while the actual current is not always in this direction (Binnig and Rohrer, 2000). Although the LBH changes while crossing the dimer rows, a large correlation to topography is considered an undesired effect in LBH images (Binnig and Rohrer, 2000). The profile B sketched on Figure 4.8 (middle) shows that the topography is within 21.6% of the mean value of the recorded LBH, while the profile C shows this value as high as 60.4%, suggesting that the LBH image that our method produces presents less correlation to the topography. In addition, it is observed that the dangling bonds that are real LBH features appear with a better contrast in the middle image in Figure 4.8 which suggests that the proposed method is capable of capturing the surface electronic properties with a better contrast.

Our analysis in section 4.4.1 shows that the conventional method also depends on the feedback system parameters, and we expect to observe more LBH image distortion while the controller gains are adjusted. This is shown in Figure 4.9 which is the same as Figure 4.8 except that the self-tuning control scheme proposed in section 3.1.1 is operating. Figure 4.9 (middle) shows that the LBH features are still distinguishable with good contrast while the self-tuning controller is operating. In contrast, in the $\ln(i)$ image which represents the conventional LBH measurement method, the LBH features appear as high as topographic features. This failure is due to the dependency of the conventional method on the feedback parameters, as discussed in section 4.4.1

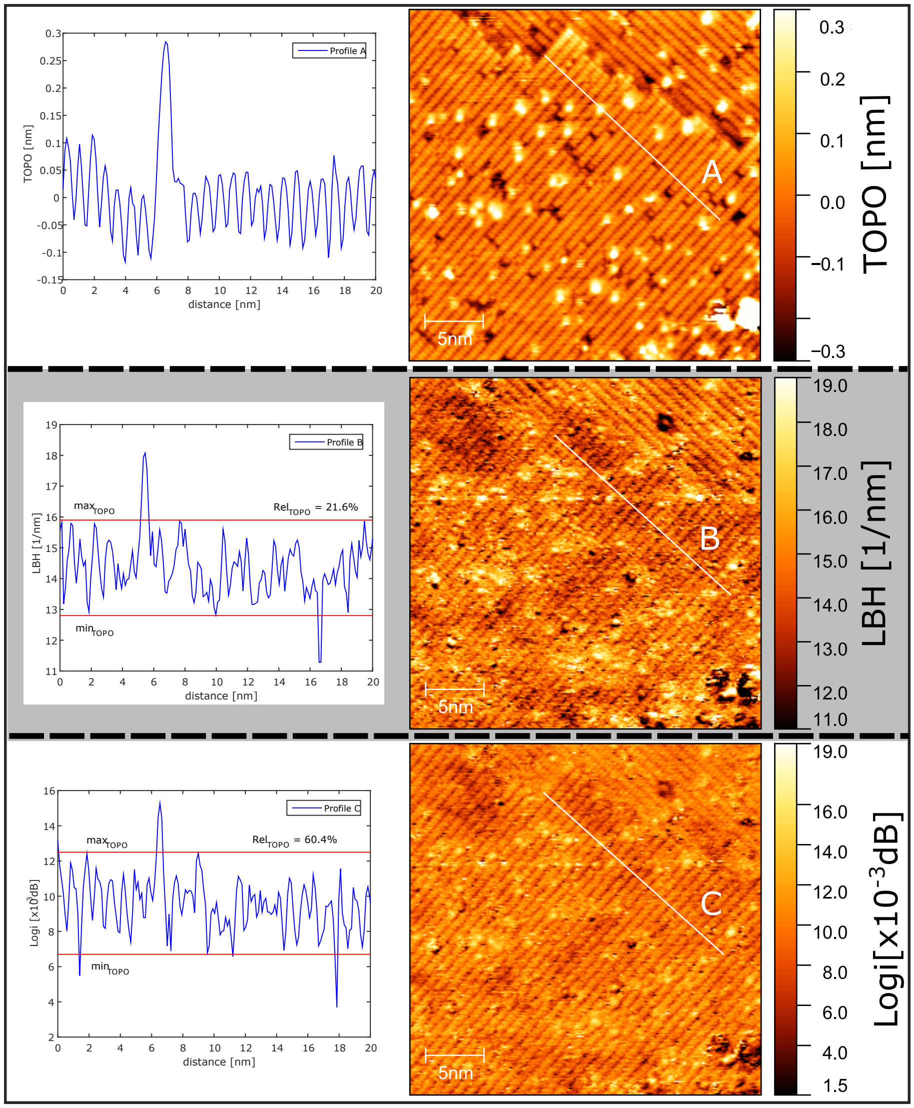

Figure 4.8. STM topography image (top) and the LBH images using the proposed (middle) and the conventional (bottom) methods. All three images were captured simultaneously while the self-tuning algorithm was off. The plots left to each image show the corresponding profile and suggest that a relative 21.6% of the mean value is due to the topography effects in the proposed method, while this relative value is as high as 60.4% in the conventional method. A better contrast of LBH features in the conventional method is apparent. Rel_{TOPO} is defined as $Rel_{TOPO} = 2\,(max_{TOPO} - min_{TOPO})\,/\,(max_{TOPO} + min_{TOPO})$.

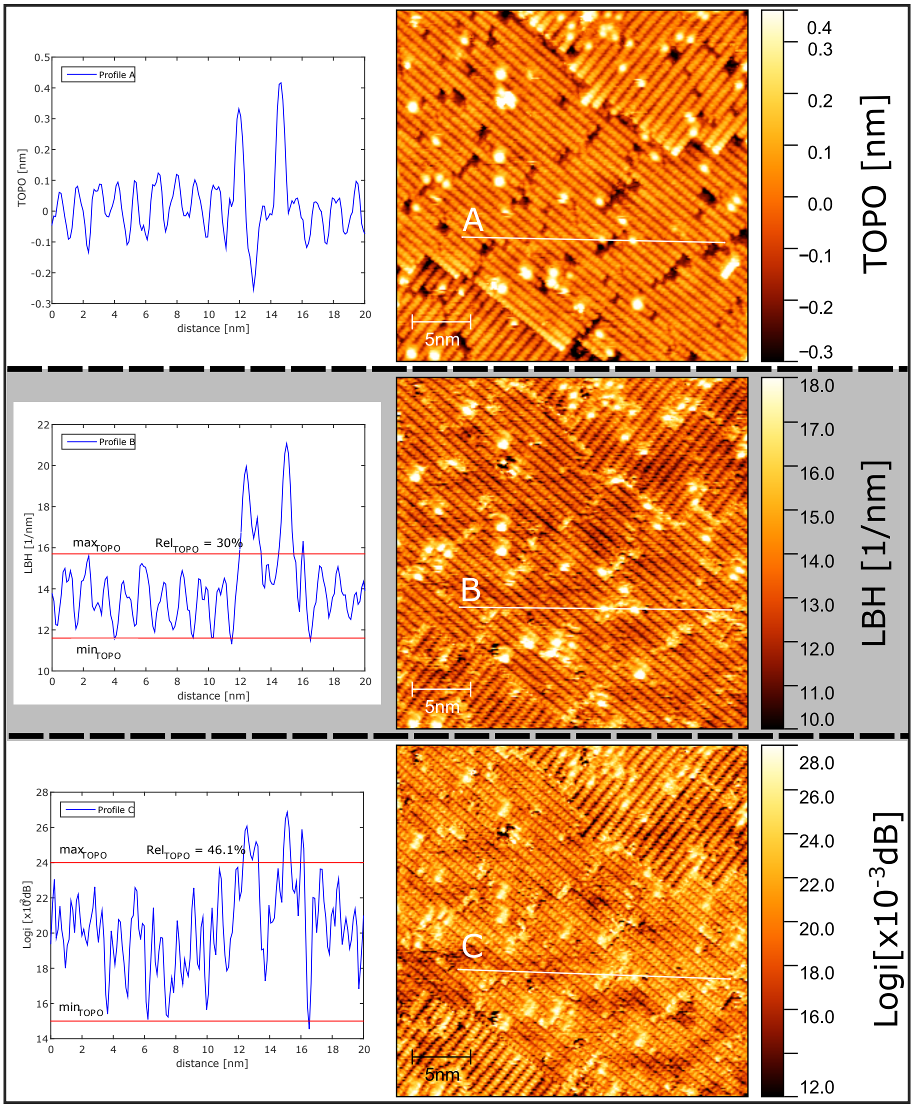

Figure 4.9. STM topography image (top) and the LBH images using the proposed (middle) and the conventional (bottom) methods. All three images were captured simultaneously while the self-tuning algorithm was active. The plots left to each image show the corresponding profile and suggest that a relative 30.0% of the mean value is due to the topography effects in the proposed method, while this relative value is as high as 46.1% in the conventional method. It is clear that in the bottom image the real LBH features appear as high as the topography features, but the LBH image obtained using our method (middle) is not affected by controller tuning and the LBH features are still distinguishable with good contrast.

4.6.3 Self-tuning PI controller

We conducted several experiments to investigate the stabilizing effect of the PI tuning algorithm proposed in section 4.5. LBH is measured at $\Omega = 1kHz$ and $\zeta = 1000$. In order to show the stabilizing effect of the tuning algorithm, PI gains are intentionally set to a high value to bring the feedback system close to the stability margin. Due to contamination or previous tip-sample contact, an area of low LBH (high $\widetilde{C}$) value exists on the hydrogen passivated silicon sample as shown in Figure 4.10. First we deactivated the tuning algorithm and scanned with high gain. When passing over the low-LBH area, the feedback system undergoes ringing. The instability is apparent in current error image (profile F in Figure 4.10). Note that this happens only over the atoms with low LBH, while over the neighboring atoms with large topography and normal LBH, the feedback system is still stable. Table 4.1 shows the main parameters used for the imaging, LBH estimation, and controller tuning throughout this section.

Table 4.1. Major parameter values used throughout the experiments.

Parameter	Value
Feedback bandwidth	˜200 Hz
LBH estimation bandwidth	400 Hz
rastering speed	60 nm/s
dither frequency (Ω)	4 kHz
current setpoint	0.2 nA
bias voltage	2.5 V
signal-to-noise ratio at Ω	10 dB

Immediately after the first test, we activated the tuning algorithm and re-scanned the surface while all other parameters including the initial PI gains were preserved. As shown in the middle row of Figure 4.10, the feedback loop remains stable despite large variations in LBH. Comparison of profile F and profile E in Figure 4.10 shows that with the PI tuning algorithm the current is better kept constant. Profile D in Figure 4.10 shows that $\widetilde{C}$ in the contaminated area is near 50% larger than other locations on the surface. This explains the feedback instability in that area which appears as large current changes and visible ringings in topography. When PI tuning is active, PI gains are lowered over this area and feedback system remains stable. When the PI tuning is inactive and feedback system is ringing, LBH estimation results shown by profile C in Figure 4.10 are not reliable. Comparison of the topography images and profiles A with B in Figure 4.10 confirms that feedback instability leads to artifacts in the obtained STM image, while with the PI tuning these artifacts are removed.

We repeated the same experiment on a different sample and with another tip. Obtained results are shown in Figure 4.11. In this experiment we had a clean sample with several dangling bonds representing missing hydrogen atoms that appear as bright dots in the topography images. Over the dangling bonds the LBH is lower and the measured $\widetilde{C}$ is higher as shown by profiles C and D in Figure 4.11. We used a set of PI gains that put the system close to the stability margin when PI tuning is inactive. While passing the dangling bonds, the feedback system experiences instability as shown by profile E in Figure 4.11. After the PI tuning is activated, the system operates reliably and produces clean images without artifacts while the PI gains are still high.

In order to investigate the efficiency of the self-tuning algorithm proposed in section 4.5, we assigned a set of high PI gains which put the feedback system close to the stability margin. We used the Zyvex Labs' scanner for these tests, and first turned the tuning algorithm off while scanning a litho-patterned sample with a slow rastering speed of $60nm/s$. In the patterned area the LBH is higher than the rest of the sample. As a result, we expect the closed-loop system to experience ringing while passing over the litho-patterned area noting that the loop gain is already high.

Figure 4.12 displays the STM topography, current error, and LBH images in top, middle and bottom rows respectively for the two cases of PI tuning Off (middle column) and On (right column). Prior to these tests, we to produce an HD lithography on the sample and drew several line patters which are visible in the images plotted in Figure 4.12. Hydrogen atoms have been removed from the patterned area. As a result, the LBH is higher on the patterns compared to the rest of the sample where electrons tunnel through hydrogen. Recalling that the LBH is directly affecting the closed-loop gain, we expect to observe instability over the patterns given large initial PI gains. We first fixed the PI gains and scanned the sample using the parameters given in Table 4.1. Then, we activated the tuning algorithm and scanned the same area again. All other parameters and conditions are the same between the two successive scans.

The middle row of Figure 4.12 compares the current error signal between the two cases. When the tuning is Off, the feedback system undergoes large oscillations while passing over the lithography patterns. As a result, the current error experiences values as low as $0.6nA$. Note that in the areas other than the patterns, the system is stable and current error is kept near zero. This supports our claim that the control system performance can be affected significantly by the local properties of the sample and tip. On the other hand, the current error image in the right column of Figure 4.12 shows that the feedback stability is preserved both over the lithography patterns and hydrogen passivated area, using the self-tuning algorithm.

The top row of Figure 4.12 compares the topography images for the two cases with and without self-tuning controller. Ringing due to the closed-loop instability is apparent around the patterns when the tuning is Off. In the bottom row of Figure 4.12 the LBH images are compared. Note that when the feedback system undergoes instability while the tuning is off, the LBH estimation algorithm fails. Therefore, the estimated LBH values shown in profile E are not reliable in this case. However, the system stays stable when using the PI tuning method. The estimated LBH values for this case displayed in profile F in Figure 4.12 shows a near 30% increase in the measured value which was enough to destabilize the feedback system in the absence of the tuning algorithm.

We also conducted further tests to verify performance of the proposed self-tuning controller on the commercial Omicron scanner. We pursued the same test strategy articulated above by setting high PI gains and repeating the STM scan successively with and without

PI tuning scheme. Results are shown in Figure 4.13. A prior lithography pattern provides an area on which the LBH value is locally different from the rest. Passing over the pattern while the tuning algorithm is off, the feedback system undergoes ringing as shown by profile D in Figure 4.13 given that the PI gains are already high. However, repeating the same scan immediately with the self-tuning algorithm in operation, the control system preserves the stability as proved by the current error image and profile C in Figure 4.13. Getting the same behavior on a commercial STM scanner assures us that the observed performance of the self-tuning PI controller is not due to the dynamics of the scanner and can be generalized to the whole family of STMs.

4.6.4 Effect on tip life-cycle

The experimental results reported in section 4.6.3 prove the efficiency of the self-tuning PI controller in avoiding the instabilities arising from LBH variations. However, to capture those results we have put the system close to its instability margin by using high PI gains. Although such high gains are not normally used in STM operation, they facilitate proving the claim that the LBH can result in closed-loop instability. Moreover, high PI gains help to capture the LBH stability effects in a single experiment. In normal working conditions, the LBH stability effects may appear gradually and influence the tip life-cycle.

We have conducted further experiments to investigate the effect of self-tuning PI controller in the STM tip durability. To this aim, we operated the STM in its normal imaging conditions, i.e. the PI gains and the scanning speed are set to their normal imaging values. Then, we capture a large number of STM images with or without the tuning algorithm and compare them to investigate the possible effect of tuning on the tip life-cycle.

Figure 4.14 displays a range of images captured using the Omicron scanner while the PI tuning was active. PI gains are set to their normal imaging values and the scanning speed is set to $150nm/s$. Each image take 5 minutes to complete and overall 64 images were taken, half of them are shown. Numbers next to the left column shows the time of taking the image in left column wit respect to the first image, and each column is taken 10 minutes after the preceding column. The tip changes several time during imaging. Every tip change causes LBH variations, however, the closed-loop system tolerates those variations and the tip survives for several hours of consecutive imaging.

After taking 64 images with active PI tuning, we immediately turned the tuning off and started another set of consecutive imaging. All parameters are kept at their previous values and half of the captured images are shown in Figure 4.15 that shows an interesting trend in the absence of tuning algorithm. Figure 4.15 shows that in the beginning the tip is almost sharp and the STM gives a good image. In the first few images several tip changes have occurred. The left image of the second row displays formation of two horizontal patterns on the surface that is very similar to HDL patterns. These patterns are formed near the spots over which tip changes have already occurred. In the next images we observe that the depassivated patterns grow gradually as more tip changes occur in those spots. This trend continues until the tip permanently changes and the STM loses its imaging capability.

The images shown in Figure 4.15 suggest that closed-loop instabilities can originate from tip changes and damage both the tip and the surface. Tip changes are visible in both Figure 4.14 and 4.15. However, when the PI tuning is inactive in Figure 4.15, the LBH variation originated from a precipitate tip change can cause momentarily closed-loop instability that brings the tip so close to the sample that several Hydrogen atoms are depassivated Over the pattern areas, LBH is different and therefore next times that the STM scans these spots it will be more prone to tip change and instability. This can be the reason for the observed growth of the patterned area in Figure 4.15. On the other hand, Figure 4.14 shows that tip changes that occur while PI gains are being tuned do not result in surface damage and the tip can survive those disturbances.

4.7 Concluding Remarks

We analyzed the control system of a Scanning Tunneling Microscope (STM). Frequency-domain closed-loop system identification tests were performed to obtain open-loop models of the STM. Our analysis show that the DC gain of the obtained open-loop plant is proportional to the Work Function or the Local Barrier Height (LBH) which is a quantum mechanical parameter of the tunneling current. The LBH is known to be a variable parameter in STM which depends on many local effects. We have shown that the LBH variation can dramatically change the loop gain in the presence of a controller with fixed parameters and this can easily result in the closed-loop instability. We proposed an algorithm for online LBH estimation which includes modulation of the current setpoint by a known fixed frequency Ω and tracking the amplitude of the corresponding component in the outputs of the closed-loop system using Lyapunov filters. The tracking bandwidth of the filter is left as a user-defined parameter for noise-bandwidth compromise. The obtained estimation is used for self-tuning of the gains of a proportional-integral PI controller. Also the estimated LBH is used for generating LBH images which map electronic properties of the sample.

Experimental results confirm that the estimated LBH is a parameter showing both slow and fast variations. The LBH is observed to precipitately change in certain conditions with unstable tip and also over specific locations on the sample. With the bandwidth of the LBH estimator selected close to that of the feedback system, the estimator tracks variations in the LBH while scanning over the sample, and this is used for self-tuning of the PI gains. The proposed method is observed to be effective in enhancing the closed-loop stability. Also, this tuning method is expected to facilitate safe increase of PI gains that gives higher closed-loop bandwidth and enables high-speed scanning.

We also conducted further experimental analysis to investigate the effect of the proposed PI tuning algorithm on the life cycle and tip durability of the STM tip. Obtained results show that the proposed control method can help to extend the tip life by preventing the tip-sample crash. This can be of extensive interest in the STM community that suffers from frequent tip crashes. The obtained results confirm the effectiveness of the proposed method. Efforts are underway to confirm increased life time of STM tips with different samples.

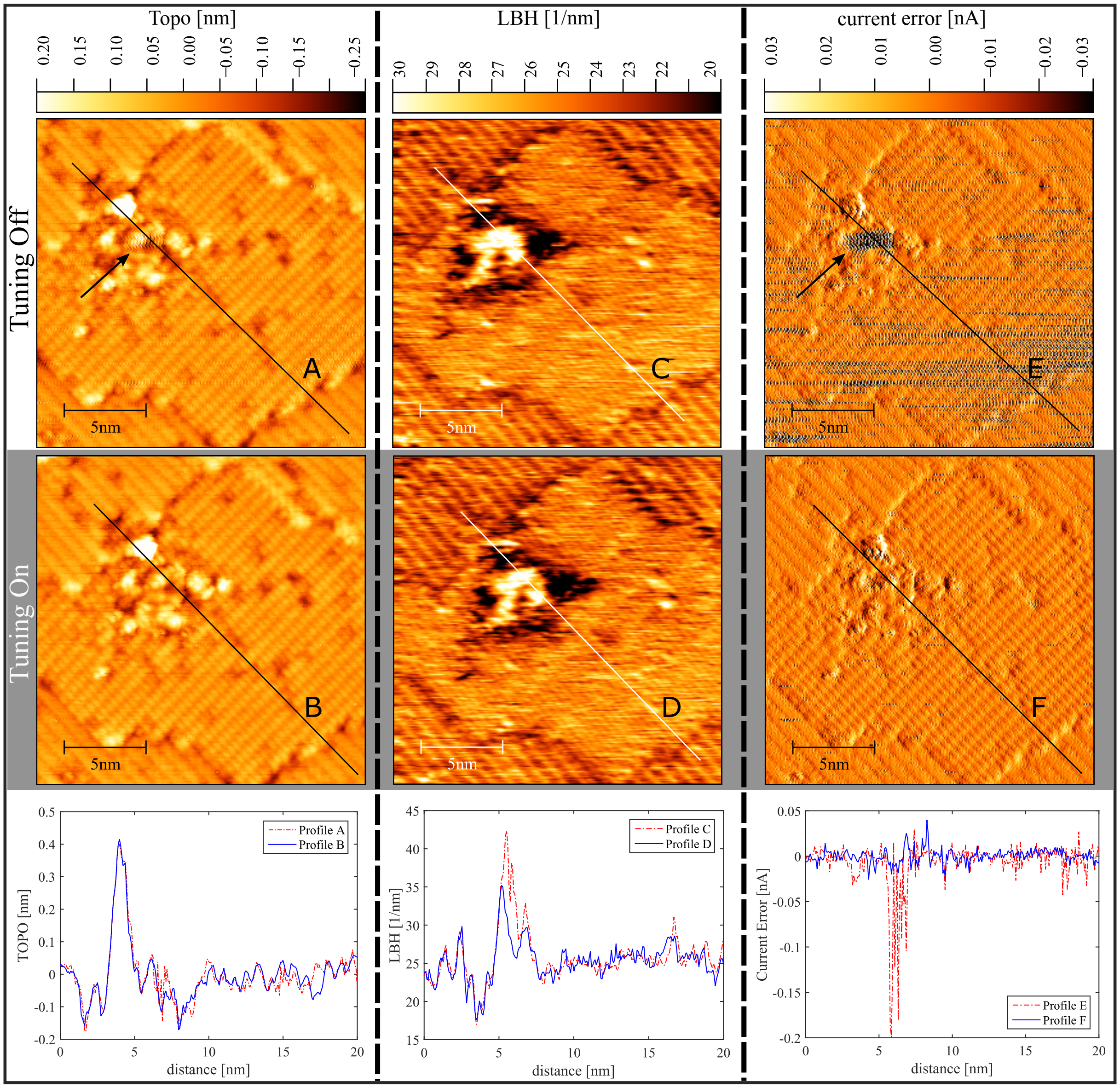

Figure 4.10. PI tuning effect on STM performance. Topography (left column), $\widetilde{C}$ representing the LBH (middle column), and current error (right column) images for the two cases without PI tuning (top row) and with PI tuning (middle row). PI gains are high and the system is close to the stability margin. Surface atomic and electronic structure is different on part of the sample due to contamination or previous tip touch. While passing over the low-LBH (high $\widetilde{C}$) area, the closed-loop system experiences ringing when the PI tuning is inactive. Immediately after the first test, PI tuning is activated and the surface is re-scanned. The closed-loop system does not experience ringing with active PI tuning. Ringing appears as artifact in topography image, e.g. area near profiles A and E pointed to by arrows.

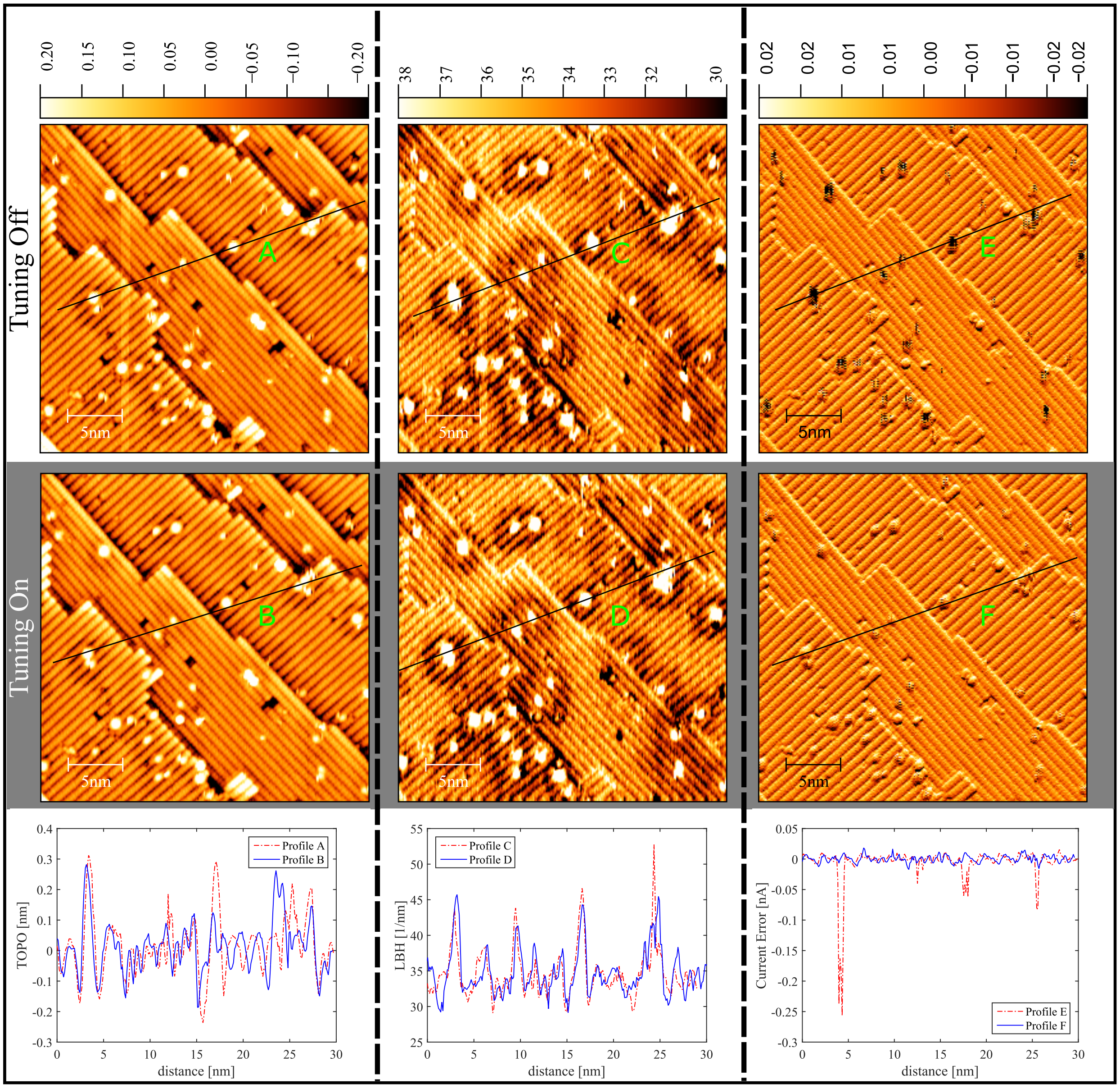

Figure 4.11. PI tuning effect on hydrogen passivated silicon sample. The surface is clean with several dangling bonds which represent missing hydrogen atoms. PI gains are high and the surface is scanned successively with PI tuning Off (top row) and On (middle row). All other parameters are the same in the two tests. Over the dangling bonds, the estimated $\widetilde{C}$ is larger, and this causes ringing when the PI tuning is Off as evidenced by profile E. When the tuning is active, the feedback system remains stable and no artifact is observed.

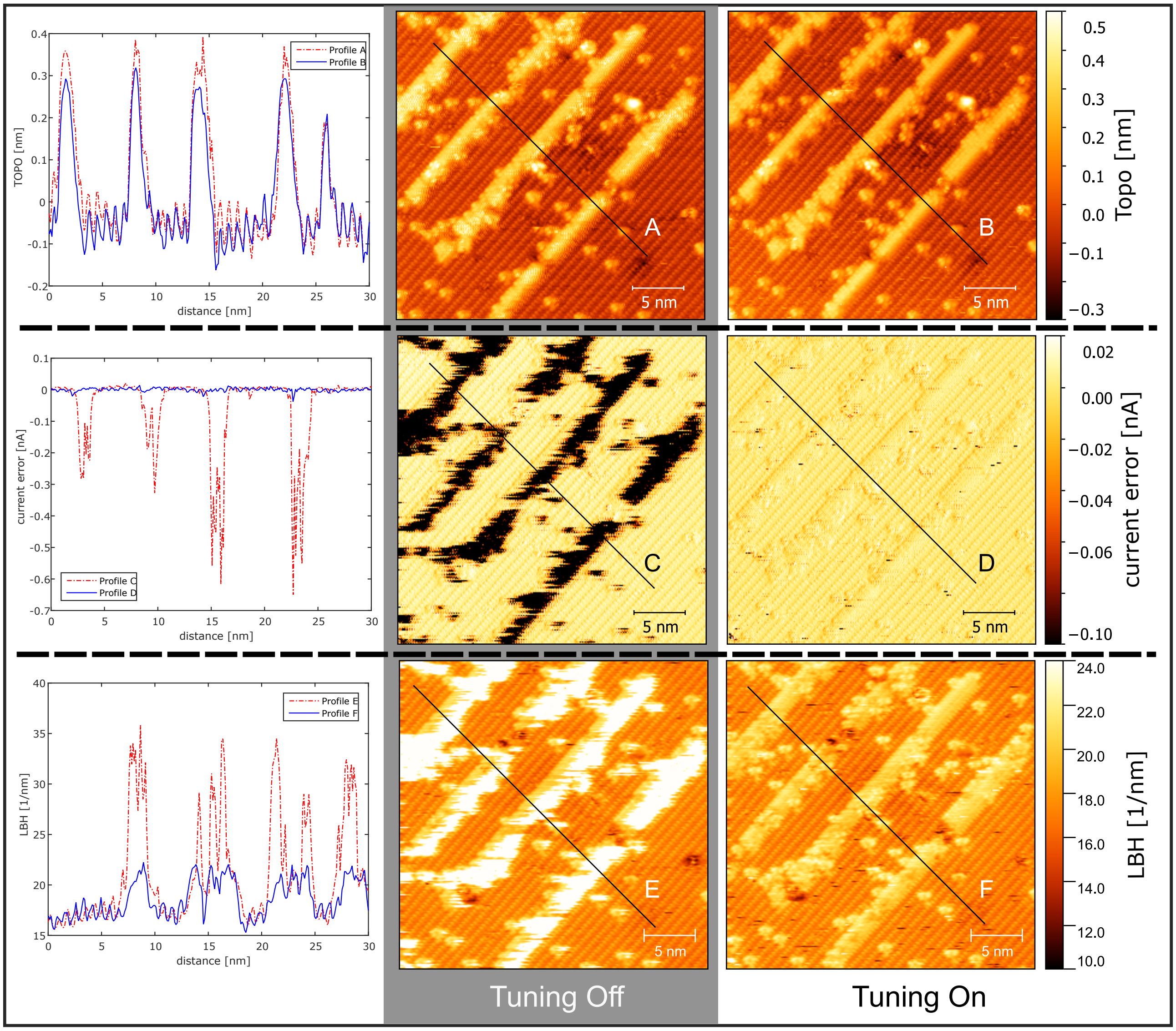

Figure 4.12. Effect of the self-tuning PI controller using Zyvex Labs' scanner. Top: topography image, middle: current error image, and bottom: LBH image, for the two cases of tuning On (right column) and off (middle column). PI gains are high and the system is close to the stability margin when the tuning is off. Large feedback error proves closed-loop ringing and instability when passing over the lithography patterns.The same system with the self-tuning controller operating stays stable. Parameters given by Table 4.1 are used during the experiments. First, three images are captured simultaneously in one scan while the tuning was off. Immediately after that, we turned the tuning On and captured the images shown in right column. All other parameters and scan conditions are the same between the two cases.

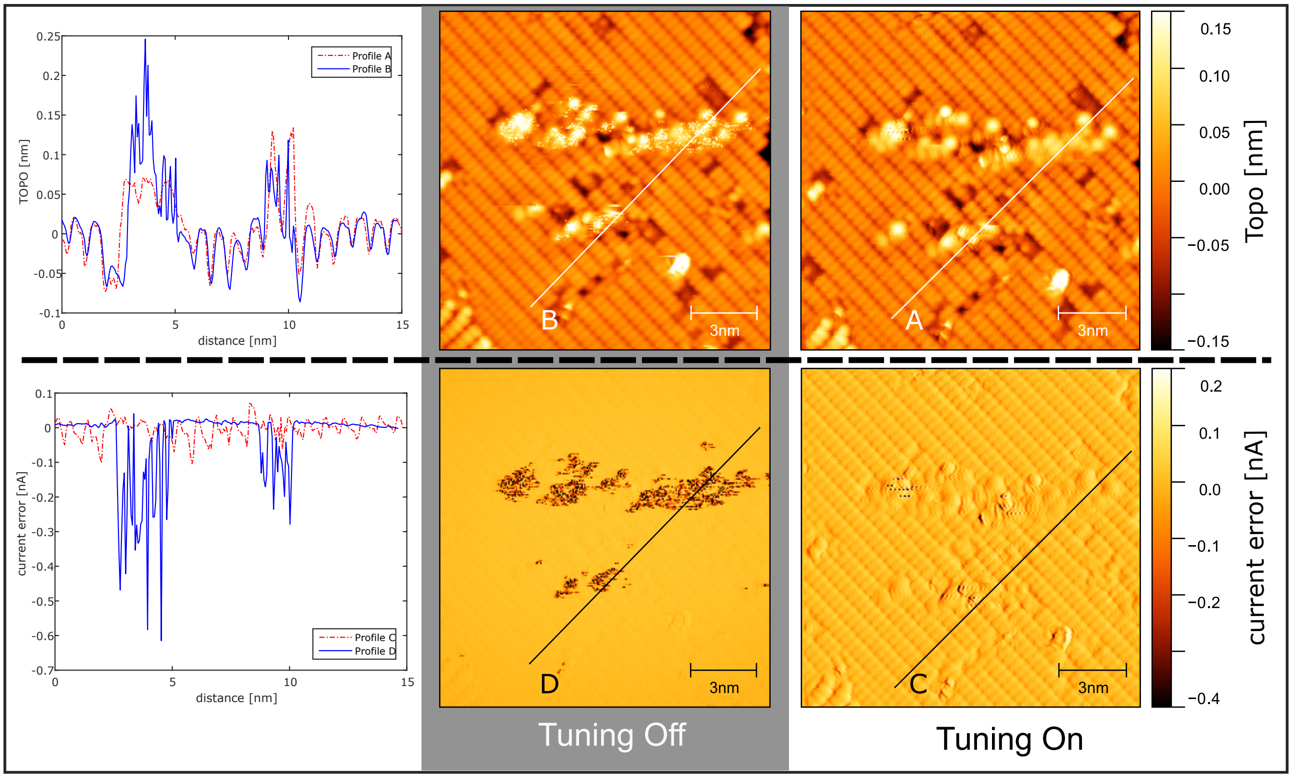

Figure 4.13. Effect of the self-tuning PI controller using the Omicron scanner. Top: topography image, and bottom: current error image, for the two cases of tuning On (right column) and off (middle column). PI gains are high and the system is close to the stability margin when the tuning is off. Large feedback error proves closed-loop ringing and instability when passing over the lithography patterns.The same system with the self-tuning controller operating stays stable. Parameters given by Table 4.1 are used during the experiments. First, the two images in the middle column are captured simultaneously while the tuning was off. Immediately after that, we turned the tuning On and captured the images shown in right column. All other parameters and scan conditions are the same between the two cases.

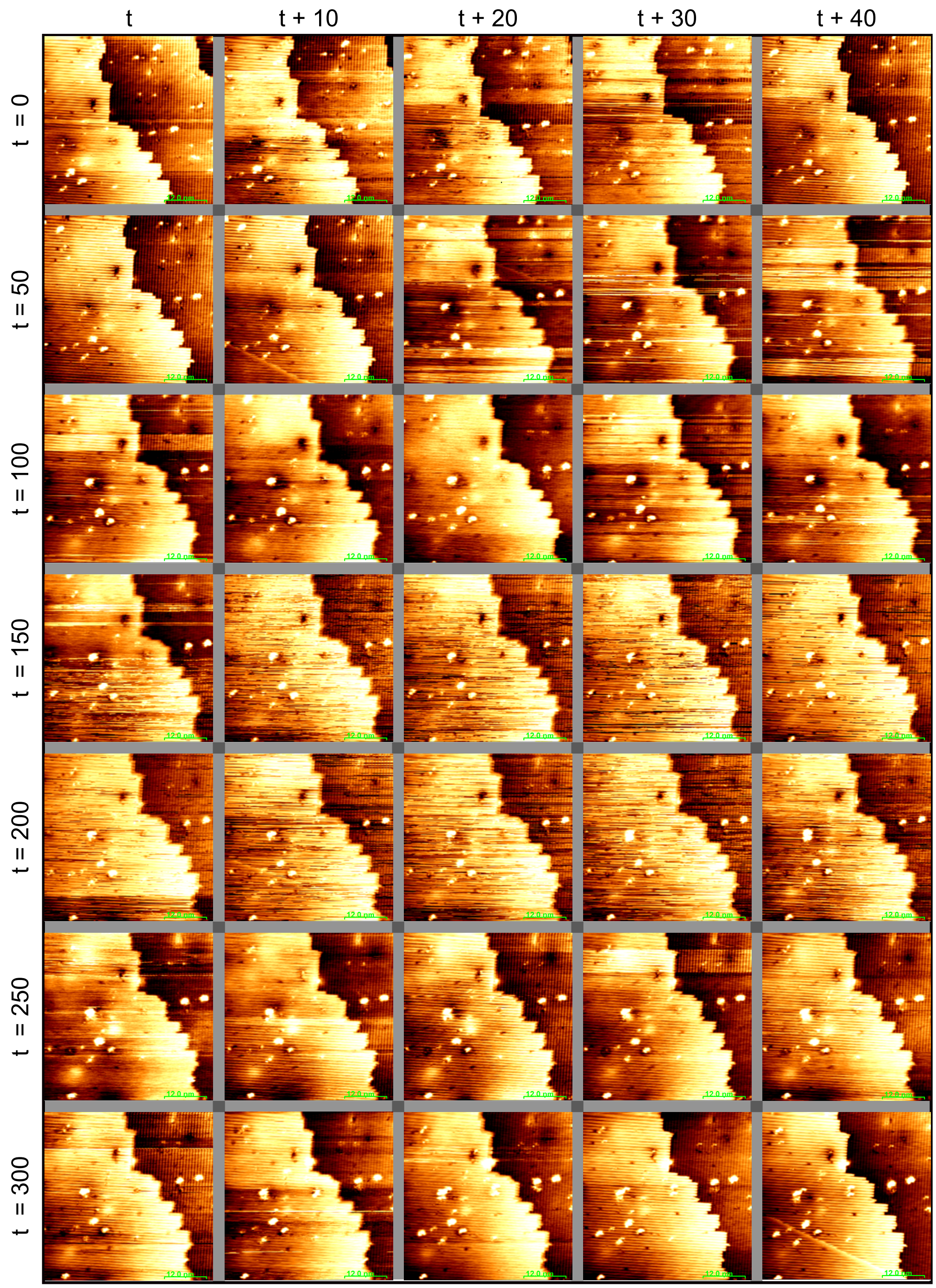

Figure 4.14. Large number of STM images taken consequently at normal PI gains with tuning algorithm active. Scanning speed is set to $150nm/s$ and the PI tuning algorithm is operating with $4kHz$ dither signal. Each image takes about $5min$ to complete and 64 images are taken with active PI tuning. Half of the captured images are shown here. Time of capturing the images with respect to the first image is also shown. The tip changes several times during the scans, however the tip survives the changes. LBH variations due to tip change do not result in permanent tip change or crash while the tuning algorithm is active.

Figure 4.15. PI tuning is Off and Large number of STM images are taken consequently immediately after the images shown in Figure 4.14. All parameters are the same as Figure 4.14. The tip changes several times during the scans, however, tip changes are followed by momentarily closed-loop instabilities. Formation of an undesired depassivation pattern is visible in the first image of the second row. The pattern on the surface grows gradually in the next images and the tip permanently crashes the surface at the end.

CHAPTER 5

APPLICATIONS IN LITHOGRAPHY

5.1 Overview

In this chapter we discuss application of STM in lithography mode. Due to severe LBH variations and harsh tunneling conditions, the STM control problem can be even more challenging in Lithography mode. We investigate the STM performance in lithography mode and compare its performance with/without the proposed self-tuning controller.

For atomically precise manufacturing and for a number of other applications, high-precision lithography is absolutely necessary. It means that the user should be able to depassivated an exact number of hydrogens in an exact desired location on the sample. This is a challenging task and an open research top in nanotechnology. We have taken several steps toward this end and have got promising results that we present in this chapter.

5.2 Hydrogen Depassivation Lithography

In Hydrogen Depassivation Lithography (HDL) the STM tip is used to transfer such high current that is enough to break the bond between hydrogen and underneath silicon atoms of a H-terminated silicon surface. This is the basis for atomically-precise manufacturing. Compared to the imaging mode, current and bias voltage are both higher in lithography mode. In imaging, current is set to the range of 0.2 to 0.4 nA with a negative bias around -2.0 to -3.0 V. But in lithography mode, bias is bigger with opposite polarity (around +4.0 V), and current is higher (around 1.5 to 2.5 nA). This large current and voltage turn the lithography mode to a harsh condition that increases the chance of tip changes. Moreover, due to chemical reactions (depassivation of hydrogen atoms) that are taken place on the surface, the current parameters, e.g. LBH, are subject to sudden changes, and this makes the control problem even more challenging. Throughout this chapter HDL is conducted under $V_b = +4V$, $i = 1.5nm$, and $v = 7.5nm/s$ as the XY travel speed of the tip, otherwise mentioned.

5.3 Effect of Self-tuning PI controller

We conducted several experiments to investigate the effect of self-tuning PI controller proposed in Chapter 4 on the performance of the STM during HDL. Figure 5.1 displays two STM images taken right after drawing two HDL patterns on the surface. Figure 5.1a shows the STM topography image after drawing line #1 on the surface while the self-tuning PI controller was active. Line #2 has been drawn next to line #1 while the tuning algorithm was inactive during the HDL.

The discontinuity in the middle of line #1 is due to an existing dangling bond on the litho path prior to conducting the HDL. In fact, while the STM tip is traveling over the sample during HDL, an existing dangling bond causes the controller to move the tip away from the sample. After the dangling bond is passed, it takes a certain time for the tip to get back to its initial value and restart depassivation of H atoms. During this time some H atoms are likely missed. The dangling bond highlighted by green circle in Figure 5.1a causes a discontinuity in the litho pattern in Figure 5.1b highlighted by green circle therein.

To better understand the difference between the two cases, we have recorded control command and error signals during the HDL. Figure 5.2 displays the control error ($Log(i)$ error) and control command (piezo drive voltage Z) during part of the two HDL patterns shown in Figure 5.1. Ideally, the control command should be as close as possible to zero. Part of the deviation from zero is due to measurement noise, and part of it is due to sudden jumps in current when a couple of H atoms sitting on a dimer are depassivated. Our observations suggest that when the PI tuning is operating the current is better kept constant and deviation of control error from zero is smaller. To quantify this observation, we calculated the mean (m) and standard deviation (SD) of the control error signal shown in Figure 5.2 and found

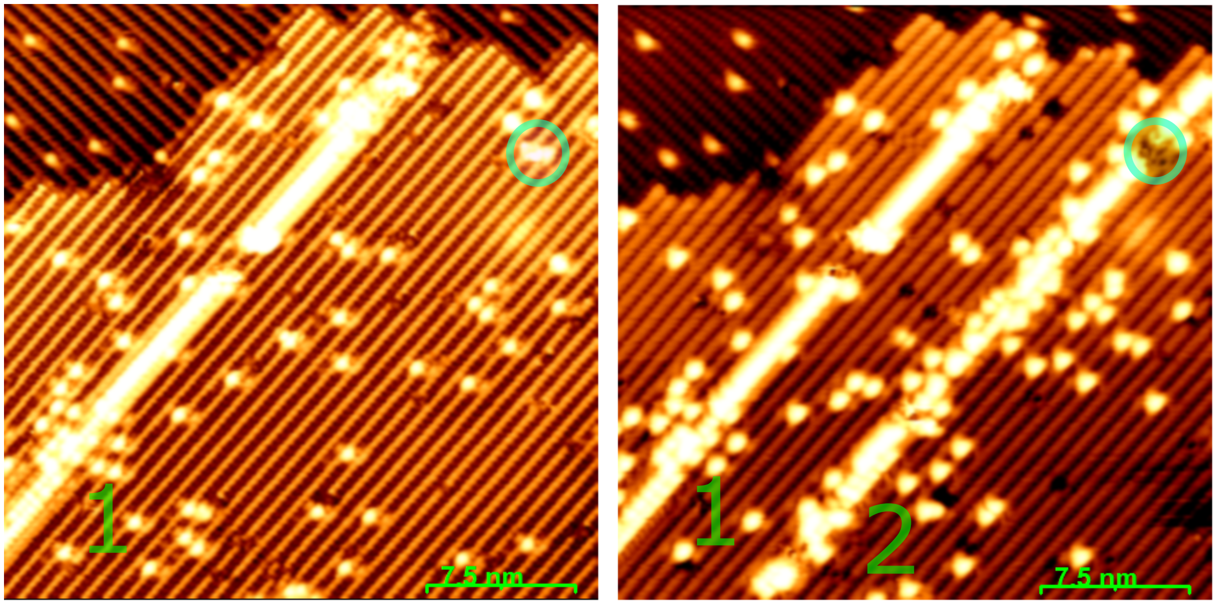

(a) (b)

Figure 5.1. (a) HDL line #1 drawn while self-tuning PI controller was active (b) HDL line #2 drawn while self-tuning algorithm was inactive. Area shown by green circle in (a) contains a dangling bond that causes a discontinuity in HDL line in (b). Green circle in (a) shows a dangling bond which causes a discontinuity in the HDL pattern in line #2.

$m_{On} = 8.42$, $SD_{On} = 0.040$, $m_{Off} = 8.42$, and $SD_{Off} = 0.052$, which shows that the deviation of error signal from zero is less when the tuning is operating. To better understand the idea, we divided the range of variation of error signal in Figure 5.2 into 10 bins and plotted the histogram of the data points falling into these bins as shown in Figure 5.3. Since the number of data points within the zero bin is much larger than the other bins we ignored this bin while plotting the histogram, for better presentation. The obtained histogram shows that the number of data points at bins far from the average is bigger when the tuning is not operating, and this shows larger current errors in the absence of tuning.

Another important potential issue when operating the STM in lithography mode is that due to higher current setpoint there is a higher chance of hitting the upper range of the current pre-amplifier. Once the sensor is saturated, the controller sends a wrong command to the actuator and this can cause damage to the tip. To avoid this issue, the pre-amplifier

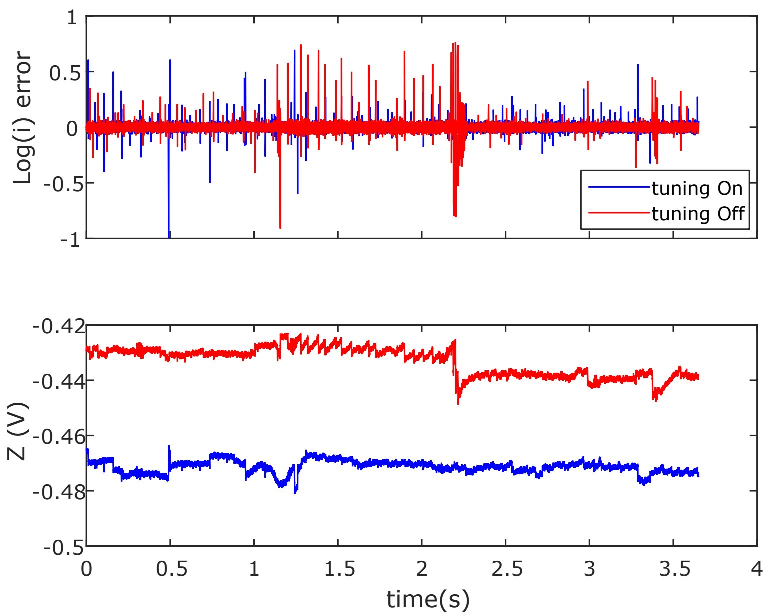

Figure 5.2. Control error signal (top) and controller command (bottom) during part of the HDL associated with Figure 5.1, with and without the PI tuning algorithm.

range should be increased. Nevertheless, due to sharp jumps in current during HDL, a chance of sensor saturation always exists. For example, during the HDL associated with line #2 in Figure 5.1, where the tuning is inactive, we detected a number of sensor saturation instances. Figure 5.4 displays some of these instances that are associated with the data shown in Figure 5.2 for the case of inactive tuning. Current jump due to hydrogen depassivation is so large that it hits the maximum measurable current limit and saturates the sensor. The control error is accumulated during the saturation causing the controller to linearly remove the tip from the sample. This large tip motion causes a sharp downward jump in current right after the sensor gets out of the saturation. Due to the resulting large negative error, the controller moves the tip toward the sample rapidly and this can result in tip crash.

The sharp jumps in the current during the HDL is due to the sudden change in the local barrier height after hydrogen depassivation. In fact, when an H atom is removed, the tunneling junction is changed from tungsten-hydrogen to tungsten-silicon, and the new junction has a different barrier height. This sudden change in LBH tends to increase the

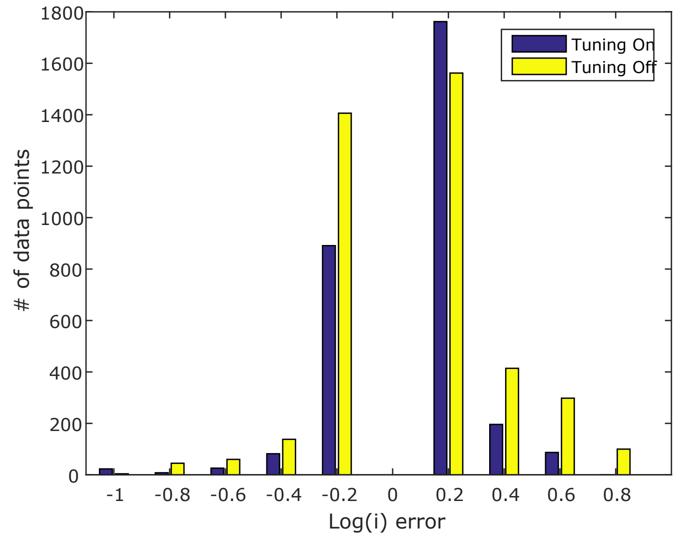

Figure 5.3. Histogram of distribution of $Log(i)$ error shown in Figure 5.2 for the cases with and without PI tuning. Most of the data points for both cases are around zero, thus the zero bin is neglected in the histogram for better presentation. Number of data points falling in bins far from zero is larger for the case of tuning Off. This suggest larger current variations in the absence of tuning.

current because tunneling to silicon is easier than tunneling to hydrogen. However, to keep the current constant, the controller moves the tip away from the sample and this appears as a downward jump in the control command, as well. As the tip continues to travel in XY plane on the sample and reaches the next dimer that contains Hydrogen, the LBH is recovered and the controller brings the tip back to the previous Z position. During HDL, successive depassivation of Hydrogen atoms causes this pattern to repeat. The observed time-spacing between the current spikes is interesting. The horizontal tip speed in Figure 5.4 is $7.5nm/s$, and the time between two successive spikes is approximately $5ms$ which gives a spacing close to $0.384nm$ that is the actual known spacing between the two successive dimmers on the surface. Also, sometimes the spikes appear earlier or later than $5ms$, suggesting that Hydrogen depassivation does not necessarily occur exactly on top of a dimer; it can happen earlier or later. Overall, this observation suggests that spacing between observed current spikes can provide a measure of the quality of ongoing HDL process.

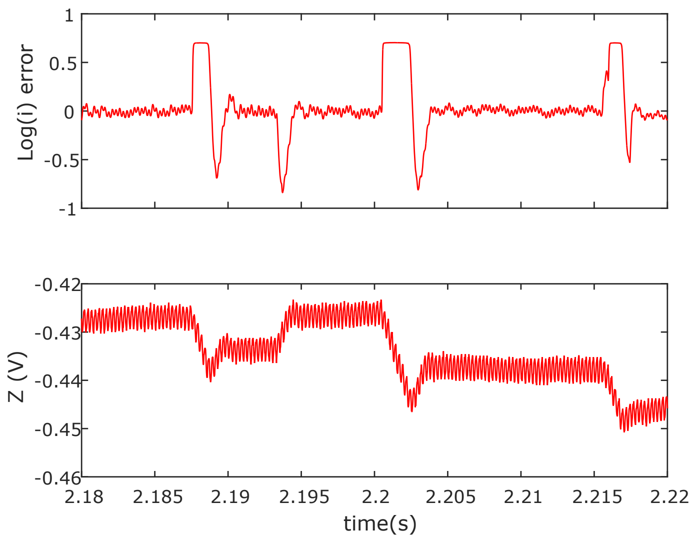

Figure 5.4. Sensor saturation in part of the data associated with the case of inactive tuning shown in Figure 5.2. Current jump due to hydrogen depassivation is so large that it hits the maximum measurable current and saturates the sensor. The control error is accumulated during the saturation causing the controller to linearly remove the tip from the sample.

As shown in Figure 5.2, the current spikes in the case of active tuning are shorter, and we believe this is due to the temporal increase of the PI gain by the tuning algorithm. Shorter current spike lowers the chance of sensor saturation and can be considered as another observed benefit of the proposed PI tuning algorithm.

5.4 Setpoint Modification for Precise Lithography

For some applications, including production of quantum processors [], precise lithography is of critical importance. That is the capability to selectively depassivate an exact number of Hydrogen atoms. To this aim, it must be possible to start or stop the lithography process immediately. In lithography mode bias voltage is positive (around +4 V) and current setpoint is high (around 2 nA), but imaging is performed under lower and negative bias (about -2.5 V) and lower current (about 0.3 nA). Switching bias voltage between positive and negative values can momentarily destabilize feedback control; because when passing through zero

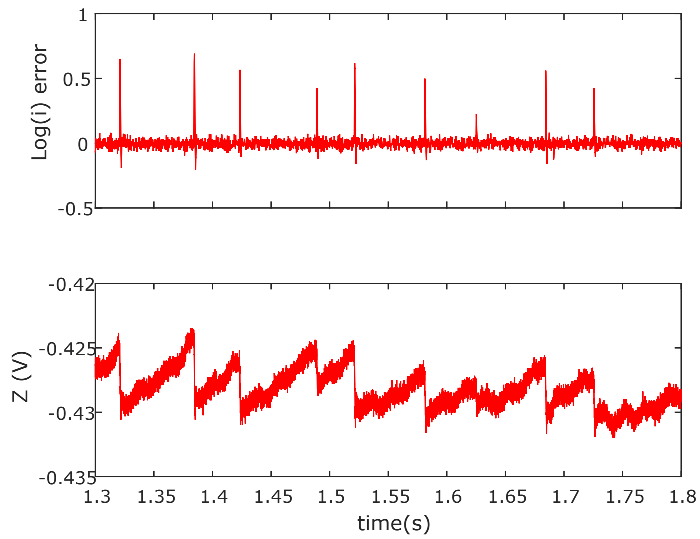

Figure 5.5. Spikes in current associated with depassivation of Hydrogen atoms, associated with the case of inactive PI tuning shown in Figure 5.2.

voltage the current disappears and the controller moves the tip toward the sample that may result in a crash. To avoid this problem, when switching between the imaging and lithography modes the feedback is temporarily disconnected during switching the bias; then feedback is connected again and current setpoint is ramped from low imaging value to high lithography value (or vise versa). Figure 5.6 displays the process of switching from imaging mode to lithography mode.

Since imaging and lithography are performed under different bias polarity, undergoing the process shown in Figure 5.6 is required for switching between the two modes. Overall, switching bias voltage or lowering it is a prevalent method for controlling the occurrence of Hydrogen depassivation. However, from control system point of view, altering bias voltage can be challenging. Firstly, disabling controller during bias switch can increase the risk of tip crash because during that time there is no control over the current. Secondly, due to nonlinear relationship between $log(i)$ and bias, variation of bias should be carefully followed by appropriate variation of current setpoint so that the tip/sample distance is preserved and

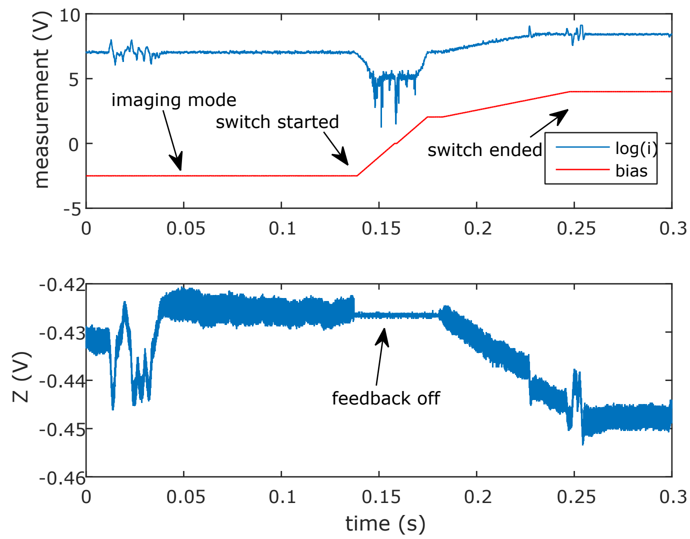

Figure 5.6. Switching from imaging mode to lithography mode. The feedback controller is frozen when bias is switched from negative to positive, then feedback is connected again and both bias and setpoint are ramped to their high lithography values.

tip crash is avoided. Considering these challenges, we propose the idea of current setpoint modification instead of bias variation for interrupting the lithography process.

It is well-known that the removal of hydrogen during the HDL process depends on the value of bias and current. In fact, for feasibility of depassivation, current should be higher than a certain threshold. In other words, if bias remains at the high positive lithography value (+4 V) but current is low, one can expect that no hydrogen depassivation happens. Based on this idea, we propose a methodology for starting and stopping the lithography process. In this proposed method, current setpoint is modified while the STM is in lithography mode so that the HDL process is interrupted for a user-defined time. Figure 5.7 displays an external signal that is multiplied by the current setpoint to modify it during the lithography.

As shown in Figure 5.7, the default value of the setpoint modification factor is 1. However, during HDL and based on a user command, the modification factor is lowered by a step to a low value (e.g. 10%) such that the hydrogen depassivation is stopped due to low current. This interruption is kept for a user-defined time, and then it is ramped up to 1 with a

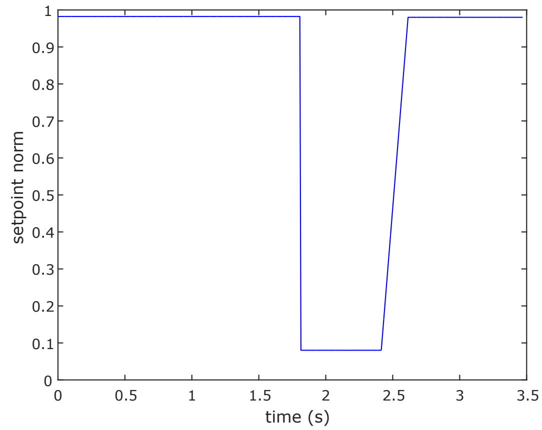

Figure 5.7. External signal that is multiplied by the current setpoint during the HDL. The initial value is 1 but by user command it is stepped down to 0.1, kept at this low value for a certain time, and ramped up to 1 again. HDL interruption is expected during low current time.

user-defined slope to re-start the HDL. We don't use step increase in current setpoint to avoid possible tip crash when approaching the surface. Figure 5.8 displays the HDL pattern that is obtained by current modification as shown in Figure 5.7. Figure 5.9-5.11 also show the time-domain data collected while performing the HDL shown in Figure 5.8. When the current setpoint is stepped down during the HDL, the controller moves the tip away from the sample and due to low current no depassivation occurs as shown in Figure 5.10. The length of the interruption depends on the horizontal speed of the tip that we have fixed at $7.5nm/s$, and the length of the low current period that is user-defined. Figure 5.10 shows that during the low-current period no depassivation happens and the HDL process is resumed after the current passes a certain threshold, where spikes appear again. Figure 5.11 is associated with the 10nm-length portion of the HDL pattern in Figure 5.8, and shows 17 current spikes that matches the 10 nm length of the pattern knowing that the spacing between each two dimers is $0.384nm$. Note that PI tuning was operating while performing the HDL shown in Figure 5.8 and the current spikes in Figure 5.11 are shorter compared to the cases where the PI tuning was Off.

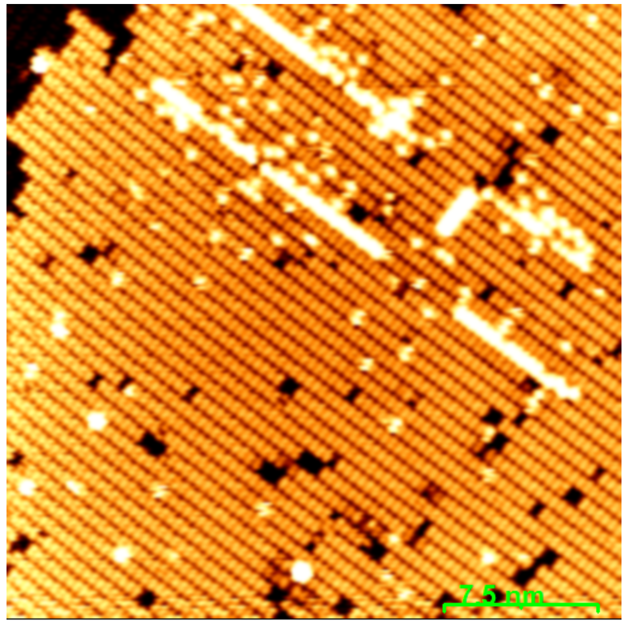

Figure 5.8. The HDL process is interrupted by modifying the current setpoint as shown in Figure 5.7. Sharp start and stop of the HDL due to current manipulation is visible in this image. The length of the interruption is $3.0nm$ that matches the interruption time $0.6s$ and the horizontal travel speed of $7.5nm/s$. PI tuning is operating while performing this HDL.

Another point about the observed current spikes is that while the PI tuning is operating the height of current jumps is usually smaller than that when the PI is not operating. Our results show that when the PI tuning is Off usually taller current spikes are observed. For example Figure 5.12 shows $Log(i)$ vs time for part of an HDL process during which the PI tuning was inactive. The HDL pattern associated with this data is shown in highlighted area in Figure 5.13. Comparing Figure 5.12 with 5.11, it is clear that spikes are larger when the tuning is not operating. Current spikes shown in Figure 5.12 appear in a regular basis: on average, they are $5ms$ apart which is equal to $0.39nm$ spacing between two consequent spikes. The exact spacing between two dimers is known to be $0.384nm$ which is very close to the obtained results and confirms that spikes are associated with hydrogen depassivations. Moreover, spikes appearing in a regular basis suggest that the HDL is being performed along the expected line and no other hydrogen atom from neighboring dimers is depassivated. Insets in Figure 5.12 show part of the data around three spikes. The right inset shows that

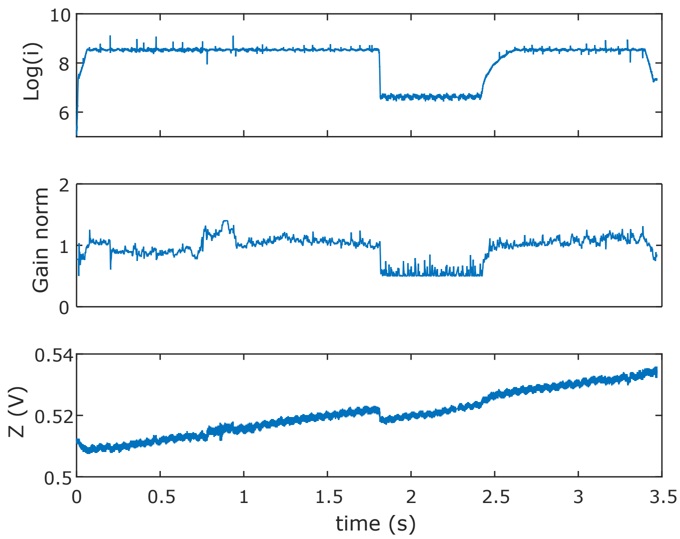

Figure 5.9. Time-domain data collected during the HDL shown in Figure 5.8 showing $Log(i)$, the PI gain modification factor (Gain norm), and the controller command. When current steps down, the HDL is stopped.

pre-amplifier saturation is quite possible due to hydrogen depassivation that is followed by a downward current jump due to controller response to sensor saturation, as discussed before.

Based on the observations presented so far, it is clear that sharp start and sharp stop of the HDL process by manipulating the current setpoint is possible. Our ultimate goal here is to draw HDL patterns containing only 3 dimers ($1.15nm$ length). To this aim we reverse the current manipulation process such that the process is continued only for a user-defined time. Figure 5.14 displays how we change the current setpoint during an HDL process. Based on this manipulation of current setpoint, we expect the HDL process to stop for a while, then continue for a user-defined time and stop again. Note that we use this strategy to keep the STM in lithography mode and draw an HDL pattern with precise user-defined length.

Figure 5.15-5.16 display the time-domain data obtained during an HDL process where current setpoint is manipulated according to Figure 5.14. As shown in these figures, using the proposed scenario we can selectively start and stop the HDL process and draw patterns of user-defined length. In Figure 5.16 10 current jumps are visible which should result in

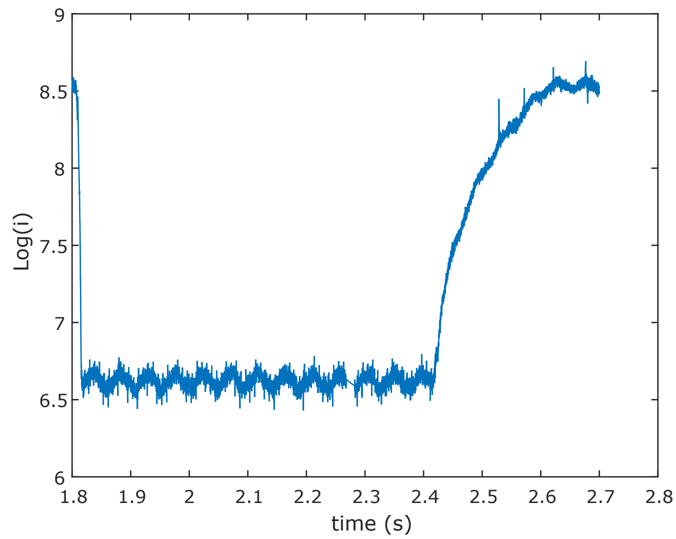

Figure 5.10. Portion of $Log(i)$ vs time data when the current is stepped down. Lack of current spikes confirm that there is no hydrogen depassivation during this time. When current ramps up again, the depassivation starts after a certain current threshold.

an HDL pattern of length $3.8nm$ and actually it is as shown by the highlighted area in the STM image shown in Figure 5.17.

5.5 Conclusions

In this chapter we first showed that the proposed PI tuning method lowers the risk of pre-amplifier saturation by improving the transient response of the closed-loop system and lowering the height current spikes. Sensor saturation is an undesired event that should be avoided in order to prevent the tip-sample crash failure.

We also investigated the STM performance in nano-lithography and proposed a procedure for drawing precise HDL patterns. We showed that it is possible to start/stop the lithography process by adjusting the current setpoint while sample bias is kept constant. This helps to avoid switching the bias from negative imaging value to positive lithography value (that in turn needs temporary disconnecting the feedback loop). We showed that drawing precise HDL patterns is more feasible using the proposed procedure.

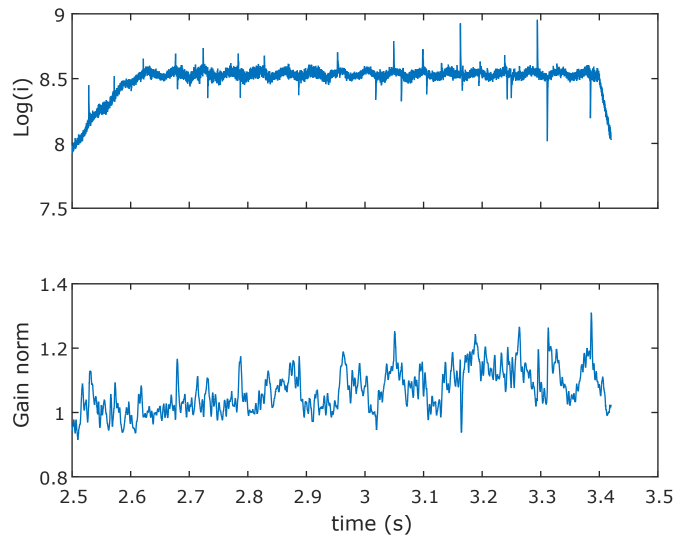

Figure 5.11. Part of the time-domain data shown in Figure 5.9 after the current is ramped up and the HDL is resumed. 17 current spikes are visible that correspond to an HDL pattern of length $6.5nm$ shown in Figure 5.8 given the spacing between dimers that is $0.384nm$. PI tuning is operating and PI gains are modified by Gain norm signal.

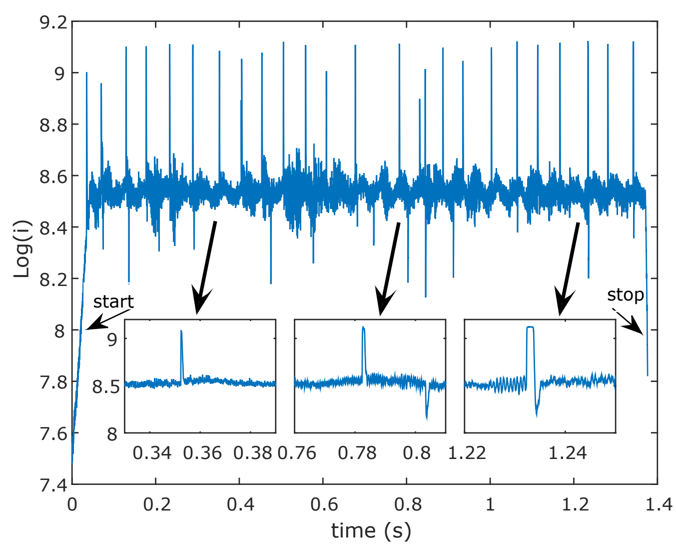

Figure 5.12. Logarithm of current while performing an HDL highlighted in Figure 5.13. PI tuning is not operating and current spikes are larger. Insets display zoomed view of the data to show individual spikes. The right inset shows that the current pre-amplifier is saturated following a spike and the controller causes a downward spike right after saturation. Spikes occur approximately every $5ms$ that gives a $0.39nm$ spacing between dimers. The exact value is know to be $0.384nm$.

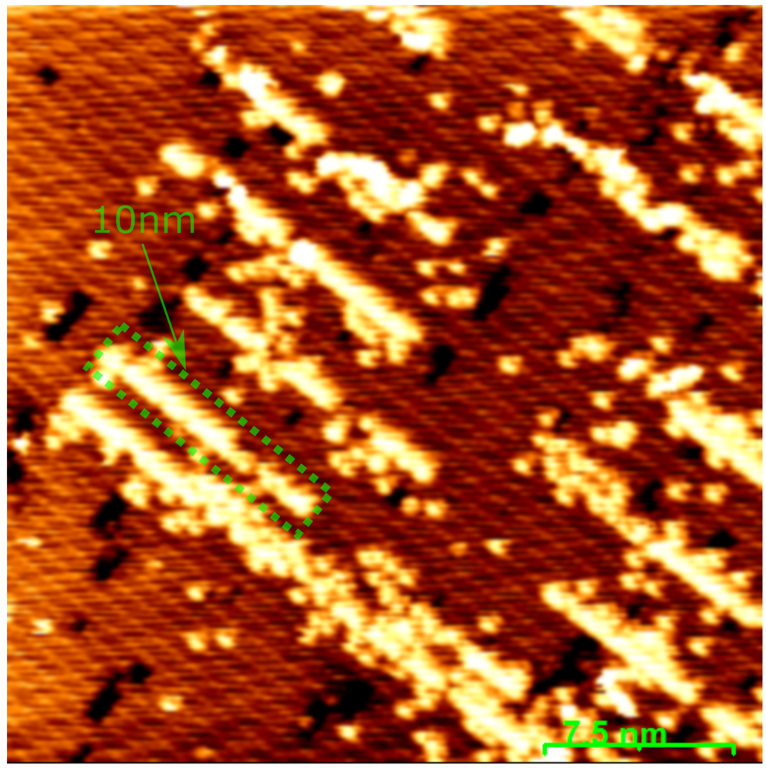

Figure 5.13. STM image showing the HDL pattern associated with the data shown in Figure 5.12.

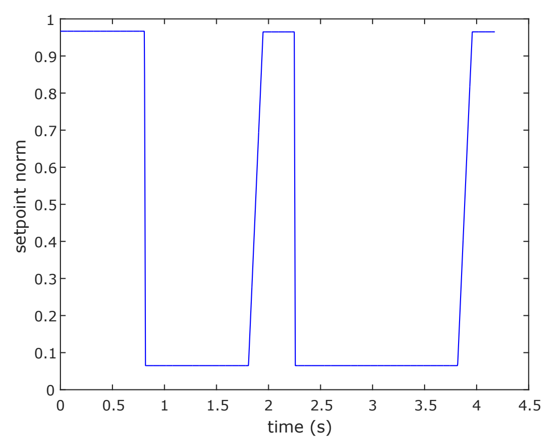

Figure 5.14. External signal that is multiplied by the current setpoint during the HDL. The initial value is 1, then based on a user command it drops to 10%, stays there for a while, ramps up to 1, and drops again to 10 %. HDL is expected to occur only when this signal is at its high level.

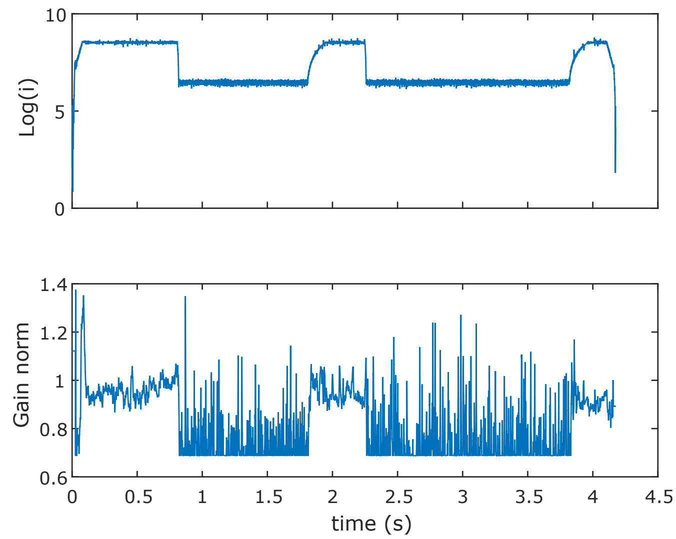

Figure 5.15. Time-domain data showing $Log(i)$ and the PI gain modifying signal (Gain norm) during an HDL process where current setpoint is manipulated based on Figure 5.14.

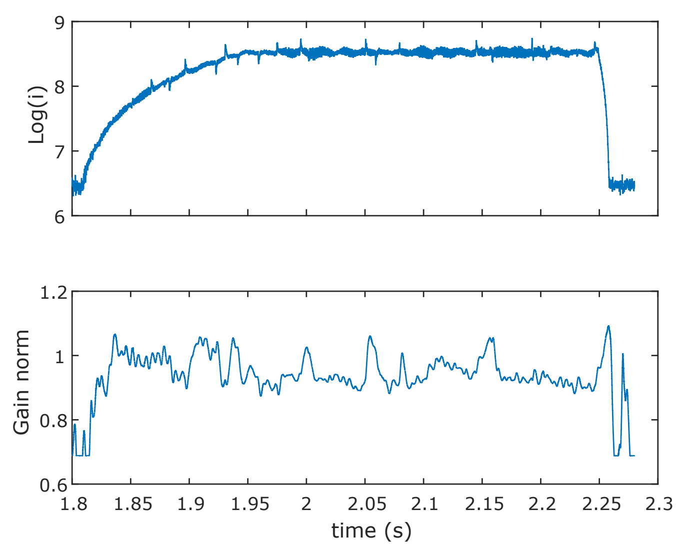

Figure 5.16. Time-domain data showing $Log(i)$ and the PI gain modifying signal (Gain norm) where the HDL starts and stop associated with Figure 5.15.

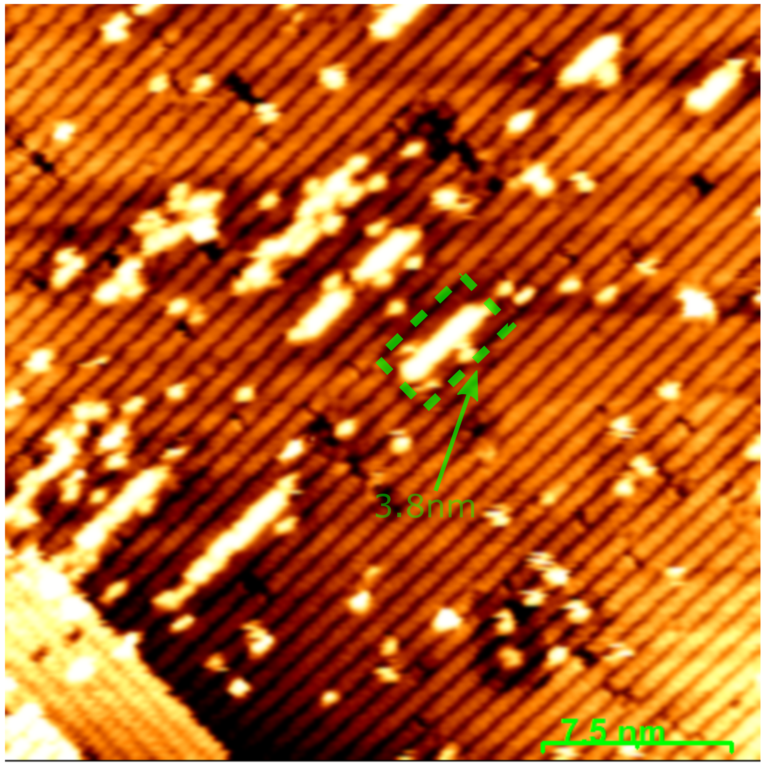

Figure 5.17. STM image showing the HDL pattern associated with the data shown in Figure 5.15.

CHAPTER 6

CONCLUSIONS AND FUTURE WORKS

In this chapter we review our major achievements in this project and discuss the possible future works.

6.1 Conclusions

Our major goal in this project was to understand the mechanism of STM tip crashes and improve control system performance to reduce the risk of those failures. We approached the problem by analyzing the control system of an existing STM. We conducted Frequency-domain closed-loop system identification tests to obtain open-loop models of the STM. Our analysis showed that DC gain of the open-loop plant is proportional to the Local Barrier Height (LBH) which is a quantum mechanical property of the tip and the sample. The LBH is known to be a variable parameter in STM which depends on many local effects. We showed that the LBH variation can dramatically change the loop gain in the presence of a controller with fixed parameters and this can easily result in closed-loop instability. In Chapter 3 we presented details of our analysis and experimental studies that support this claim. To the best of the author's knowledge, this is the first time that the LBH link to STM closed-loop stability is investigated.

Understanding DC gain variations due to LBH changes motivated us to propose an algorithm for on-line LBH estimation and use that to adaptively tune the PI controller gains. The estimated LBH is also used for generating LBH images which map electronic properties of the surface. Our proposed method for LBH estimation is different from the "Gap Modulation Method" that was proposed in early STM works. The difference is that, despite the other method, our procedure gives LBH estimations that are not dependent on feedback parameters, and this is expected because LBH only depends on tip and sample properties. Moreover, we showed that results of our proposed LBH estimation method are less correlated to surface topography. In Chapter 4 we presented the details of our approach for LBH estimation and PI tuning, and reported experimental observations that confirm improved STM stability in the presence of the PI tuning algorithm. Furthermore, we investigated effects of the proposed method on the STM tip life-cycle. Obtained results suggest extended tip durability due to reduced chance of tip.

We also investigated the STM in lithography mode and showed that the proposed tuning method improves the control system performance in this mode as well. Given the harsh conditions that the STM tip experiences during the lithography and due the undergoing chemical reactions, LBH is subject to sudden changes in lithography, and this can easily result in closed-loop instability and tip-sample crash. In Chapter 5 we presented obtained experimental results confirming that in the presence of the tuning algorithm the current jumps due to hydrogen depassivations are smaller. This immediately lowers the chance of pre-amplifier saturation which is observed frequently with fixed PI gains and results in unreliable control performance.

Usually bias is altered to start and stop the lithography process. We suggested using current manipulation for starting and stopping the lithography process instead. Adjusting current to control lithography makes sure that the feedback loop remains operational and there is no need to temporarily switch it off when changing bias polarity during switching between imaging and lithography modes. We showed that drawing extremely precise HDL patterns is possible using current manipulation. We also suggested a single-dimer lithography procedure which ensures an exact number of hydrogen depassivations by counting the number of current jumps. This procedure also keeps the tip away from the harsh lithography conditions as much as possible and is expected to lower the number of tip-changes during lithography. This facilitates drawing precise 3-dimer patterns with increased repeatability, and is a forward step toward atomically-precise manufacturing.

6.2 Future Works

Our achievements in this project clear the path for future research to improve STM performance. From control systems perspective, the following headlines are suggested for future works:

- Identifying the system dynamics on-the-fly: this can be based on time-domain system identification procedure and would help to keep track of the whole changing system dynamics and adjust the control parameters accordingly.
- Replacing fixed-gain PI controller with an advanced model-based controller that is robust to variations in system dynamics
- improving performance of the proposed self-tuning PI controller by increasing the LBH estimation bandwidth

Moreover, in order to improve STM performance in lithography and aiming to draw extremely precise HDL patterns, the following steps are suggested:

- Investigating the parameters (bias and current) required to break H-Si bond, and describing the statistical distribution of these parameters to better understand the HDL phenomenon
- Investigating efficient methods to detect current jump due to hydrogen depassivation. This would help to build more robust single dimer depassivation procedure.
- mixing imaging and lithography in order to improve lateral positioning of the tip. This can be performed by acquiring a small local image prior to landing the tip on a dimer to make sure that the tip will land exactly on top of a single dimer.

The author hopes that achievements of this dissertation will be considered as a small but efficient step toward the future atomically-precise manufacturing.

REFERENCES

Ahmad, I., A. Voda, and G. Besancon (2008). Controller design for a closed-loop scanning tunneling microscope. In *2008 IEEE International Conference on Automation Science and Engineering*, Volume 2, Washington DC- USA, pp. 971–976.

Ahmad, I., A. Voda, and G. Besancon (2009). H-infinity controller design for high-performance scanning tunneling microscope. In *Proceedings of the 48h IEEE Conference on Decision and Control (CDC) held jointly with 2009 28th Chinese Control Conference*, pp. 6058–6063.

Ahmad, I., A. Voda, G. Besançon, and G. Buche (2012). Robust digital control approach for high performance tunneling current measurement system. *Control Engineering Practice 20*(7), 643–653.

Akçay, H. (2010). An insight into instrumental variable frequency-domain subspace identification. *Automatica 46*(2), 375–382.

Anguiano, E., A. I. Oliva, and M. Aguilar (1998). Optimal conditions for imaging in scanning tunneling microscopy: Theory. *Review of Scientific Instruments 69*(11), 3867.

Ballard, J. B., T. W. Sisson, J. H. G. Owen, W. R. Owen, E. Fuchs, J. Alexander, J. N. Randall, and J. R. Von Ehr (2013). Multimode hydrogen depassivation lithography: A method for optimizing atomically precise write times. *Journal of Vacuum Science & Technology B: Microelectronics and Nanometer Structures 31*(6), 06FC01.

Binnig, G., N. Garcia, H. Rohrer, J. M. Soler, and F. Flores (1984). Electron-metal-surface interaction potential with vacuum tunneling: Observation of the image force. *Physical Review B 30*(8), 4816–4818.

Binnig, G. and H. Rohrer (2000). Scanning tunneling microscopy. *IBM Journal of Research and Development 44*(1.2), 279–293.

Blanvillain, S., A. Voda, G. Besançon, and G. Buche (2014). Subnanometer Positioning and Drift Compensation With Tunneling Current. *IEEE Transactions on Control Systems Technology 22*(1), 180–189.

Bonnail, N., D. Tonneau, F. Jandard, G.-a. Capolino, and H. Dallaporta (2004). Variable Structure Control of a Piezoelectric Actuator for a Scanning Tunneling Microscope. *IEEE Transactions on Industrial Electronics 51*(2), 354–363.

Boudreau, A., B. Paillard, and P. Rowntree (2002). High-performance digital control system for scanning tunnelling microscopy. *Measurement Science and Technology 13*, 1599–1607.

Cai, W., F. Pang, J. Wang, H. Liu, X. J. Liang, Q. K. Xue, and D. M. Chen (2007). Ultrahigh vacuum, variable temperature, dual scanning tunneling microscope system operating under high magnetic field. *Review of scientific instruments 78*(6), 065108.

Cao, Y. and X. B. Chen (2014). A Survey of Modeling and Control Issues for Piezo-electric Actuators. *Journal of Dynamic Systems, Measurement, and Control 137*(1), 014001.

Cauberghe, B., P. Guillaume, R. Pintelon, and P. Verboven (2006). Frequency-domain subspace identification using FRF data from arbitrary signals. *Journal of Sound and Vibration 290*(3-5), 555–571.

Claes, M., M. R. Graham, and R. A. De Callafon (2007). Frequency domain subspace identification of a tape servo system. *Microsystem Technologies 13*(8-10), 1439–1447.

Clayton, G. M. and S. Devasia (2005). Image-based compensation of dynamic effects in scanning tunnelling microscopes. *Nanotechnology 16*(6), 809–818.

Clayton, G. M., S. Tien, K. K. Leang, Q. Zou, and S. Devasia (2009). A Review of Feedforward Control Approaches in Nanopositioning for High-Speed SPM. *Journal of Dynamic Systems, Measurement, and Control 131*(6), 061101.

Devasia, S., E. Eleftheriou, and S. O. R. Moheimani (2007). A survey of control issues in nanopositioning. *IEEE Transactions on Control Systems Technology 15*(5 SPEC. ISS.), 802–823.

Döhler, M. and L. Mevel (2012). Modular subspace-based system identification from multi-setup measurements. *IEEE Transactions on Automatic Control 57*(11), 2951–2956.

Fleming, A. J. (2013). A review of nanometer resolution position sensors: Operation and performance. *Sensors and Actuators A: Physical 190*, 106–126.

Forssell, U. and L. Ljung (1999). Closed-loop identification revisited. *Automatica 35*(7), 1215–1241.

Fuechsle, M., J. A. Miwa, S. Mahapatra, H. Ryu, S. Lee, O. Warschkow, L. C. L. Hollenberg, G. Klimeck, and M. Y. Simmons (2012). A single-atom transistor. *Nature nanotechnology 7*(4), 242–246.

Garcia, N., C. Ocal, and F. Flores (1983). Model Theory for Scanning Tunneling Microscopy: Application to Au(110)(1x2). *Physical Review Letters 50*(25), 2002–2005.

Hansma V.B. Elings, O. Marti, C.E. Bracker, P. K. (1988). Scanning tunneling microscopy and atomic force microscopy: Application to biology and technology. *Science 242*, 209–216.

Hla, S. W. and K. H. Rieder (2002). Engineering of single molecules with a scanning tunneling microscope tip. *Superlattices and Microstructures 31*(1), 63–72.

Ioannou, P. A. and J. Sun (1996). *Robust Adaptive Control*.

Jammoussi, H., M. Franchek, K. Grigoriadis, and M. Books (2013). Closed-Loop System Identification Based on Data Correlation. *Journal of Dynamic Systems, Measurement, and Control 136*(1), 014507.

Jia, J., K. Inoue, Y. Hasegawa, W. Yang, and T. Sakurai (1998). Variation of the local work function at steps on metal surfaces studied with STM. *Physical Review B 58*(3), 1193–1196.

Jin, Q., Z. Wang, R. Yang, and J. Wang (2014). An effective direct closed loop identification method for linear multivariable systems with colored noise. *Journal of Process Control 24*(5), 485–492.

Kuk, Y. (1990). Scanning tunneling spectroscopy of metal surfaces. *Journal of Vacuum Science & Technology A: Vacuum, Surfaces, and Films 8*(1), 289.

Lang, N. (1988). Apparent barrier height in scanning tunneling microscopy. *Physical Review B 37*(17), 10395–10398.

Lee, W. C. T., S. R. McKibbin, D. L. Thompson, K. Xue, G. Scappucci, N. Bishop, G. K. Celler, M. S. Carroll, and M. Y. Simmons (2014). Lithography and doping in strained Si towards atomically precise device fabrication. *Nanotechnology 25*(14), 8.

Liu, H., Y. Meng, H. W. Zhao, and D. M. Chen (2007). Active mechanical noise cancellation scanning tunneling microscope. *Review of Scientific Instruments 78*(7), 073705.

Ljung, L. (1999). *System Identification: Theory for the user*. Prentice Hall.

Loth, S., M. Etzkorn, C. P. Lutz, D. M. Eigler, and A. J. Heinrich (2010). Measurement of fast electron spin relaxation times with atomic resolution. *Science 329*(5999), 1628–1630.

Lyding, J. W., T. C. Shen, J. S. Hubacek, J. R. Tucker, and G. C. Abeln (1994). Nanoscale patterning and oxidation of H-passivated Si(100)-2x1 surfaces with an ultrahigh vacuum scanning tunneling microscope. *Applied Physics Letters 64*(15), 2010–2012.

Lyding, J. W., S. Skala, J. S. Hubacek, R. Brockenbrough, and G. Gammie (1988). Variable-temperature scanning tunneling microscope. *Review of Scientific Instruments 59*(9), 1897–1902.

Maeda, Y., M. Okumura, S. Tsubota, M. Kohyama, and M. Haruta (2004). Local barrier height of Au nanoparticles on a TiO2(1 1 0)-(1 x 2) surface. *Applied Surface Science 222*(1-4), 409–414.

Minase, J., T.-F. Lu, B. Cazzolato, and S. Grainger (2010). A review, supported by experimental results, of voltage, charge and capacitor insertion method for driving piezoelectric actuators. *Precision Engineering 34*(4), 692–700.

Moheimani, S. O. R. and A. J. Fleming (2006). Piezoelectric transducers for vibration control and damping. In *Advances in Industrial Control*. Springer.

Noël, J. P. and G. Kerschen (2013). Frequency-domain subspace identification for nonlinear mechanical systems. *Mechanical Systems and Signal Processing 40*(2), 701–717.

Oliva, a. I., M. Aguilar, J. L. Peña, and E. Anguiano (1997). Experimental determination of the parameters of the feedback system of a scanning tunnelling microscope. *Measurement Science and Technology 8*(5), 501–507.

Oliva, A. I., E. Anguiano, N. Denisenko, M. Aguilar, and J. L. Penna (1995). Analysis of scanning tunneling microscopy feedback system. *Review of Scientific Instruments 66*(5), 3196.

Patwardhan, R. S. and R. B. Goapluni (2014). A moving horizon approach to input design for closed loop identification. *Journal of Process Control 24*(3), 188–202.

Pintelon, R. (2002). Frequency-domain subspace system identification using non-parametric noise models. *Automatica 38*(8), 1295–1311.

Pintelon, R. and J. Schoukens (2012). *System Identification, A Frequency Domain Approach*. John Wiley & Sons.

Pouliquen, M., O. Gehan, and E. Pigeon (2014). Bounded-error identification for closed-loop systems. *Automatica 50*(7), 1884–1890.

Rahim, M. A., M. Ramasamy, L. D. Tufa, and A. Faisal (2014). Iterative closed-loop identification of MIMO systems using ARX-based Leaky Least Mean Square Algorithm. *Proceedings - 4th IEEE International Conference on Control System, Computing and Engineering, ICCSCE 2014* (November), 611–616.

Randall, J. N., J. W. Lyding, S. Schmucker, J. R. Von Ehr, J. Ballard, R. Saini, H. Xu, and Y. Ding (2009). Atomic precision lithography on Si. *Journal of Vacuum Science & Technology B: Microelectronics and Nanometer Structures 27*(6), 2764.

Ryba, Ł., A. Voda, and G. Besanc (2014). 3DOF nanopositioning control of an experimental tunneling current-based platform. In *IEEE Conference on Control Applications (CCA) Part of 2014 IEEE Multi-conference on Systems and Control*, pp. 1976–1981.

ScientaOmicron. Variable Temperature SPM: Benchmarking UHV STM and AFM Technology. http://www.scientaomicron.com/en/products/variable-temperature-spm.

Skogestad, S. and I. Postlethwaite (2005). Multivariable Feedback Control: Analysis and Design. WILEY.

Smith, R. S. (2014). Frequency domain subspace identification using nuclear norm minimization and Hankel matrix realizations. *IEEE Transactions on Automatic Control 59*(11), 2886–2896.

Stieg, A. Z., H. I. Rasool, and J. K. Gimzewski (2008). A flexible, highly stable electrochemical scanning probe microscope for nanoscale studies at the solid-liquid interface. *Review of Scientific Instruments 79*(10), 103701.

Tajaddodianfar, F., A. Fowler, E. Fuchs, J. Randall N., and S. O. R. Moheimani (2016). Frequency-domain closed-loop system identification of a scanning tunneling microscope. In *ASPE 2016 Spring Topical Meeting Precision Mechatronic System Design and Control*, Massachusetts Institute of Technology, Cambridge, Massachusetts, USA, pp. 54–57.

Tajaddodianfar, F., S. O. R. Moheimani, E. Fuchs, and J. N. Randall (2017). Stability Analysis of A Scanning Tunneling Microscope Control System. In *American Control Conference (ACC)*, Seattle, WA, USA, pp. 204–209. IEEE.

Tajaddodianfar, F., S. O. R. Moheimani, J. Owen, and J. N. Randall (2017). A Self-tuning Controller for High-Performance Scanning Tunneling Microscopy. In *IEEE Conference on Control Technology and Applications (CCTA)*, Hawaii, USA, pp. 106–110.

Troyanovskiy, A. M. and D. Roditchev (2012). A Compact 3D Nanopositioner of a Scanning Tunneling Microscope Operating at Temperatures of 4.2-300K. *Instruments and Experimental Techniques 55*(6), 711–716.

Voigtlander, B. (2015). *Scanning Probe Microscopy, Atomic Force Microscopy and Scanning Tunneling Microscopy.* Berlin: Springer-Verlag.

Weber, B., S. Mahapatra, H. Ryu, S. Lee, A. Fuhrer, D. L. Thompson, W. C. T. Lee, G. Klimeck, L. C. L. Hollenberg, and M. Y. Simmons (2012). Ohm's Law Survives to the Atomic Scale. *Science 335*, 64–67.

Wiesendanger, R., L. Eng, H. R. Hidber, P. Oelhafen, L. Rosenthaler, U. Staufer, and H. J. Güntherodt (1987). Local tunneling barrier height images obtained with the scanning tunneling microscope. *Surface Science 189-190*(C), 24–28.

Wolkow, R. A. (1992). Direct observation of an increase in buckled dimers on Si(001) at low temperature. *Physical Review Letters 68*(17), 2636–2639.

Yan, W., C. Du, and C. K. Pang (2015). A general multirate approach for direct closed-loop identification to the Nyquist frequency and beyond. *Automatica 53*, 164–170.

Yong, Y. K., S. O. R. Moheimani, B. J. Kenton, and K. K. Leang (2012). Invited Review Article: High-speed flexure-guided nanopositioning: Mechanical design and control issues. *Review of Scientific Instruments 83*(12), 121101.

Zhang, T., P. Cheng, X. Chen, J. F. Jia, X. Ma, K. He, L. Wang, H. Zhang, X. Dai, Z. Fang, X. Xie, and Q. K. Xue (2009). Experimental demonstration of topological surface states protected by Time-Reversal symmetry. *Physical Review Letters 103*(26), 1–4.

BIOGRAPHICAL SKETCH

Farid Tajaddodianfar completed his BS in Mechanical Engineering, honored as the 1st rank student, at K. N. Toosi University of Technology in 2007. He also received his MS and PhD in Mechanical Engineering from Sharif University of Technology and the University of Tehran, in 2010 and 2015, respectively. His research background is in the field of nonlinear dynamics, applied mathematics and statistics, machine learning, control systems and Micro/Nano-Electromechanical-Systems (M/NEMS).

In 2015, he joined the Laboratory of Dynamics and Control of Nanosystems (LDCN) at The University of Texas at Dallas as a Research Assistant and PhD candidate in Mechanical Engineering. He spent a few years researching the design and implementation of an ultra-high precision control system for scanning tunneling microscopy (STM), and completed this dissertation in spring 2018.

CURRICULUM VITAE

Farid Tajaddodianfar

March 25, 2018

Contact Information:

Department of Mechanical Engineering
The University of Texas at Dallas
800 W. Campbell Rd.
Richardson, TX 75080, U.S.A.

Email: farid.tajaddodianfar@utdallas.edu
f.tajad@gmail.com
Google Scholar account
Linkedin account

Educational History:

B.S., Mechanical Engineering, K.N.Toosi University of Technology, 2007
M.S., Mechanical Engineering, Sharif University of Technology, 2010
Ph.D., Mechanical Engineering, University of Tehran, 2015
Ph.D., Mechanical Engineering, The University of Texas at Dallas, 2018

High Performance Control Design for Scanning Tunneling Microscopy
Ph.D. Dissertation
Mechanical Engineering Department, The University of Texas at Dallas
Advisor: Prof. S.O.Reza Moheimani

Nonlinear Dynamics of Initially Curved MEMS Resonators
Ph.D. Dissertation
Mechanical Engineering Department, University of Tehran
Advisor: Prof. Mohammadreza Hairi Yazi

Stability Analysis of Human-Machine Interaction in Haptic Robotic Systems
M.Sc. Dissertation
Mechanical Engineering Department, Sharif University of Technology
Advisor: Prof. Mohammad Taghi Ahmadian

Employment History:

Research Assistant, The University of Texas at Dallas, September 2015 - February 2018
Applied Researcher, Microsoft (Windows and Devices Group), February 2018 – present

Publications:

- **F. Tajaddodianfar**, S.O R. Moheimani, J. Owen, J. N. Randall, *On the effect of local barrier height in scanning tunneling microscopy: Measurement methods and control implications*, Review of Scientific Instruments, vol. 89(1), 2018

- **F. Tajaddodianfar**, A. Fowler, E. Fuchs, J. N. Randall, and S. R. Moheimani, *Frequency-domain closed-loop system identification of a scanning tunneling microscope*, ASPE 2016 Spring Topical Meeting Precision Mechatronic System Design and Control, Massachusetts Institute of Technology, Cambridge, Massachusetts, USA, 2016, pp. 54-57.

- **F. Tajaddodianfar**, S. O. R. Moheimani, E. Fuchs, J. N. Randall, *Stability Analysis of a Scanning Tunneling Microscope Control System*, 2017 American Control Conference, May 24-26, Seattle, WA, USA

- **F. Tajaddodianfar**, S. O. R. Moheimani, J. N. Randall, *A Self-tuning PI controller for Stabilized Scanning Tunneling Microscopy*, 1st IEEE Conference on Control Technology and Applications, August 27-30, 2017, Hawai'i, USA

- **F. Tajaddodianfar**, S. O. R. Moheimani, J. N. Randall, *Scanning Tunneling Microscope Control: A Self-Tuning PI controller based on Online Local Barrier Height Estimation*, under review.

- **F. Tajaddodianfar**, S. O. R. Moheimani, J. Owen,E. Fuchs, J. Ballard, J. N. Randall,*Self-tuning PI Control for STM Tip Protection*, The 62nd International Conference on Electron, Ion, and Photon Beam Technology and Nanofabrication (EIPBN), May 2018, Puerto Rico, USA

- S. O. R. Moheimani, **F. Tajaddodianfar**, J. N. Randall, E. Fuchs, J. Ballard, J. Owen, *Methods, Devices and Systems for Scanning Tunneling Microscopy Control System Design*, USA patent under review, submitted Sep. 19, 2016

Professional Recognitions and Honors:

Louis J. Beecherl Fellowship, Engineering and Computer Science, The University of Texas at Dallas, 2017

Professional Memberships:

Institute of Electrical and Electronics Engineers (IEEE), 2017–present